The sensitivity of the Durham mk6 ground-based atmospheric cherenkov telescope to very high energy gamma-ray sources

Karl Lyons

The Sensitivity of the Durham Mk6 Ground-based Atmospheric Cherenkov Telescope to Very High Energy Gamma-ray Sources

by Karl Lyons, B.Sc.

A thesis submitted to the University of Durham in accordance with the regulations for admittance to the degree of Doctor of Philosophy

Department of Physics
University of Durham
September, 2001

ACKNOWLEDGEMENTS

There are many people to whome I am indebted for their assistance and support throughout the course of this thesis. I would like to express my gratitude to my supervisor, John L Osborne, for many useful conversations and his guidance. My thanks also go out to past and present colleagues at the Observatory and to the many friends I have gained during my time at the University of Durham, for widening my knowledge of both physics and life.

This thesis has been made possible through the provision of the facilities of the Physics Department at the University of Durham, for which I thank Professor M.R, Pennington. I also wish to thank the Particle Physics and Astronomy Research Council for funding of my research studentship.

PREFACE

The work described in this thesis has been associated with the Durham University Atmospheric Cherenkov Telescopes in Narrabri, NSW, Australia. The author has participated in the operation, maintenance and development of the Mk6 telescope in Narrabri. At the University of Durham the author has also been involved in the routine pre-processing and analysis of data. In addition the author has participated in work regarding the effect of the geomagnetic field on ground based gamma ray observations, though principally work has been focused on the sensitivity of the Durham Mk6 telescope. No part of the material presented in this thesis has been submitted previously for admittance to a degree in this or any other University, As a member of the Durham Gamma-Ray Research Group he has been co-author of 10 papers in referreed journals, some of which cover aspects of the present work performed jointly, such as the review of the observational properties of specific AGNs in the final chapter. All of the material presented in this thesis is the author's own work except where due reference is given. The copyright of this thesis rests with the author.

The Sensitivity of the Durham Mk6 Ground-based Atmospheric Cherenkov Telescope to Very High Energy Gamma Ray Sources

by Karl Lyons, B.Sc. Ph. D. Thesis, University of Durham, 2001

ABSTRACT

The subject of this thesis is a determination of the sensitivity of the Durham Mk6 ground based Imaging Atmospheric Cherenkov Telescope (IACT), an instrument which uses the imaging atmospheric Cherenkov technique to detect Very High Energy (VHE) gamma-rays. The first three chapters are introductory: Chapter 1 describes the basics of Very High Energy (VHE) gamma ray astronomy. Chapter 2 describes the properties of Extensive Air Showers (EAS). Chapter 3 describes the detection of these EAS on the ground by IACTs, Chapter 4 details the Durham Mk6 IACT and includes a description of the Cherenkov imaging technique for background discrimination. Chapter 5 describes the MOCCA and SOLMK simulation codes. Chapter 6 contains a description of the details of the simulations produced for this thesis. This chapter continues to its logical conclusion and presents a revised VHE gamma-ray flux of $2.5 \pm 0.7_{stat}$ [+0.5 or -1.6]$_{syst}$ x 10^{-7} photons m^{-2} s^{-1} for a sub set of a previously published data set which gave a 6.8σ detection of the close X-ray selected BL Lac PKS 2155-304. Chapter 7 discusses the importance of PKS 2155-304 and presents 3σ flux limits for another seven Southern hemisphere AGN observed between 1996 and 1999 using the Durham Mk6 IACT. Finally there is a short discussion on the future of VHE gamma-ray astronomy.

CONTENTS

CHAPTER ONE - VHE Gamma-Ray Astronomy	1
1.1 Introduction	1
1.1.1 Extra-terrestrial ionising radiation	1
1.1.2 Extra-terrestrial neutral radiation	2
1.1.3 VHE gamma-rays	4
1.2 Particle acceleration models	4
1.2.1 Fermi acceleration (2nd order)	5
1.2.2 Fermi acceleration (1st Order)	6
1.3 VHE photon production	10
1.3.1 Synchrotron radiation	10
1.3.2 Curvature radiation	13
1.3.3 Relativistic Bremsstrahlung	14
1.3.4 Inverse Compton effect	15
1.3.5 Pion decay	16
1.4 VHE photon attenuation	17
1.5 Fundamental physics with TeV observations	18
1.5.1 Intergalactic Infrared radiation field	20
1.5.2 Quantum gravity	21
1.5.3 Dark matter	22

CHAPTER TWO - Cherenkov Radiation and Extensive Air Showers 24

2.1 Introduction 24

2.2 Extensive air showers 27

2.2.1 Photon initiated EAS 28

2.2.2 Nucleon Initiated EAS 30

2.2.3 Lateral development of EAS 32

2.3 Cherenkov radiation 34

2.3.1 Cherenkov radiation (background) 34

2.3.2 Cherenkov radiation in the atmosphere 37

2.3.3 Cherenkov radiation from VHE gamma-ray EAS 41

2.3.4 Cherenkov radiation from nucleonic EAS 43

2.3.5 Cherenkov photon yields from EAS 44

2.3.6 Images of Cherenkov radiation from EAS 45

CHAPTER THREE - Ground-based Gamma-Ray Astronomy 48

3.1 Introduction 48

3.2 The detection of Cherenkov radiation from EAS 50

3.2.1 Detection of Cherenkov radiation above the NSB 51

3.2.2 Basic optimisation for detecting radiation from EAS 52

3.3 Specifications for an imaging atmospheric Cherenkov telescope 53

3.3.1 Effective sensitive area 53

3.3.2 Field of view 55

3.3.3 Triggering 56

3.3.4 Telescope energy threshold 57

3.4 The principles of data processing 58

3.4.1 Source tracking and telescope rigidity 58

3.4.2 Photomultiplier calibration 59

3.4.3 Preliminary pre-processing 60

3.5 Summary of VHE observations 61

3.5.1 Recent observations 62

3.6 Summary of IACT telescopes 64

CHAPTER FOUR - The Durham Telescopes 67

4.1 Introduction 67

4.1.1 The Bohena observatory 68

4.2 The Mark 6 telescope 70

4.2.1 Mirrors 71

4.2.2 Detector packages 73

4.2.3 Triggering 74

4.2.4 Electronics 75

4.2.5 Data collection and integrity 76

4.2.6 Data reduction 77

4.3 Cherenkov image analysis 78

4.3.1 Image element selection 79

4.3.2 The moments technique 80

4.3.3 Image parameterisation 82

4.3.4 Physical interpretation of image parameters 85

4.3.5 Physical differences reflected in the Hillas parameters 89

4.3.5 Gamma/nucleon EAS image separation 88

4.3.6 Other strategies for analysis 90

4.4 Detections and flux limits for extragalactic VHE sources 91

CHAPTER FIVE - EAS & Telescope Simulations 93

5.1 Introduction 93

5.1.1 Historical development of simulations 95

5.1.2 Further Monte Carlo studies 97

5.1.3 Monte Carlo simulations and Cherenkov imaging 98

5.1.4 Monte Carlo simulation programs 100

5.2 MOCCA 101

5.2.1 The treatment of particles within MOCCA 103

5.2.2 Heavy nucleus fragmentation 103

5.2.3 The MOCCA energy splitting algorithm 104

5.2.4 Transverse particle momenta within MOCCA 106

5.2.5 Particle type and charge assignment for Glueballs 109

5.2.6 Electrons and gamma-ray photons 109

5.2.7 Cherenkov photon emission 110

5.2.8 MOCCA output and IACT simulations 111

5.3 The SOLMK IACT Monte Carlo simulation program 113

5.3.1 Point spread function 114

5.3.2 Single electron pulse profile 115

5.3.3 dc/pe ratio 116

5.3.4 Simulated triggering 117

5.3.5 Background noise level 117

CHAPTER SIX - Simulation method and results 119

6.1 Introduction 119

6.2 The simulation of cosmic ray induced EAS images 121

6.2.1 The observed cosmic ray spectrum 121

6.2.2 Atmospheric profile 122

6.2.3 Model dependent parameters in SOLMK 124

6.3 Matching the cosmic ray event rate and image distributions 126

6.3.1 Variations in background cosmic ray distributions 128

6.3.2 Event rate 130

6.3.3 Background image parameter distributions 132

6.3.4 The disparity in the length and iratio distributions 136

6.4 Simulated gamma-ray image parameter distributions 138

6.5 Determining the flux of PKS 2155-304 140

6.5.1 The observed data 142

6.5.2 Method for calculation of flux values 143

6.5.3 Spectral index 146

6.5.4 The flux for PKS 2155-304 147

6.6 Statistical and systematic errors 150

6.6.1 Statistical error 150

6.6.2 Systematic error (atmospheric stability and count rate) 151

6.6.3 Systematic error (SOLMK input parameters) 152

6.6.4 Insights from CORSICA and ALTAI 153

6.6.5 Combined systematic error 155

6.7 Conclusion 156

CHAPTER SEVEN - Discussion 158

7.1 Introduction 158

7.2 Upper limits for other southern AGNs 161

7.2.1 Cen A 162

7.2.2 PKS 1514-24 162

7.2.3 1ES 2316-423 163

7.2.4 1ES 1101-232 163

7.2.5 RX J1058-275 163

7.2.6 PKS 0548-322 164

7.2.7 PKS 2005-489 164

7.3 Further work 165

7.4 The future of ground-based gamma-ray astronomy 166

7.4.1 The HESS project 167

Refrences 169

CHAPTER ONE - VHE GAMMA-RAY ASTRONOMY

1.1 Introduction

During the 1970s and 1980s VHE Gamma-ray astronomy developed out of cosmic-ray physics. Originally envisaged as an extension to cosmic-ray physics, by the end of the 20th century VHE gamma-ray astronomy had grown into a mature discipline, providing valuable observations of the physics prevalent in many high energy astrophysical environments, and contributing to the search for the origins of cosmic-rays.

1.1.1 Extra-terrestrial ionising radiation

Cosmic-rays represent a flux of mostly charged high energy particles. The first clues to the existence of cosmic radiation came near the beginning of the 20th century from observations of the discharge of apparently well electrically insulated gold leaf electroscopes. Rutherford and Cook (1903) observed that the rate of discharge from a gold leaf electroscope decreased when the electroscope was isolated from its surroundings by metal shielding, and as the distance between the electroscope and the Earth was increased. The observations of Rutherford and Cook were understood to indicate the presence of an ionising flux of radiation at the Earth's surface.

To test whether this ionising radiation was wholly terrestrial in origin, Goeckel (1910) and Hess (1912) conducted balloon based field experiments which showed that the

flux of ionising radiation decreased only up to an altitude of ~1.5 km. Above this altitude the flux steadily increased up to the altitudes of the highest contemporary balloon experiments conducted by Kolhorster (1913) at about 9km. The conclusion was that some of the ionizing radiation must indeed be extra-terrestrial in origin; later the term "cosmic radiation" was coined by Millikan in 1925. As scientific knowledge accumulated, the nature of cosmic-rays became clearer: they appeared to consist mainly of a wide variety of highly energetic charged particles, the energy density of which is approximately that of starlight photons within the galaxy.

Even today the details of their origin remain unclear. The primary reason for this is that, over interstellar distances, charged particles are scattered by the complex structure of our galaxy's magnetic field, so much so that by the time cosmic-rays reach Earth, all directional information regarding their origin has been lost.

1.1.2 Extra-terrestrial neutral radiation

A small neutral component of cosmic radiation, consisting of neutrinos, neutrons and very high energy (VHE) gamma-rays, will in theory retain its directional information over interstellar distances, though there are significant technical and physical problems with observing neutrinos and neutrons. Neutrinos have an extremely small cross-section for interaction with matter which makes them difficult to detect except in the rare circumstance of a nearby supernova explosion, when very large fluxes of neutrinos are produced.

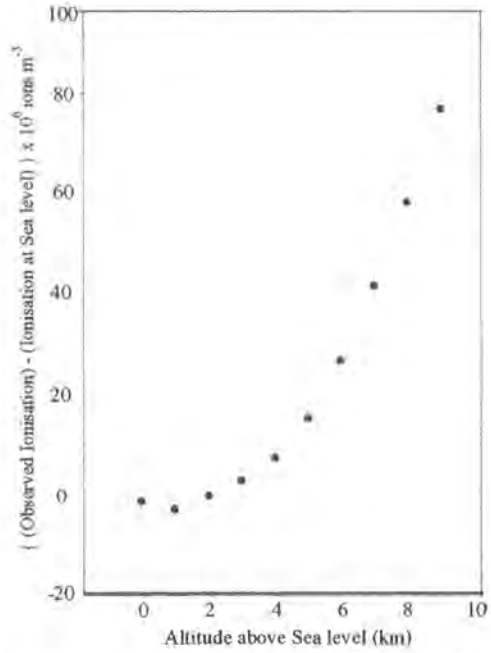

Figure 1.1: The variation of ionisation with altitude from the observations of Kolhorster (data obtained from Hillas (1972)).

Neutrons, on the other hand, have too short a lifetime to provide significant flux over large distances; a neutron generated at the galactic centre, ~ 7 kpc distant, would require an energy of ~ 1 EeV were it to survive to the Earth without decaying. However, VHE gamma-rays can travel over intergalactic distances without interacting and are much easier to detect than either neutrinos or neutrons. Additionally, they are destroyed rather than scattered by interactions and thus any observed VHE gamma-ray must have travelled directly from its source. Though VHE gamma-rays constitute only a fraction (~ 1/10,000) of the total cosmic-ray flux , the study of these gamma-rays can provide valuable information concerning the nature of cosmic-ray sources.

1.1.3 VHE gamma-rays

Gamma-rays are defined as electromagnetic radiation with photon energies greater than 0.511 keV, the rest-mass energy of the electron. This is the lowest energy photon that can be produced via particle annihilation. There are four principal mechanisms for the production of gamma-rays in astrophysical processes: nuclear transitions between energy levels; particle annihilation; elementary particle decay, and the acceleration of charged particles combined with subsequent interactions with magnetic or nuclear fields.

The principal concern of this thesis is with gamma-rays having energies greater than those which are easily detectable by satellite experiments. Thus we may neglect the first of these processes, (i.e. nuclear transitions between energy levels), as this process is not capable of producing the energies suitable for inclusion.

1.2 Particle acceleration models

It is thought, for reasons that will be clarified in the following sections of this chapter, that VHE photons are produced through the acceleration of charged particles and their subsequent interactions. It is clear that charged particles are accelerated to high energies, as the existence of cosmic-rays testifies, and there are a number of mechanisms by which this could happen. The most significant mechanisms will be discussed within this section.

1.2.1 Fermi acceleration (2nd order)

Second order Fermi acceleration is a statistical model for gaining a net increase in the energies of a population of relativistic charged particles. Proposed by Fermi in 1949, this method considers the effect of moving magnetic mirrors on the local particle population, see figure 1.2. Magnetic mirrors are caused by irregularities in the galactic magnetic field which reflect charged particles with which they interact.

Fermi's theorem shows that it is more likely that a particle will gain energy than lose energy, over a large number of collisions. The average fractional gain in energy is dependent on the quantity $(V/c)^2$, where V represents the magnetic mirrors bulk velocitity and c represents the speed of light. In figure 1.2, v represents the interacting particles velocity. In the relativistic limit $\upsilon = c$, the average fractional gain in energy becomes,

$$\left\langle \frac{\Delta E}{E} \right\rangle = \frac{8}{3}\left(\frac{V}{c}\right)^2 .$$

where E is energy, ΔE is the change in energy.

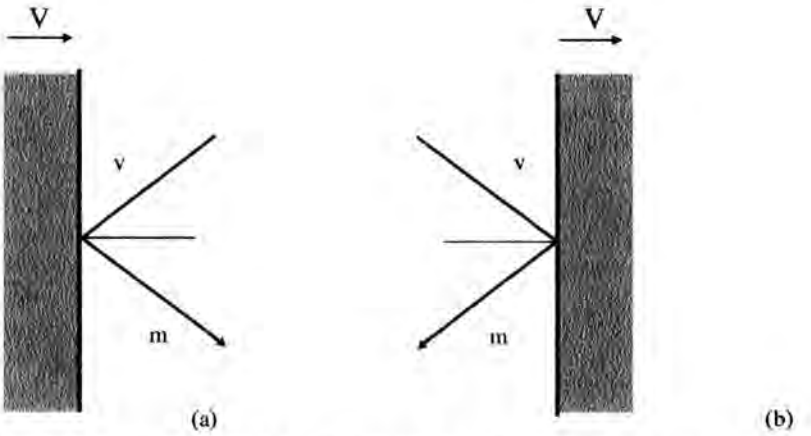

Figure 1.2: Second order Fermi mechanism: a) a head on collision; b) a following collision.

It can be seen from the equation above that the increase in particle energy is exponential, as the fractional increase per collision is the same. If one assumes that the particles remain in the accelerating region for some characteristic time, and that the particle population remains constant, the result particle energies will be in the form of a power law distribution. However, second order Fermi acceleration cannot account for the observed energy spectrum of cosmic-rays at the Earth. As the irregularities in the magnetic field of our galaxy move relatively slowly $V \sim 10^{-4}c$, collisions between these and cosmic-rays are therefore not sufficiently frequent to accelerate particles at a significant rate.

In the version of the Fermi mechanism described above, the average energy gain per collision is proportional to $(V/c)^2$. This result is due to the decelerating effect of the following collisions. Fermi realised that if there were no following collisions to hinder this process, a more favourable first order energy gain would be achievable.

1.2.2 Fermi acceleration (1st Order)

The first order Fermi acceleration is a more effective mechanism for the acceleration of particles to high energy. A mechanism in which only head-on collisions occur, first order Fermi acceleration is able to accelerate particles across regions containing strong shockfronts such as those produced by supernova explosions or the relativistic jets of active galactic nuclei.

When matter expands into a medium at a speed faster than the speed of sound, the expanding matter can have no influence on the material of the medium until it actually collides with it. This produces a shockfront over which the physical characteristics of the medium are discontinuous.

For a shock moving at a supersonic speed of U, and upstream gas of density ρ_1, gas moves into the shock at a velocity $\upsilon_1 = U$ in the reference frame of the shock. The gas then leaves the shock downstream at υ_2, ρ_2. Fluid dynamical equations of continuity require that mass be conserved across the shock such that, in the case of a strong shock,

$$\rho_1 \upsilon_1 = \rho_2 \upsilon_2 \quad [and] \quad \frac{\rho_2}{\rho_1} = \frac{\gamma + 1}{\gamma - 1}$$

where $\gamma = 5/3$ is the specific heat of a fully ionised gas. Hence $\rho_2/\rho_1 = 4$ and $\upsilon_2 = \frac{1}{4}U$. Particles travelling through the shock from upstream will be travelling at a velocity of ¾U relative to the downstream gas. The upstream particles will then be scattered by the irregularity in the downstream gas. In this process the particle has gone from rest in the upstream gas to rest in the downstream gas, a change of ¾U in velocity. Symmetry follows because exactly the same can be said of particles at rest relative to the downstream gas. These particles will also be travelling at ¾U but this time relative to the upstream gas. So, particles are able to gain a small amount of energy ΔE every time particles cross the shock, from either side. Taking a more quantitative look at this process, it is possible with simple arguments to evaluate the average increase in energy for a particle crossing the shock from either side, see figure 1.3.

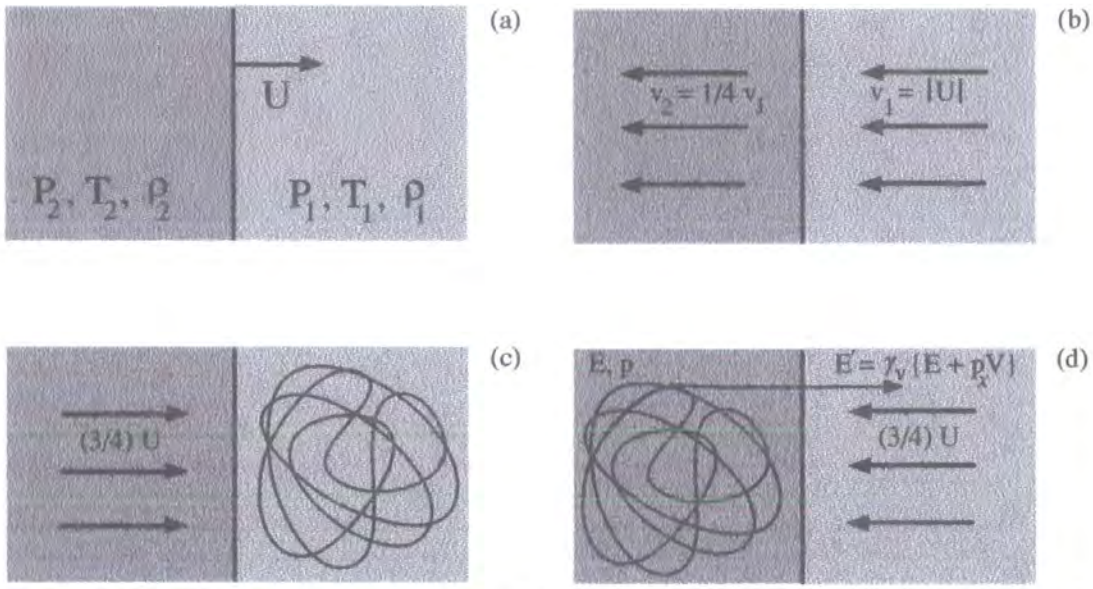

Figure 1.3: The first order Fermi mechanism and dynamics of high energy particles in the vicinity of a strong shock. a) A strong shock propagating at velocity U through a stationary interstellar gas with pressure P_1, temperature T_1 and density ρ_1. b) In the reference frame of the shock, gas upstream moves into the shock at velocity U and exits at a velocity of U/4, since the mass flow rate through the shock must be conserved. c) In the frame of the upstream gas, material moves up behind the shock at 3/4U. When particles pass through this shock their velocity distributions are randomized and become isotropic. d) A particle of energy, E, and momentum, p, passing the shock from either side, experiences a net gain in energy, $\Delta E \sim p_x V$ each time it crosses the shock. (Longair (1997) Vol2)

Upon crossing the shock and being scattered isotropically, particles undergo a change in velocity of $V = \frac{3}{4}U$, so, performing a Lorentz transformation, the particle's energy after crossing the shock is:

$$E' = \gamma_v \left(E + p_x V\right)$$

Assuming the shock is non-relativistic, $V \ll c$, such that $\gamma_V = 1$, but that the particles are relativistic, so that $E = p_x c$, where p_x is the particles' momentum, then $p_x = (E/c)\cos\theta$. Considering that the particle may not cross the shock head on, but at some angle θ from the normal, the average change in energy becomes,

$$\Delta E = p_x V \cos\theta \; ; \; \frac{\Delta E}{E} = \frac{V}{c}\cos\theta$$

i.e. the average fractional energy increase for a particle crossing the shock in the range 0 to $\pi/2$ is proportional to the first order of V/c,

$$\left\langle \frac{\Delta E}{E} \right\rangle = \frac{V}{c} \int_0^{2\pi} 2\cos^2\theta \sin\theta \, d\theta = \frac{2}{3}\frac{V}{c}$$

Given that the typical velocity of material ejected in supernova explosions can be up to about 10^4 km s^{-1} the fractional energy gain is relatively small, with each particle adding only a few percent to their total energy per crossing.

The maximum particle energy obtainable by this method is limited by the lifetime of supernova-induced shocks, typically only ~10^5 years. Some of the accelerated particles escape the acceleration region of the shock leading to a power law spectrum with a well defined differential energy distribution of,

$$N(E)dE = AE^{-2} \, dE$$

(Bell (1978)).

1.3 VHE photon production

The region of the electromagnetic spectrum of interest to VHE gamma-ray astronomy comprises photons in the energy range from ~100 GeV to >10 TeV (1TeV = 10^{12} eV). Photons are produced within this energy range by relativistic particle interactions with magnetic fields, low energy photons and nuclear fields. As the rate of energy loss for a particle due to these processes is inversely proportional to the mass of the particle, attention tends to focus on electrons and positrons, as these predominate as efficient radiators.

1.3.1 Synchrotron radiation

Synchrotron radiation produced by relativistic electrons gyrating in a magnetic field is the dominant emission process in high energy astrophysics. Light particles are very efficient at emitting synchrotron radiation, as the rate of photon production is an inverse function of the particle's mass, $Syn_{eff} \propto m^{-4}$. Electrons moving within a magnetic field are forced to accelerate perpendicular to the instantaneous direction of both its velocity and the magnetic field vectors (i.e. in the direction of the cross-product of its velocity and the magnetic field vectors). This resultant acceleration constantly changes the electron's velocity vector such that the electron follows a helical path along the magnetic field lines.

Radiation is emitted along the electron's instantaneous velocity vector, at a pitch angle α to the magnetic field lines, at a much higher frequency than the gyrofrequency of the electron, see figure 1.4. High energy photon emission is a result

of the relativistic beaming and doppler shifting of the normal dipole emission of an accelerating charged particle, see figure 1.5.

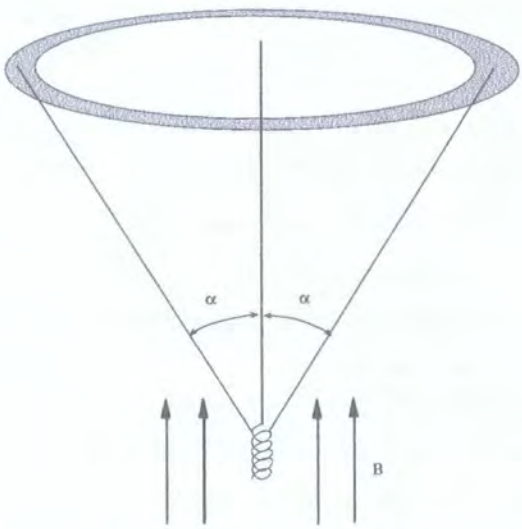

Figure 1.4: Radiation is beamed along a cone; the opening angle is dependent on the pitch angle of the electron.

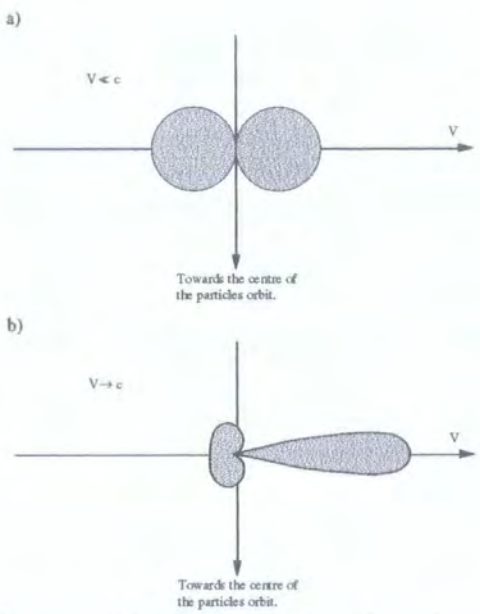

Figure 1.5: The polar diagram of the dipole radiation of an electron in its instantaneous frame of reference. a) when V « c ; b) when V is of the order of c.

The approximate frequency, ν, at which radiation is emitted may be derived from relatively simplistic arguments concerning a relativistic electron moving towards the observer over a small angle of one gyration, significant amounts of radiation are only observed when the strongly elongated dipole radiation is directed towards the observer, with the amount of beaming being inversely proportional to the Lorentz factor of the electron. The fraction ϕ of the electrons' curved trajectory over which emission is observed, can be approximated to $\phi \sim 1/\gamma$, resulting in a very short pulse of radiation and partly explaining why the spectrum of radiation received by the observer is of a much higher frequency than the gyrofrequency of the electron in its orbit.

The maximum Fourier component of the observed pulse of radiation can be shown to be,

$$\nu \approx \gamma^2 \nu_g \sin\alpha$$

where ν_g is the non-relativistic gyrofrequency, α the pitch angle and γ the Lorentz factor. A more detailed analysis of the synchrotron spectrum of radiation emitted by a single gyrating electron has been given by Rybicki & Lightman (1979). Their highly detailed analysis results in the expression,

$$\nu \approx \frac{3}{2} \gamma^2 \nu_g \sin\alpha$$

The energy of the radiation, E_γ (MeV) emitted by electrons with energy, E_e (EeV; 10^{18} eV), in a magnetic field of B (μG), is given by,

$$E_\gamma \approx 20BE_e^2$$

So, the energy of the photons emitted by high energy electrons will be only a small fraction of the total energy of the electron, it is rare that synchrotron photons will be produced at VHE energies. However the emission of X-ray synchrotron radiation from an astrophysical source indicates that a population of electrons exists which have enough energy to act as seed electrons which may produce VHE photons via the inverse Compton effect (see section 1.3.4).

1.3.2 Curvature radiation

Curvature radiation is associated with the acceleration of charged particles, predominantly electrons, as they move along a curved trajectory in a strong (~10^8 Tesla) magnetic field. The electrons are constrained to move along the magnetic field lines; where these lines are strongly curved, the resultant acceleration on the electrons causes them to radiate. The physical mechanism for radiation is very similar to synchrotron radiation except that it is the general curvature of the magnetic field lines and not gyration around the field lines which is the basis of this radiation, see figure 1.6.

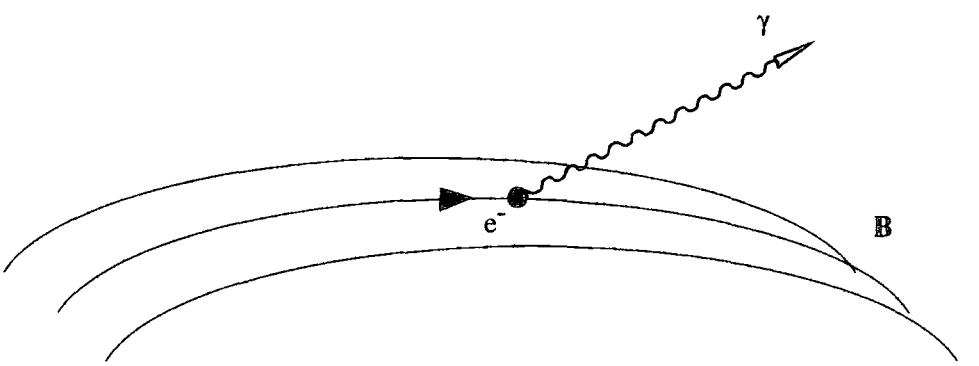

Figure 1.6: Curvature radiation in a strong magnetic field.

1.3.3 Relativistic Bremsstrahlung

Bremsstrahlung or 'braking radiation' is emitted by charged particles passing through an electrostatic field, see figure 1.7, chiefly the radiation from an electron passing through the electrostatic field of an ion or atomic nuclei. With the energy of the radiation dependent on the energy loss rate of the electron, and limited by the total energy of the electron, relativistic Bremsstrahlung may generate photons with frequencies up to $\nu = E_e/h$. On average photon frequencies are ~ $E_e/3h$, where E_e is the electron energy.

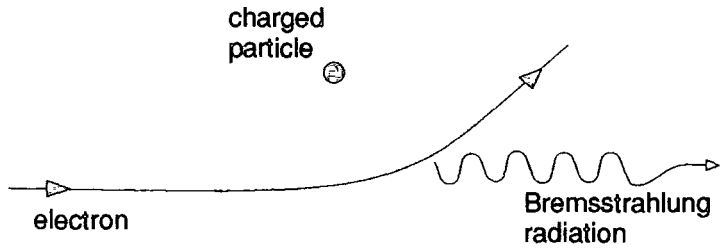

Figure 1.7: Bremsstrahlung: the deviation of an electron by the coulomb field of a charged particle.

An important feature of relativistic Bremsstrahlung in astrophysical environments is the power law electron energy distribution which results, this in turn produces an intensity spectrum for emitted photons of the same power law form. Meaning, that if the electron distribution is described by $N_e(E) = AE^{-x}$ then the photons produced will be of the form $N_\gamma(E) = AE^{-x}$, providing the intensity is measured in terms of the flux density of the photons $m^{-2}s^{-1}MeV^{-1}sr^{-1}$.

1.3.4 Inverse Compton effect

The inverse Compton effect derives directly from Compton scattering in which electrons gain energy by scattering with photons. However, in the inverse case it is the photons which gain energy through scattering with ultra relativistic electrons, see figure 1.8.

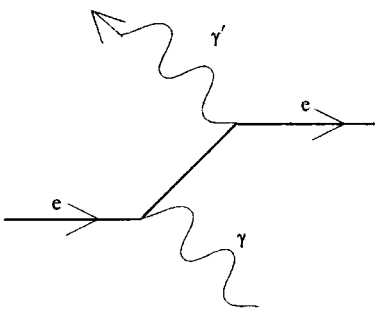

Figure 1.8: Feynman vertices diagram for the inverse Compton effect.

The general result found by (Blumenthal & Gould 1970) is that the energy of photons scattered by ultra relativistic electrons of energy γmc^2 is,

$$E_{after} \approx \frac{4}{3}\gamma^2 E_{before}$$

If the original photon is of a low enough energy in the rest frame of the electron,

$$\gamma E_{before} < m_e c^2$$

then the Klein-Nishina cross section, $\sigma_{K\text{-}N}$, for interaction is

$$\sigma_{K\text{-}N} = \pi r_e^2 \frac{1}{\varepsilon}\left\{\left[1 - \frac{2(\varepsilon+1)}{\varepsilon^2}\right] ln(2\varepsilon+1) + \frac{1}{2} + \frac{4}{\varepsilon} - \frac{1}{2(2\varepsilon+1)^2}\right\}$$

where $\varepsilon = h\omega/2\pi m_e c^2$, and reduces to the Thomson cross section σ_T, for low energy photons $\varepsilon \ll 1$,

$$\sigma_{K\text{-}N} = \frac{8\pi}{3} r_e^2 (1 - 2\varepsilon) = \sigma_T (1 - 2\varepsilon) \approx \sigma_T = 6.653 \times 10^{-29}\ m^2$$

Hence for low energy photons the interaction cross section, see figure 1.9, is large

enough to make the inverse Compton effect an efficient mechanism for the production of VHE Gamma-ray photons.

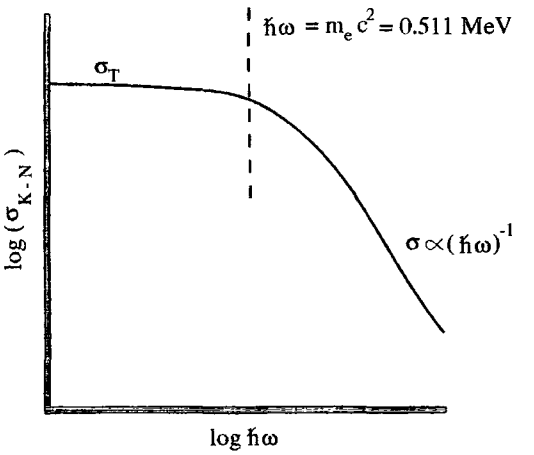

Figure 1.9: A schematic diagram of the steep K-N cutoff in the interaction cross section between electrons and photons.

1.3.5 Pion decay

The mechanisms described in sections 1.3.1 through 1.3.4 have all been concerned with the production of high energy photons through the interactions of relativistic electrons. One important mechanism remains that involves the interactions of high energy nucleons with matter. When a high energy proton interacts violently with another free proton, or with a nucleon, charged and neutral pions are the principal products. Neutral pions are very short-lived mesons, with a half life of ~ 8.4×10^{-17}s and a mass m_π = 135 MeV/c^2, they have a preferred decay path that produces two photons with energy $E_\gamma = m_\pi c^2/2$ in the pions' rest frame. In proton-proton, proton-nucleon interactions at high energies, the pions produced may have very high Lorentz factors, resulting in the decay products being both beamed in the direction of the pion's motion and boosted to much higher energies.

1.4 VHE photon attenuation

There are only a few mechanisms by which VHE photons may be absorbed. Unlike low energy photons, VHE photons are not generally absorbed by matter in intergalactic or interstellar space as they have large radiation lengths within matter (about 25 g cm^2). The typical column density in intergalactic space is < 10^{-5} g cm^2 Mpc^{-1}, hence even over cosmological distances absorption by matter is negligible. There may be some absorption within dense interstellar dust clouds where the column density is much higher but this is of little concern to VHE astronomy. The principal absorption mechanism for VHE photons is interactions with low energy real photons, High energy photons may also be absorbed through electron pair production process as a result of their interaction with low energy photons. For the transition,

$$\gamma_{real} + \gamma_{real} \rightarrow e^+ + e^- \quad or \quad \gamma_{real} + \gamma_{virtual} \rightarrow e^+ + e^-$$

to occur, the energy in the centre of the momentum frame must be at least twice the rest mass energy of the electron E_e, where $2E_e = 1.22MeV/c^2$. So, for a 1TeV photon colliding head on with a low energy photon, the centre of the zero momentum frame would need to have a Lorentz factor of $\gamma_L = 1TeV / E_e$ to produce an electron positron pair. Given this Lorentz factor, and the requirement that momentum is conserved in the zero momentum frame, the resultant electron positron pair will have a considerable amount of kinetic energy in the observer's frame.

For photon-photon interactions of one photon with energy E_{source} and momentum vector separated by θ degrees relative to a background photon of energy E_{bg}, the

energy of E_{bg} will be,

$$E_{bg} \geq \frac{1}{E_{source}} \left(\frac{2E_e^2}{1 - cos\theta} \right)$$

The cross-section for this process for the case of head on collisions in the ultra relativistic limit is

$$\sigma_{pp} = \pi r_e^2 \frac{m_e^2 c^4}{E_{source} E_{bg}} \left[2ln \left(2 \frac{\sqrt{E_{source} E_{bg}}}{m_e c^2} \right) - 1 \right]$$

where r_e is the classical electron radius (Ramana Murthy & Wolfendale (1986)).

There are a number of astrophysical situations in which this mechanism will be important. The principal locations are summarised in table 1.

Background	Example Location	E_{bg}(eV)	E_{source}(eV)
Cosmic Microwave Background	Extragalactic Space	6×10^{-4}	4×10^{14}
Starlight	Interstellar Space	2	10
X Ray	Neutron Stars	10^3	3×10^8

Table 1: Examples of astrophysical locals of background photon fields, of energy E_{bg}, where electron pair production is an important factor in the attenuation of gamma-ray photons of energy E_{source}.

1.5 Fundamental physics with TeV observations

Although the primary aim of TeV gamma-ray astronomy was originally to investigate the origins of cosmic-rays, a question which still awaits a clear answer, the physics objectives have now become much broader. This field has become part of the general quest to understand the mechanisms involved in many astronomical sources. The

extent of the current physics objectives may be summarised as follows (taken from Lorenz (2001)):

1) The study of gamma-ray emission and particle acceleration by supermassive black holes inside active galactic nuclei.

2) The search for VHE gamma-ray emission from violent, extragalactic gamma-ray bursts (GRB).

3) The study of shell type supernova remnants, which are considered to be plausible sources of cosmic-rays.

4) The study of plerions, i.e. synchrotron nebulae powered by active pulsars, such as the Crab, to explore relativistic pulsar winds.

5) The search for a variety of galactic objects showing sufficient energy release for particle acceleration in shock waves or jets such as accreating binaries, microquasars, cataclysmic variables, etc.

6) Constraints on stellar formation at early epochs through measurements of the IR extra galactic radiation field.

7) The search for possible topological defects and relic particles left over from the early universe.

8) The search for the lightest supersymetric particles. these are assumed to be amassed, for example, at the center of our galaxy. Gamma-rays would be generated in annihilation processes.

9) Tests for quantum gravity effects.

Many of these objectives will likely be familiar to the reader, and have been discussed in detail in a variety of books and review papers. Some of those which exemplify the interesting nature of TeV gamma-ray investigations available using both existing data and dedicated new observations will be covered briefly in the next few subsections; this selection is by no means intended to be comprehensive.

1.5.1 Intergalactic Infrared radiation field

VHE gamma-ray observations are able to place constraints on the intergalactic infrared radiation field (IIRF), and in turn upon star formation rates in the early universe. The background of infrared radiation might have a number of possible causes, though early bursts of star formation would be expected to constitute a significant contributing factor. Other contributors might include pre-galactic star formation, unusual primordial galaxy types and present day star formation. Even the decay of supersymetric particles and other weakly interacting relics of the Big Bang are expected to make a contribution. Although interpretive complications do arise due to the evolution of radiation produced in the early universe, the IIRF is expected to be especially sensitive to rapid star formation periods, and so studies into its nature are of significant cosmological interest.

High energy gamma-ray photons travelling through inter-galactic space will experience some attenuation through photon-photon interactions. The importance of these photon-photon interactions and their effect upon VHE gamma-rays was first noted by Nikishov (1962) in relation to the newly discovered cosmic microwave

background radiation (CMBR). Similarly the high end of the TeV gamma-ray spectra from sources at large distances (e.g. blazars), will be attenuated by interactions with infrared photons.

Further studies into the absorption of TeV gamma-ray photons by infrared and optical photons was conducted by Gould and Schreder (1966), who concluded that determining the exact nature of the IIRF would supply useful constraints on the evolution of stars and galaxies at high redshifts. They also noted the dependence of TeV photon attenuation length on cosmological parameters such as the Hubble constant, pointing to TeV gamma-ray astronomy as a method of probing such parameters. Currently, only upper limits on the intensity of the IIRF have been derived from TeV observations, though much more is expected of the next generation of ground-based instruments. Present TeV observations of Mrk 421 (McEnery 1997) give an upper limit to the IIRF at 20μm of about 4 $nWm^{-2}sr^{-1}$.

1.5.2 Quantum gravity

By making multi-spectral observations [including TeV observations] of distant high energy sources it is possible to place lower limits on the energy at which quantum gravity couples to electromagnetism E_{QG}. Quantum fluctuations within the vacuum of space induce a dispersive effect upon photons. The Amelino-Camelia (Amelino-Camelia (1998)) formulation relates the dispersive time delay Δt of a photon of energy E relative to the light travel time over a distance L, to the energy E_{QG},

$$\Delta t \approx \xi \frac{EL}{cE_{QG}}$$

where ξ is a model dependent quantity ~ 1.

The analysis of a strong TeV gamma-ray emitting flare detected within Mrk 421 observations in 1997 (Catanese et al. (1997a&b)) have enabled a lower limit to be placed on E_{QG} which is four times higher than the theoretical lower limit.

1.5.3 Dark matter

With dedicated VHE gamma-ray observations it may be possible to probe the 'dark matter' content of the universe. It is apparent from observations of galactic rotation profiles, mass estimates of galaxy clusters and elemental abundance as a result of cosmonuclear synthesis, that the majority of mass in the universe must consist of non-baryonic dark matter, with ~1% to ~10% of normal baryonic matter.

One of the many candidates for this 'dark matter' are the 'neutralinos', a type of Weakly Interacting Massive Particle (WIMP), predicted to be the lowest energy resonance of a possible family of stable supersymmetric particles. It is thought that significant quantities of neutralinos would have been produced in the early universe and could have survived to the present day.

Limits placed on the neutralino by accelerator experiments and cosmological arguments constrain their mass to be within the range of $30GeV/c^2$ to $3TeV/c^2$ So, neutralinos may be observable through their neutralino-antineutralino annihilation

channels,

$$\chi + \chi' \rightarrow \gamma + \gamma \; ; \; \chi + \chi' \rightarrow \gamma + Z_0$$

by the new generation of sensitive VHE gamma-ray telescopes (Bergstrom et al. (1998)). As neutralinos possess a mass, they will tend to congregate around massive bodies such as our galaxy, concentrating near the galactic bulge. The bright sky fields, common near the galactic centre, may present a significant problem for neutralino detection as high sky noise levels are problematic for ground-based gamma-ray observations, although the potential for neutralino detection receives a boost from the monoenergetic nature of the neutralino-antineutralino annihilation line. As ground-based observations are taken at continually changing zenith angles, the change in detector threshold with zenith angle acts as a spectral filter. The neutralino-antineutralino annihilation line will cut-off quite sharply at the zenith angle for which the IACT threshold meets the annihilation line energy. This effect renders inherently weak and extended signals much easier to detect. The possible detection of the neutralino is one of many reasons for development of next generation of gamma-ray telescopes.

CHAPTER TWO - Cherenkov Radiation and Extensive Air Showers

2.1 Introduction

In order to investigate high energy radiation from astronomical sources it is usually necessary to observe from a platform above the Earth's atmosphere, as the atmosphere forms a very effective barrier to radiation from ultraviolet and higher energies. As a result, observations in the high energy regime of the electromagnetic spectrum have generaly been confined to either balloon or space based detectors.

The recently decommissioned Compton Gamma-Ray Observatory (CGRO), shown in figure 2.1, has been the most notable of the high energy space based observatories. The CGRO contained four experiments: OSSE - the Orientated Scintillation Spectroscopy Experiment (0.5 to 10MeV), BATSE the Burst and Transient Source Experiment (30keV to 1.9MeV & 15keV to 110MeV), COMPTEL - the Compton Telescope (0.8 to 30MeV) and finally EGRET - the Energetic Gamma-ray Experiment (10MeV to 30GeV). CGRO was launched in 1991 and, over the lifetime of the EGRET detector, recorded 271 distinct gamma-ray sources (Hartman et al. (1999)) in the energy range 10MeV to 20GeV.

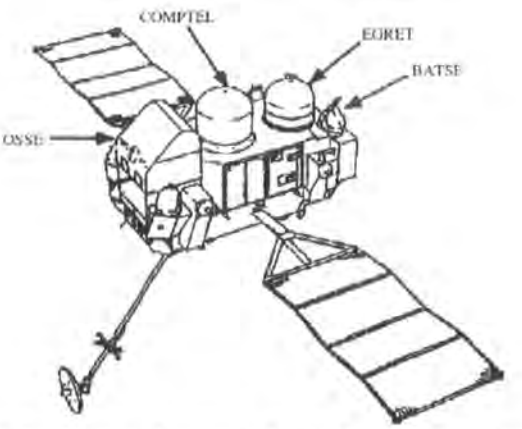

Figure 2.1 Location of the various detectors aboard the Compton Gamma-Ray Observatory. (Taken from: Fishman, et al. 1992).

There is at this time (late 2001) no space-borne instrument which is able to detect gamma-rays in the 10MeV to ~100 GeV energy range, although this will be rectified by the planned Launch of the AGILE and GLAST satellites.

The AGILE satellite, part of the Italian Space Agencies' program for small scientific missions, has a forseen launch in early 2004 and will be devoted to gamma-ray observations in the 30 MeV to 50 GeV range. It is most notable for its large field of view (1/5th of the sky) which makes it ideal for monetering gamma-ray sources like AGN and unidentified galactic sources, for the discovery of gamma-ray transient and gamma-ray bursts, and for the study of diffuse galactic emission and the identification of gamma-ray pulsars.

The GLAST satellite which is part of NASA's Office of Space and Science Strategy Planning program for space observatories, has an anticipated launch date in 2005 (Kniffen, Bertsch and Gehrels (2000)). GLAST is a next generation high-energy

gamma-ray observatory designed to make observations of celestial gamma-ray sources in the energy range extending from 10 MeV to more than 100 GeV, following in the footsteps of the CGRO-EGRET experiment. GLAST will have a field of view about twice as wide (FOV > 2.5 steradians), and sensitivity about 50 times greater than that of EGRET at 100 MeV. GLAST's two year flux limit for source detection in an all-sky survey should be ~1.6 x 10^{-9} photons cm^{-2} s^{-1} (at energies > 100 MeV). GLAST should be able to locate sources between positional accuracies of 30 arc seconds to 5 arc minutes, depending on energy. Beyond the EGRET AGILE and GLAST energy ranges the size and cost of experiment needed to detect the low fluxes of increasingly penetrating radiation becomes prohibitive.

Over the past decade ground-based methods have opened up a new astronomical window for gamma-rays with energies above ~30GeV. Gamma-rays above these energies interact with the Earth's atmosphere inducing electronic cascades (Extensive Air Shower (EAS)). The Cherenkov radiation emitted from shower particles may be detected as a very short faint flash of blue light by sensitive ground-based detectors; this is the basis of the Atmospheric Cherenkov Technique (ACT). A complication with this technique is that high energy gamma-rays are not the only progenitors of Cherenkov radiation in the atmosphere. Similar flashes of Cherenkov radiation are induced by energetic cosmic-ray particles, predominantly protons, which also initiate EAS and constitute a strong source of background noise. There is a limit to the effectiveness of this technique as at energies below about 30GeV, high energy electrons become a strong and indistinguishable background to gamma-ray observations.

2.2 Extensive air showers

EASs are initiated when a high energy cosmic-ray photon or nucleon interacts with an atom near the top of the atmosphere. Photons and nucleons initiate different types of EAS: electromagnetic and nucleonic, respectively. A primary high energy particle may suffer its first interaction close to the top of the atmosphere, but a significant fraction of the secondary radiation still reaches ground level. It is the lateral extent of the air shower, as well as its penetration through the atmosphere, which is of importance in high energy gamma-ray astronomy, because it means that a detector at ground level which is well away from the path of the primary gamma-ray may still record a signal from the secondary radiation.

The depth of the atmosphere provides latitude for the showers to spread laterally, hence secondary emission from the shower particles is spread over a large area on the ground. This results in a much larger effective area for ground-based detectors than their physical size would suggest. The ground-based observation of EAS is therefore an effective method of studying the very highest gamma-ray energies, though much needs to be known about the nature of EAS for practical observational use to be made of them. A complicating factor in the observation of gamma-ray induced EAS is the relatively strong background of nucleon-induced EAS, which must be suppressed.

2.2.1 Photon initiated EAS

An electromagnetic EAS starts near the top of the atmosphere when a high energy gamma-ray undergoes pair production, producing a relativistic electron-positron pair. Direct interactions with nuclei are also possible but have a lower probability of ~ 2.8 x 10^{-3}. This results in an EAS which is principally electromagnetic in nature. The electrons (e^+ & e^-) then undergo Bremsstrahlung interactions with other atoms along their path, resulting in the emission of further lower energy gamma-rays. The particle shower will continue to grow geometrically until the average particle energy in the shower reaches the 'critical energy' for air, E_c ~ 80MeV. Below this energy ionisation becomes the principle energy loss mechanism. The cross section for ionisation rises sharply as the electron energy falls and the cross-section for Bremsstrahlung falls along with the electron energy. The combined result is that the electrons in the shower which fall below this critical energy rapidly lose the remainder of their energy and the production of gamma-rays via Bremsstrahlung is reduced. Combined with the diminishing cross section for pair-production and the increasing effects of Compton scattering and photoelectric absorption, the shower's continuing growth is staunched.

A simple model which outlines the main features of an electromagnetic EAS in the atmosphere has been given by Allan (1971). In this simple model the interaction length for Bremsstrahlung X_0, is approximated to the interaction length for pair production $X_p = 9/7X_0 = 37g\ cm^{-2}$, so that the probability of interaction is half at some distance X_R, given by, $X_R = X_0 \ln 2$. A further approximation is that the energy of the initial gamma-ray E_0, is equally divided in each interaction, so that the energy

of each particle is $E = E_0/2^n$ after n interactions. Given these assumptions, the resultant shower will be composed of equal numbers of electrons, positrons and gamma-ray photons, shown schematically in fig 2.2.

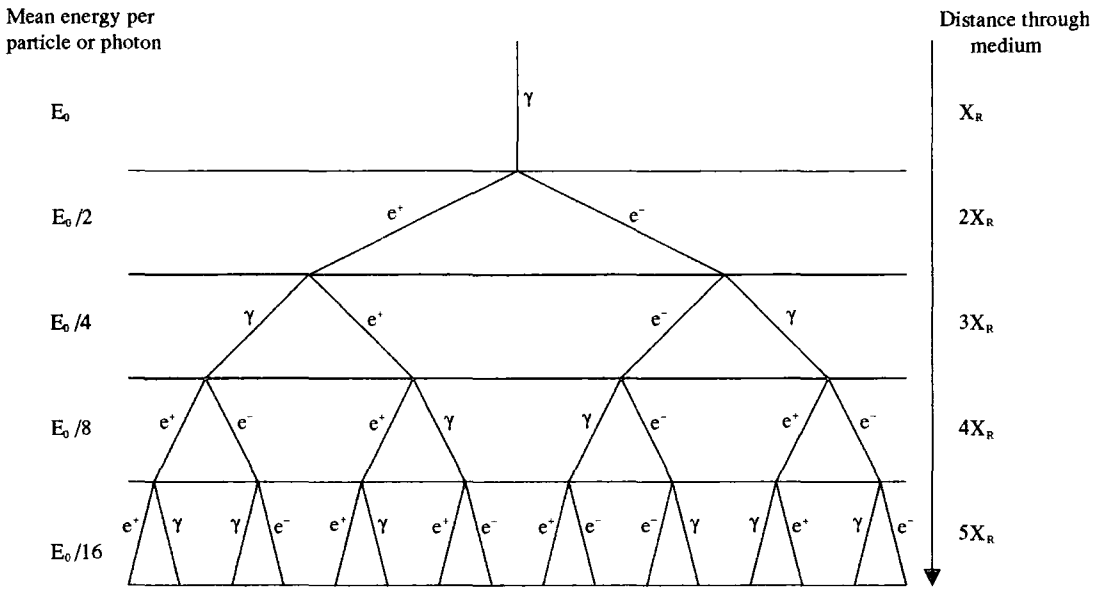

Figure 2.2: A simple model of a gamma-ray initiated EAS (Longair (1997) Vol 1).

The maximum number of particles $N_{max} \sim E_0/E_c$, is reached at a depth $X_{max} \sim X_0 \ln(N_{max})$, in the atmosphere. It is possible to estimate the *height of maximum* of a simplified EAS of the type described above if one assumes an approximate model of the atmosphere. Given an atmosphere with a total depth of 1000g cm^{-2} and a scale height of ~7km, the height of maximum for a gamma-ray photon of about 300 GeV would be ~8km above sea level. In reality the height of maximum for a typical 300 GeV gamma-ray EAS would be at a somewhat higher altitude, as the electrons in the shower suffer from some continual energy loss through ionisation of the atmosphere.

2.2.2 Nucleon Initiated EAS

The development within the atmosphere of EAS initiated by high energy cosmic-ray nucleons is inherently more complex than those with photon progenitors, see figure 2.3. A nucleonic cascade is initiated through the process of *pionisation* in which a high energy nucleon collides with the nuclei of an atom within the atmosphere. Approximately half of the incoming nucleon's energy is transferred to secondary nucleons liberated from the target nuclei and transformed into the production of pions.

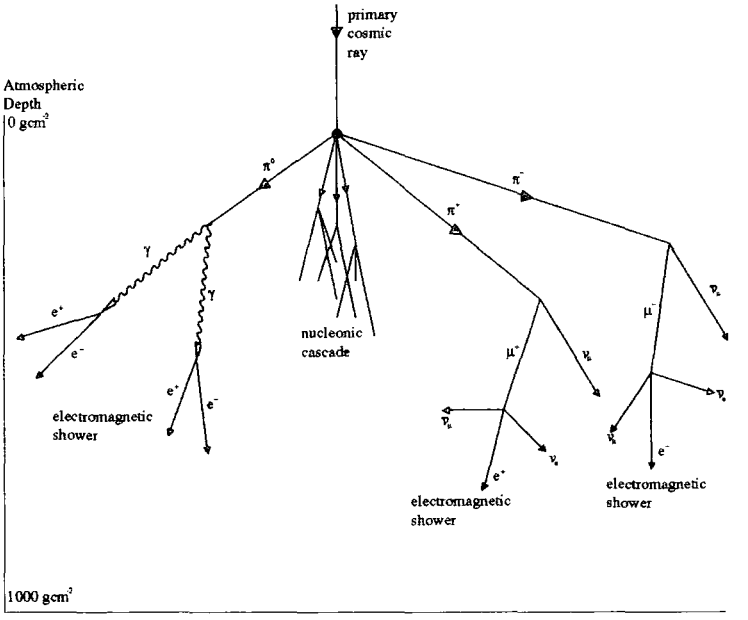

Figure 2.3: A schematic diagram of a nucleon initiated EAS (Longair (1997) Vol 1).

The nuclear debris from this initial collision will have sufficient energy to multiply in successive generations of nuclear collisions, until the point at which the energy per particle drops below that required for multiple pion production (about 1GeV).

The pion component has three forms, π^+, π^- and π^0, where the π^0's are the simplest of these to consider, as they have very short mean lifetimes (8×10^{-17} s) and decay with 99% probability into two gamma-rays, each of which initiates an electromagnetic cascade, developing in an identical fashion to those discussed in the previous section. Charged pions behave differently to neutral pions; they have a much longer lifetime of 1.2×10^{-8} s, and decay into even longer lived muons 2.2×10^{-6} s, which lose only a small fraction of their energy via ionisation (about 10^{-3} g^{-1} cm^2) with an even smaller amount lost via bremsstrahlung 10^{-4} g^{-1} cm^2. A proportion of the muons, i.e. those with Lorentz factors >>20, survive to sea level. the remainder of muons with Lorentz factors <20 decay in the atmosphere and produce an electron or positron which may seed a further low energy electromagnetic shower. The elemental composition of cosmic-ray nuclei at the top of the atmosphere is dominated by protons (87%), the remainder being composed mostly of ^{4}He (12%), with a trace of heavier nuclei. This composition is well measured below 1TeV; above this energy the elemental abundance of cosmic-rays is not as well known.

The different species of nuclei initiate a slightly different EAS. For instance, the interaction length for pionisation decreases with increasing mass number. On average a 1 TeV proton will have an interaction length of about 83 g cm^{-2}, while an Iron nucleus will have a much lower interaction length of roughly 2 g cm^{-2}. The production of muons observed from nucleonic EAS is also affected by the mass number, A, of the initiator; the number of muons produced is proportional to $A^{0.24}$.

2.2.3 Lateral development of EAS

The lateral spread of shower particles in electromagnetic EAS is dominated by multiple small Coulomb scattering of electrons and positrons in the electromagnetic fields of nuclei in the atmosphere. The root mean square scattering angle is inversely proportional to the energy of the shower particles, and ranges from less than one degree for energetic ~1 GeV electrons to about 10 to 15 degrees at shower maximum. The interactions which give rise to these multiple scatterings are also those which are responsible for the production of Bremsstrahlung. It is possible, then, to express the multiple scattering in terms of the interaction length for Bremsstrahlung, X_0. The overall scattering angle, Θ, for a large number of small scattering angles, θ_i, over a path length d is,

$$\Theta^2 = \sum_{i=1}^{i=n} \theta_i^2$$

where

$$\Theta^2 = \frac{d}{X_0}\left(\frac{21\ \text{MeV}}{E}\right)^2 .$$

For an electron at shower maximum, $E \approx E_c$, the opening angle over one interaction length, $d = X_0$ would result in a mean angular deflection, Θ of about 15°.

The lateral spread due to pair production and Bremsstrahlung is quite small. For pair production this is due to strong relativistic beaming. For photons produced via Bremsstrahlung, the small deviations are of a lesser extent than that of the electrons. In the case of nucleonic EAS, the shattering of the nucleus during pionisation results in a small number of nucleonic fragments. These fragments collide with other nuclei

in a narrow range of angles to the path of the initiating particle, producing further subshowers. The pions emerge in a wider beam relative to the path of the initiator, with lateral momentum components of the order 100-200 MeV c^{-1}. High energy protons and/or neutrons from the initial collision will collide with other nuclei and produce further subshowers. Although the main constituents of nucleonic-initiated EAS are photons, electrons and positrons, the pion component gives rise to electromagnetic components early in the shower development, resulting in a wider, more penetrating, though less ordered, shower, see figure 2.4.

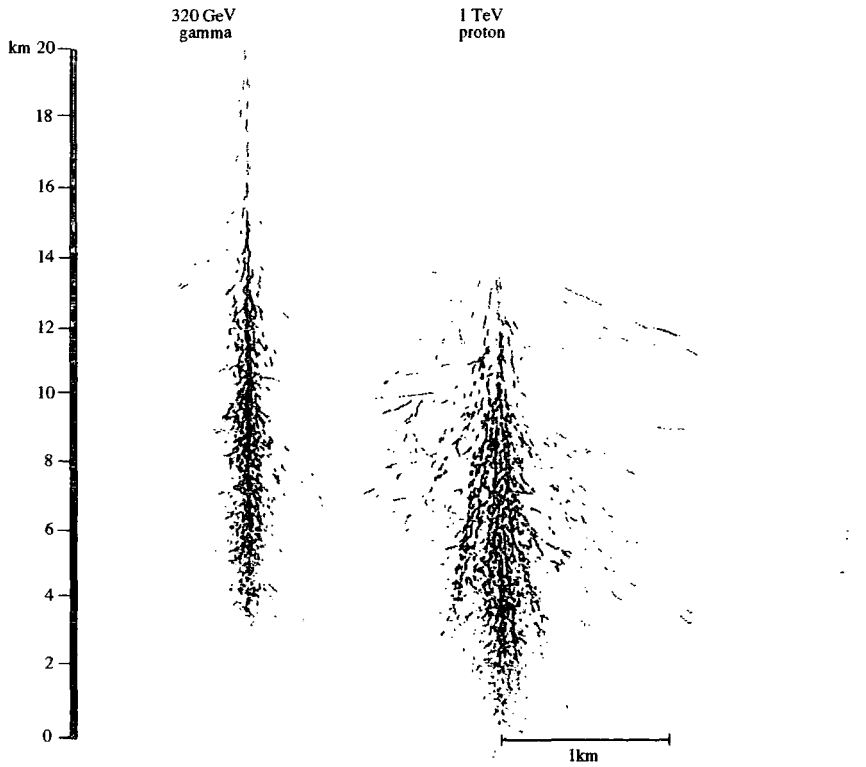

Figure 2.4: Simulations of EAS for a 320 GeV gamma-ray and a 1 TeV proton primary, showing all Cherenkov emitting particles. Although the proton has three times the primary energy of the gamma-ray the height of maximum are similar at ~ 9km. Note: the horizontal scale in this figure is roughly four times the vertical scale. Adapted from Hillas (1996).

2.3 Cherenkov radiation

The phenomenon of a faint blue glow emitted from transparent materials located near strong radioactive sources has become known as the Cherenkov effect. The effect had been noticed in the late 19th century by physicists working with concentrated radio active materials. Heaviside supplied a classical explanation for the effect, which appeared in 'The Electrician' (Heaviside 1890). Heaviside derived the correct relations for Cherenkov photon production and the Cherenkov emission angle. Considerable time passed until further investigations into the precise nature of this radiation where conducted. The research of Mallet in the 1920s (Mallet (1926) (1928) and (1929)) and Cherenkov in the 1930s (Cherenkov (1937)) resulted in the identification of energetic charged particles as the cause of the emission, though it was not until Ginzberg (1940) that a fully quantum mechanical explanation was proposed.

2.3.1 Cherenkov radiation (background)

The following description of the Cherenkov effect has been based on the quantitative explanation given by Jelley (1958). Considering a charged particle moving with velocity V through a transparent medium with refractive index,

$$n = \frac{c_{vacuo}}{c_{medium}} .$$

The electric field of the charged particle will have a local polarizing effect on the atoms/molecules within the medium. If the particle travels with $V < c/n$, then its electric field will distort the atoms/molecules of the medium symmetrically about the

particle's position. However, a particle travelling with $V > c/n$, will be travelling faster than any influence can be transmitted within the medium. This results in a dipole being induced in the atoms/molecules behind the particle, but with no corresponding dipole in front of the particle (see figure 2.5). Thus the symmetry is broken along the axis of motion and a resultant electromagnetic pulse emanates from the distorted atoms/molecules directly behind the particle's position.

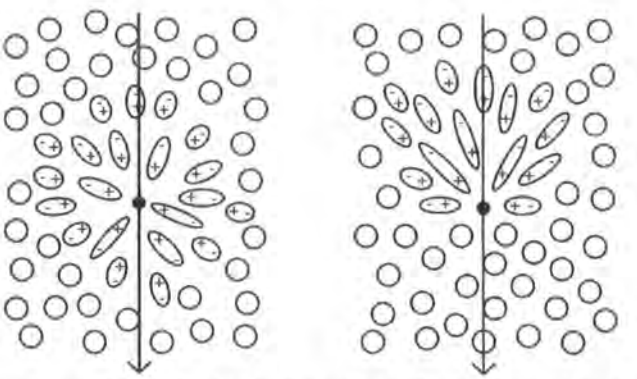

Figure 2.5: An illustration of polarisation in a medium, due to the presence of a charged particle. In this case, a negatively charged particle, a) when V < c/n and b) when V> c/n.

This emission will constructively interfere only in certain directions, illustrated by the Huygens construction in Figure 2.6.

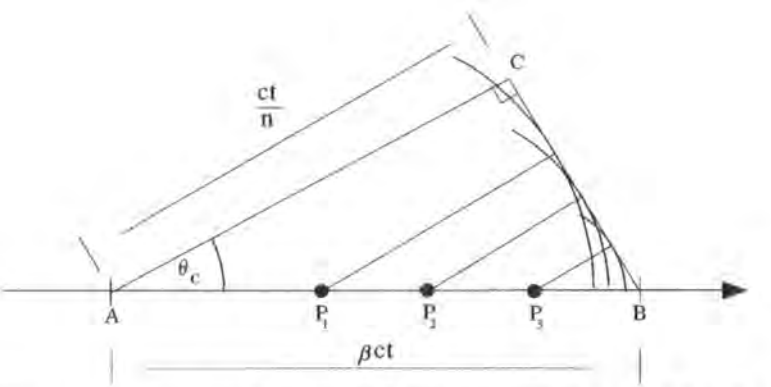

Figure 2.6: A Huygens construction for a charged particle moving along, AB with velocity V > c/n, within a medium of refractive index n. The particle emits Cherenkov radiation at points P. Constructive interference will occur along the tangent CB, giving rise to Cherenkov emission over the surface of a cone with semi-vertical angle *(90–θ)*.

A charged particle with velocity $V = \beta c$ travels a distance AB $= \beta ct$, in a time t. Over this same time light emitted at point A will have travelled a distance, d = ct/n = AC. The individual wavelets emitted at points P_i throughout the particle's track will interfere constructively along the tangent CB, to produce a plane wave at an angle, θ_c = CAB to the particle's velocity vector AB. The angle θ_c, can be shown to be

$$\cos \theta = \frac{AC}{AB} = \frac{1}{\beta n} .$$

For a charged particle travelling faster than the phase velocity of light, the symmetry of polarization is broken along the axis of motion but is preserved in the azimuthal plane. Thus, emission occurs over the surface of a cone with its apex at point A and opening angle θ_c. Cherenkov radiation is only emitted by charged particles travelling faster than the phase velocity of light in a particular medium; thus β is constrained to be at least 1/n. Therefore,

$$\beta_{min} = \frac{1}{n} .$$

and the upper value of β is,

$$\beta_{max} = 1$$

Due to the constraint that the particle cannot travel faster than the speed of light in a vacuum, the limits of β effectively constrain the emission angle of the Cherenkov radiation to be within the range.

$$0 < \theta < \cos^{-1}\left(\frac{1}{n}\right) \quad .$$

The refractive index of transparent materials is a function of wavelength λ so θ_c will be a function of the wavelength of the emitted photons. Cherenkov photons are not emitted if the refractive index in a region of the spectrum is less than or equal to than unity, $n(\lambda) \leqslant 1$, or if the material absorbs at a particular wavelength. For air, Cherenkov emission is limited to the near ultra-violet and visible regions of the electromagnetic spectrum.

2.3.2 Cherenkov radiation in the atmosphere

The possibility of Cherenkov light being produced as a result of EAS was first suggested by Blackett (1948) and detected four years later by Galbraith and Jelley (1953a&b). The Cherenkov radiation sampled at ground level is a product of the complete shower development history, and provides vital information regarding the identity of the primary particle and the amount of energy dissipated within the atmosphere during shower development. The charged particles which are produced in EAS are of suitably high energy to produce Cherenkov radiation, despite the relatively low refractive index of air, n = 1.000293, at standard temperature and pressure (STP).

The refractive index of air is even lower at the altitude at which typical EAS reach their maximum particle numbers. The refractive index of air is closely related to the air pressure which decreases exponentialy with altitude in a simple model of the atmosphere. Assuming that $n = 1 + \eta$, it can be seen that $\eta(h)$ is an exponential

function of altitude,

$$\eta(h) = \eta_{STP}\, e^{-\frac{h}{h_0}}$$

where h_0 is the scale height of an exponential atmosphere of ~7km.

The minimum Lorentz factor ($\gamma = 1/(1-\beta)^{0.5}$) required to produce Cherenkov radiation can be found using β_{min},

$$\beta_{min} = \frac{1}{\sqrt{2\eta}}$$

as long as η remains small.

The kinetic energy of a particle E_{ke} is given by $(\gamma - 1)mc^2$. The threshold energy, E_T, below which no Cherenkov emission occurs is then simply,

$$E_T = mc^2 \left(\frac{1}{\sqrt{2\eta}} - 1 \right) .$$

The energy thresholds at sea level for differing species of charged particles are as follows: electrons 21 MeV, muons 3.4 GeV, pions 5.6 GeV, protons 38 GeV and Helium nuclei 151.5 GeV. The majority of the Cherenkov light from EAS is therefore due to the electrons and positrons in the shower, as they are more numerous and have a considerably lower threshold energy for photon production than any other particle. Cherenkov photons will be emitted over a very small opening angle, $\theta_{max} = (2\eta)^{0.5}$, about 1.4 degrees at sea level.

Frank and Tamm (1937) showed that for an electron moving through a uniform dielectric medium the energy radiated over the path length *dl* is given by

$$\frac{dE}{dl} = \frac{\pi z^2 e^2}{\varepsilon_0} \int \left\{1 - \left(\frac{1}{n\beta}\right)^2\right\} \frac{d\lambda}{\lambda}$$

integrated over the range $n\beta > 1$, where $\alpha = 1/137$ is the fine structure constant, z is the charge on the particle, e is the electronic charge, and ε_0 is the permittivity of free space. The photon production rate between λ_1 and λ_2 from a single electron (neglecting dispersion) is given as,

$$\frac{dN}{dl} = 2\pi\alpha\left(\frac{1}{\lambda_1} - \frac{1}{\lambda_2}\right) \cdot sin^2\theta$$

For an electron at shower maximum the photon yield at sea level, over a path length of 1 meter, due to the passage of a highly energetic electron $E >> E_T$ will be about 30 photons, emitted in the wavelength interval from 300 to 500 nm. At higher altitudes the yield of Cherenkov photons would be much less as the refractive index is much less, and in addition the Cherenkov emission angle, θ, would also reduce (see figure 2.7). The energy loss due to the emission of Cherenkov photons represents a relatively small fractional energy loss for the electron compared to ionisation or Bremsstrahlung.

As the Cherenkov photons propagate through the atmosphere, a number of attenuation mechanisms are important. These include Rayleigh scattering, ozone absorption and aerosol scattering. As a result of these processes, approximately half the Cherenkov photons produced within an EAS in the wavelength interval from 300 to 500 nm will be absorbed or scattered before reaching sea level.

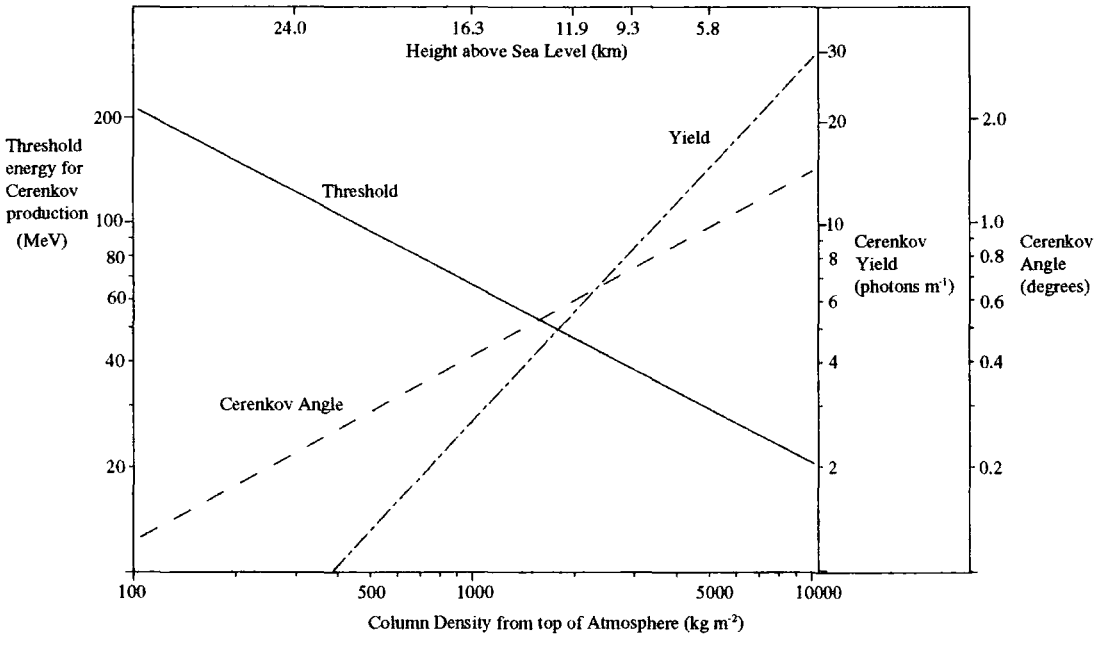

Figure 2.7: Variation with atmospheric depth of different properties of Cherenkov radiation (Ramanamurthy and Wolfendale, 1986)

As a result of the low refractive index of air, Cherenkov photons almost catch up with the particles which emit them; thus the photons arrive at the ground in a short pulse. The pulse length can be approximated by,

$$\Delta t = \frac{d}{c}\left(\frac{n-1}{n}\right)$$

where d is the length over which photons are emitted, usually a few km, giving a pulse period of a few ns. The extent over which the Cherenkov photons are spread on the ground can be roughly determined by considering the Cherenkov emission angle at height of maximum, about 1 degree, at about 8km altitude, for a 300 GeV gamma-ray. This would suggest that the light would fall in a pool of around 140 meters in radius.

2.3.3 Cherenkov radiation from VHE gamma-ray EAS

The principal feature of gamma-ray-induced EAS in the atmosphere is that they are essentially long and relatively narrow beams of energetic electrons and positrons. The short energy independent interaction length (37.7 g cm^{-2}) for VHE gamma-ray photons means that the shower starts high in the atmosphere. Except for the very highest energy photons the shower dies out at a few km above ground level as ionisation losses become large (~4km for a 300 GeV primary photon).

High in the atmosphere, the emission angle for Cherenkov radiation is about 1 degree; this angle will increase as the shower develops deeper into the atmosphere, to a maximum of 1.4 degrees at sea level. The increasing Cherenkov emission angle and the reducing altitude at which photons are emitted combine to produce a focusing effect in the Cherenkov light pool on the ground, see figure 2.8. The photon lateral density function (LDF) of the Cherenkov light pool rises from a plateau near the shower axis to a prominent ridge or 'hump' (at about 100 m) from the shower axis before falling away quickly (Rao & Sinha, 1988). The light in the plateau region of the LDF is dominated by emission from particles in the tail of the shower nearest the observer; it is thus subject to large fluctuations from shower to shower. Showers initiated by gamma-rays with several TeV of energy may produce electrons which penetrate to ground level and produce localised peaks of Cherenkov light within the pool (Hillas & Patterson, 1990).

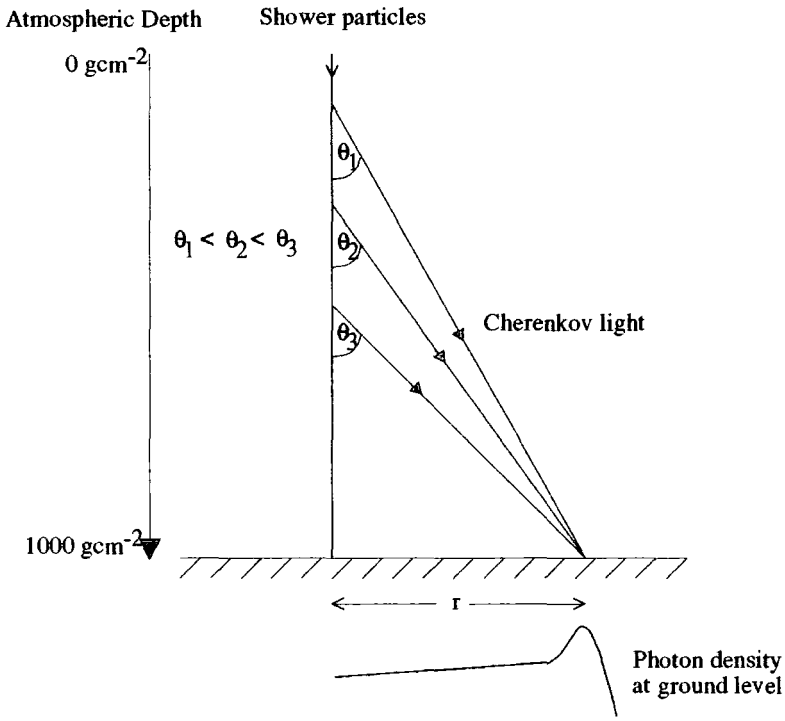

Figure 2.8: Schematic diagram showing the focusing effect of changing Cherenkov emission angle with atmospheric depth.

Light in the region of the 'hump' is dominated by emission from energetic, (E > 1GeV) electrons which tend not to be deviated from their almost parallel paths, so that the radius of the 'hump' can be directly related to the Cherenkov emission angle and altitude of the emitting particles. Beyond the 'hump' the light falls off as $1/r^2$. this light is due to low energy electrons which have been deflected from the main axial path of the majority by multiple coulomb scattering, see figure 2.10.

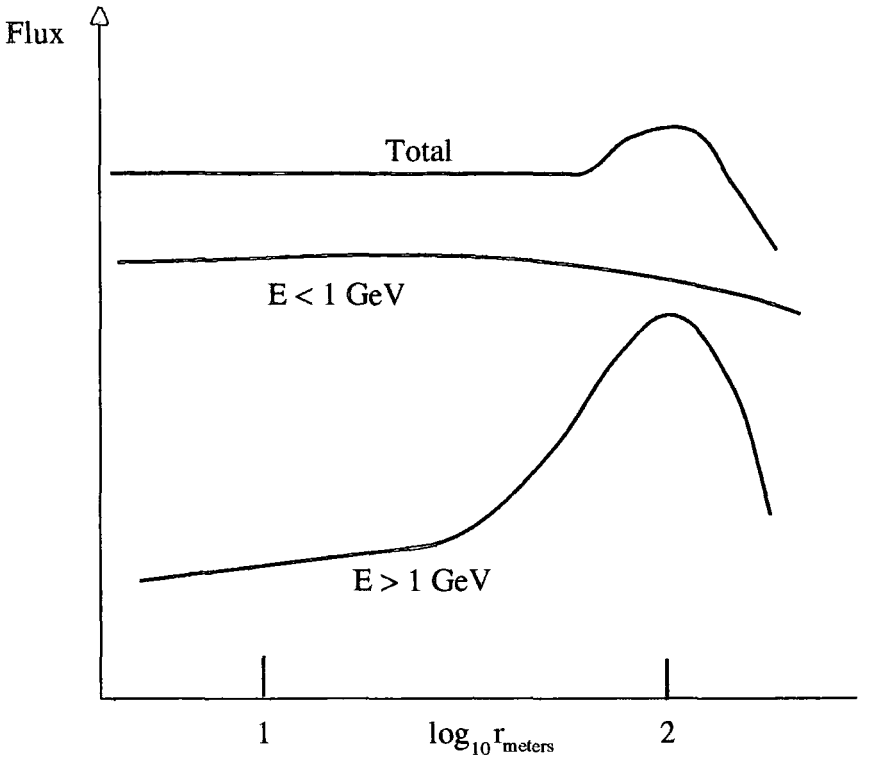

Figure 2.10: Contributions to the overall Cherenkov light profile on the ground from electrons of different energies (Rao & Sinha, 1988).

2.3.4 Cherenkov radiation from nucleonic EAS

The interaction length for a 1 TeV proton in the atmosphere is ~83 g cm^{-2}, which is significantly longer than for a typical gamma-ray. Energetic protons therefore tend to penetrate deeper into the atmosphere. Nucleonic EAS may be thought of as a collection of electromagnetic showers, maximising deep in the atmosphere and all pointing in slightly different directions. This leads to a photon distribution on the ground which is peaked about the shower axis and drops away with distance. There is no 'hump' observed in the light distribution of nucleonic EAS, as the light from the

numerous small electromagnetic showers combine to smear out any net focusing effect (Rao & Sinha, 1988).

Superimposed on the main broad light distribution are localised intense peaks due to electromagnetic showers initiated by energetic electrons produced in low altitude pion decay. In a typical 1 TeV proton initiated EAS, a few tens of muons will be produced and will easily penetrate to ground level. These muons produce intense peaks of Cherenkov emission and may fall anywhere within several hundred meters of the shower axis.

2.3.5 Cherenkov photon yields from EAS

Investigations into the emission of Cherenkov photons have found that gamma-ray and cosmic-ray proton-initiated EAS at the same primary energies yield different quantities of Cherenkov light, (Turver & Weekes 1978). Proton-initiated EAS produce less Cherenkov emission relative to gamma-rays and this differential increases as primary energy reduces. The reason for this reduction is that pions and muons created in the cascade absorb an increasingly larger fraction of the total energy budget at lower primary energies. This results in less energy being available for the production of electrons and positrons, which are the most efficient producers of Cherenkov photons due to their much lower mass and thus Cherenkov emission thresholds.

The electrons created in nucleonic showers will tend to have lower energies and are thus more susceptible to Coulomb scattering (see section 2.2.3) resulting in a wide

diffuse pool of photons on the ground. Monte Carlo simulations of Cherenkov photon yields show that the ratio of yields for equivalent energy gamma-ray and proton primaries change from a factor of ~2 at 1TeV to ~10 at 0.1TeV, at core distances of 100m (Shaw (1999)).

2.3.6 Images of Cherenkov radiation from EAS

As has been discussed in Sections 2.2.1 to 2.3.5 there are considerable intrinsic differences between both the shower development and resultant distribution of Cherenkov radiation from gamma-ray and cosmic-ray initiated events. These differences are due to the physical processes at work in the cascade development, producing different secondary particle distributions within the shower. The differences in Cherenkov light distribution are used as a discriminator between shower initiating particles to provide improved noise reduction when analysing observational data of potential gamma-ray sources. In practice this is achieved by recording an image of the Cherenkov flash in a simple camera arrangement, consisting of an array of photomultiplier tubes at the prime focus of a large focusing mirror. Before going in to detail about the detection of gamma-rays via their Cherenkov images (see section 4.3), it would be useful to review the main points which characterise the differences observed between EAS initiated by gamma-ray and cosmic-ray primaries.

Gamma-Rays: As discussed in section 2.2.1, a photon primary will initiate an electromagnetic cascade high in the atmosphere. This cascade will travel forward along the arrival direction of the initial photon and will be highly constrained in its lateral extent (see section 2.2.3). Except for the very highest energy photons, the cascade will die out due to increasing ionisation losses at an altitude of a few kilometers above sea level.

The Cherenkov light emitted from the charged shower particles, (mainly the electrons and positrons) forms an elliptical 'image' when viewed by a camera arrangement at ground level. Perspective effects result in the major axis of this elliptical image being aligned along the arrival direction of the initiating gamma-ray photons, essentially a point source in the sky. This results in a relatively small elliptical image, about 0.1 to 0.3 degrees wide, which is well aligned with the direction of the gamma-ray source. Thus the images of gamma-ray induced EAS will appear in the camera to radiate like the spokes of a wheel around the 'hub' of the source position.

Cosmic-Rays: In Section 2.2.1 it was stated that a proton primary will generally initiate a nucleonic cascade at a greater depth within the atmosphere than would a photon of the same energy. Pions produced by nuclear interactions have large transverse momenta, which results in a wide lateral development of the shower. Penetrating particles, such as muons, produce local peaks of Cherenkov emission within the light pool on the ground.

An 'image' of a nucleonic EAS will therefore generally be broad and irregular in shape, with no preferred orientation. The variety of possible light distributions on the ground from a nucleonic EAS means that their 'images' may sometimes appear very similar to the image of a gamma-ray EAS in medium resolution detectors, though they are generally quite distinct.

CHAPTER THREE - Ground-Based Gamma-Ray Astronomy

3.1 Introduction

The first observations of Cherenkov radiation from EAS were made by Bill Galbraith and John Jelley during the 1950s (Galbraith and Jelley (1953a) Galbraith and Jelley (1953b) Jelley and Galbraith (1955)). Their apparatus consisted of a photomultiplier tube located at the prime focus of a 25cm diameter parabolic mirror. The detection of EAS particles by a local air shower array was used to ensure that it was indeed Cherenkov light from EAS which was triggering the system and not other effects, such as distant lightning or meteor shower trails. It was realised that these early phenomenological experiments offered a real possibility for the detection of discrete gamma-ray sources at TeV energies, using rudimentary Cherenkov telescopes based around this atmospheric Cherenkov technique to provide large collection areas, for the detection of anisotropy in the arrival directions of cosmic-ray EAS.

Actual astronomy in the TeV range is commonly thought to have begun with the prediction by Cocconi (1959) that the Crab Nebula should be observable with contemporary instrumentation, though Cocconi appears to have been unaware of the work of Galbraith and Jelly and suggested that observations be made using particle detector arrays. Cocconi's paper stimulated new experiments to try to confirm his prediction. The first serious attempt to detect VHE gamma-rays from the region of the Crab nebula was conducted by the Lebedev Institute in Moscow. Their detector

was located in the Crimea and consisted of 12 telescopes each with a $1.5m^2$ collecting area. This experiment produced an upper limit for the VHE gamma-ray emission from the Crab nebula which was two orders of magnitude below that predicted by Cocconi (Chudakov et al. (1965)). Although no emission was detected from the Crab pulsar/nebula by the Lebedev Institute's telescopes, their work did prompt a number of groups to join the field, primarily in Ireland and India.

The development of a new model for TeV gamma-ray emission from the Crab (Gould and Schreder (1965)) helped to maintain interest in ground-based observations even though no detections had been forthcoming. This new model was based around Compton-scattering for synchrotron radiation by relativistic electrons as opposed to neutral pion production, and their consequential decay into two gamma-rays, as was the case for Cocconi's prediction.

Through several decades of continuous development a number of characteristics of the two types of showers (nucleonic and gamma-ray initiated) have been used as possible discriminatory factors. Some of the best developed and well understood methods have been: the presence of penetrating particles (Grindlay (1971)), the ultra-violet excess (Stepanian et al. (1983)), and the shape of the image (Hillas (1985)). In addition, methods were developed for improving the angular resolution of the technique (Gibson et al. (1982)).

The most successful of these techniques, and the one which has shown the highest potential for future improvement, is the Imaging Atmospheric Cherenkov Technique

(IACT). Offering the possibility of improving discrimination against background as well as increased angular resolution using a single optical reflector, the IACT method was first suggested by Hill and Porter (1961) for image intensifiers coupled to small optical systems. A more practical realization was achieved with the use of arrays of photomultipliers in the focal plane of large optical reflectors (Weekes and Turver (1977), Zyskin et al. (1987)).

It had taken many decades of continual effort to develop a method for the reliable detection of a TeV gamma-rays, with the first clear steady flux of VHE gamma-rays being detected from the Crab Nebula by the US/Irish Whipple collaboration in 1989 (Weekes et al. (1989)). This discovery marked the coming of age of VHE gamma-ray astronomy.

3.2 The detection of Cherenkov radiation from EAS

Critical to the detection of gamma-rays by ground-based instruments is the ability to efficiently identify the signals from gamma-ray induced extensive air showers within a very strong background signal of nucleonic cosmic-ray initiated showers.

There are many complications to overcome if usable signals are to be obtained from the Cherenkov emission of EAS. The faint, short duration flashes of Cherenkov light need to be resolved above the ambient night sky background light level, whilst being recorded faithfully and reliably. If a reasonable signal is to be obtained, EAS initiated by gamma-rays have to be effectively distinguished from those caused by the copious

background of nucleonic induced events, and some determination (via simulation) of the efficiency of this discrimination is required for accurate fluxes to be determined. Many techniques are now exploited for ground-based gamma-ray astronomy, with over half a dozen groups throughout the world observing astronomical objects at VHE energies using the IACT method, a summary of experiments is given in table 3.1.

Experiment	Location	Lat.,Long. (°)	Altitude (km)
CANGAROO	Woomera, Australia	31.1S 136.8E	0.2
CAT	Targasonne, France	42.5N 2.0E	1.7
Durham Mk6	Narrabri, Australia	30.5S 150.0E	0.3
HEGRA	La Palma, Spain	28.8N 17.9W	2.2
SHALON	Tien-Shan, Russia	42.0N 75.0E	3.3
TACTIC	Mt. Abu, India	24.6N 72.7E	1.3
Whipple	Mt, Hopkins, USA	31.7N 110.9W	2.3

Table 3.1: Various ground-based IACT experiments around the world (circa 1999), combined with geographical location and altitude.

3.2.1 Detection of Cherenkov radiation above the NSB

The major limiting factor upon the detection of Cherenkov photons from EAS results from fluctuations in the Night Sky Background (NSB) flux ($S_{NS} \approx 10^{12}$ photons/m^2/s/sr). As Poissonian statistics govern the level of fluctuations in the night sky background, variations are on the scale of $\sigma_{NS} = \sqrt{S_{NS}}$, and as Cherenkov photons from EAS comprise ~10^{-4} of the total NSB fluctuations are often at a level well above the Cherenkov photon flux levels from EAS. An expression for the minimum detectable Cherenkov photon signal S_{min}, within a background of NSB photons can be derived from simple considerations. The Cherenkov signal S_C, detected at the

prime focus of a simple telescope system is related to the characteristics of the detector,

$$S_C \propto \eta A_m ,$$

where A_m is the mirror area and η is the combination of the relative quantum efficiency of the detector and mirror reflectivity ($0 \leq \eta \leq 1$). The contribution to the full signal received due to NSB photons will be time-dependent and similarly dependent on the characteristics of the detector,

$$S_{NS} \propto \Omega \eta A_m t \Phi ,$$

where Ω is the solid angle of sky subtended by the detector (i.e. the field of view of a single detector pixel), Φ is the photon flux due to the NSB, and t is the time over which the signal is integrated. The minimum signal threshold is proportional to the ratio of the NSB fluctuations σ_{NS} and the Cherenkov signal S_C,

$$S_{min} \propto \frac{\sigma_{NS}}{S_C} \propto \sqrt{\left(\frac{\Omega t \Phi}{A_m \eta}\right)} .$$

To avoid recording NSB fluctuations, the Cherenkov light signal S_C, from an EAS must be several times greater than σ_{NS} to provide for a low minimum signal threshold.

3.2.2 Basic optimisation for detecting radiation from EAS

Cherenkov signals from EAS may be enhanced by using large highly reflective mirrors combined with the intelligent choice of photomultipliers. Choosing to use PMTs which have peak quantum efficiencies (η) within the blue to near UV region, i.e. where the spectrum of Cherenkov light is most intense. The sensitivity range of

photomultipliers effectively reduces Φ, as the spectral distribution of NSB photons is much flatter than the Cherenkov photon spectrum, thus decreasing the relative background signal.

Further reductions in sky noise can be achieved by reducing the time over which the Cherenkov photon signals are integrated to a minimum. The characteristic time-scale of a Cherenkov light pulse is about 5 to 20 ns, so an integration time of around 20 ns would capture most of the Cherenkov signal whilst reducing the number of NSB photons observed. Further improvements can be made by using smaller PMTs and so minimising the solid angle of acceptance Ω.

3.3 Specifications for an imaging atmospheric Cherenkov telescope

The detection of Cherenkov light from an EAS using the IACT method requires dark moon-less nights and some form of triggering logic such that only Cherenkov events and calibration data are recorded. The main qualities of an IACT telescope – the Effective Sensitive Area (ESA) which is governed by the Field Of View (FOV) and triggering logic, and the threshold energy which is dependent on the ESA and the source spectrum – are discussed in the next few sections.

3.3.1 Effective sensitive area

The ESA of a ground-based Cherenkov telescope derives from a combination of sensitive area and detection efficiency, and is the equivalent sensitive area for

gamma-rays of an imaginary telescope with 100% collection efficiency. The primary benefit which ground-based observation provides for the detection of VHE gamma-rays arises from the sensitive area of Cherenkov telescopes not being related to their physical size but to the lateral extent of the Cherenkov light pool (see section 2.3.3). For a VHE gamma-ray induced air shower falling vertically through the atmosphere, Cherenkov photons typically fall within a light pool of area $>10^5$ m^2, providing ground-based observations with sensitive areas out of all proportion to their physical dimensions. The detection efficiency of ground-based telescopes is principally dependent upon light collection area, mirror quality, detector quality and environmental concerns, such as ambient light levels and sky transparency, with a significant additional factor deriving from the implementation of image selection criteria designed to 'clean up' the data by preferentially selecting images of gamma-ray induced EAS from further analysis.

The ESA of ground-based telescopes is strongly dependent upon the zenith angle at which observations are made; as the zenith angle of observation increases, the size of the Lateral Distribution Function (LDF) (see section 2.2.3) also increases, for as the distance between shower maximum and the telescope becomes larger the Cherenkov light evolves and spreads over a wider area. By choosing to preferentially observe sources at high zenith angles the ESA of a ground-based telescope can be improved at high energies at the cost of a reduction in the detection efficiency of low energy EAS. The effect that zenith angle has on telescope ESA is shown graphically for a range of shower energies in Figure 3.2.

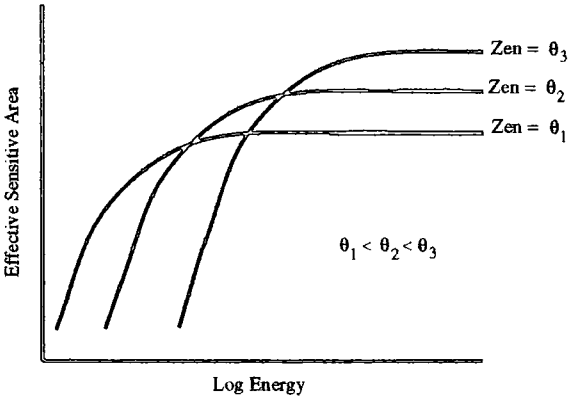

Figure 3.2: A diagram showing the way in which the effective area of a ground-based IACT telescope changes with zenith angle. Note that a greater effective area may be obtained at progressively higher zenith angles at the expense of a higher energy threshold.

For gamma-rays the extent of the LDF is not strongly dependent on the primary energy, so as the shower energy decreases so will the resultant Cherenkov photon flux, hence there will come a point where the efficiency of detection falls below 100%. As a result of changing ESA with zenith angle it has been suggested that observations of known VHE gamma-ray sources at high zenith angles would be an effective way of sampling their energy spectra in the tens of TeV range.

3.3.2 Field of view

The Field Of View (FOV) of an IACT telescope should be large enough to record images of showers with impact parameters up to the radius of the Cherenkov light pool of a gamma-ray induced EAS. If the FOV is too large the telescope will detect more background nucleon induced EAS, as these are isotropically distributed in the sky, but will not detect any more gamma-ray induced EAS. If the FOV is made too small then one will lose part of the images of potentially observable gamma-ray induced EAS.

For observations of gamma-ray induced EAS at a zenith angle of $\theta = 0^o$, the optimum FOV for an IACT telescope can be found by using a simple geometrical approximation,

$$\alpha = \tan^{-1}\left(\frac{2r}{h}\right) \approx \frac{2r}{h}, \quad [h \gg r]$$

where 'r' is the characteristic radius of a Cherenkov light pool and h is the approximate height of maximum of a gamma-ray induced EAS ~ 10km. This expression gives an optimum FOV of about 3^o, for a point source.

3.3.3 Triggering

In order to record the Cherenkov signal, the detector needs to be triggered in some way, which will reliably minimise the number of accidental triggers. A typical detector package consists of an array of individual photomultiplier tubes (or pixels) viewing neighbouring sections of the sky and working as a whole to produce an image.

As sky noise varies randomly from tube to tube, yet the Cherenkov light signature from EAS is both spatial and temporarily coincident over several tubes, the coincidence in the Cherenkov light signal over a number of tubes can be used as the basis for reliable trigger criteria for the detector's electronics. The triggering requirement of spatial and temporal coincidence in neighbouring PMTs allows each detector pixel in the imaging array to be triggered by a lower than expected signal threshold, while allowing the detector as a whole to maintain a low rate of accidental triggers. Any sensible triggering condition would demand that a number C of

neighbouring tubes, or tubes spatially coincident upon the sky (in the case of an IACT telescope with more than one paraxial detector), should receive a signal above a certain threshold level within a short coincidence time, Δt. The rate, R, at which this condition is satisfied by chance, for a telescope with N possible triggering permutations, satisfying a particular triggering logic, is given by,

$$R \approx N\left[C!\left(\prod_{i=C}^{i=1} n_i\right)\Delta t^{(C-1)}\right]$$

where n_i is the accidental count rate for an individual pixel.

3.3.4 Telescope energy threshold

The energy threshold of an IACT telescope depends on the telescope's ESA and on the intrinsic differential energy spectrum of VHE gamma-rays. The energy threshold of an IACT telescope is often defined as the energy at which the detected gamma-ray flux is at a maximum, i.e. the peak of the function created by multiplying the ESA as a function of energy with the intrinsic differential source spectrum.

Some form of gamma-ray event selection analysis will always be necessary to enable statistically significant detection of gamma-ray induced events, as gamma-ray fluxes are only ever a tiny fraction of the total cosmic-ray flux. Inevitably during this analysis, there will be a fraction of gamma-ray induced events which are not retained, and this selection efficiency is certain to be energy dependent. As lower energy events become progressively less well defined, they become less likely to be retained after analysis, inevitably increasing energy threshold through data selection.

3.4 The principles of data processing

The behaviour of an atmospheric Cherenkov telescope may deviate from the ideal due to, for example, small changes in detector gain, both during and in between observations. Variations of this kind may significantly affect the appearance of inherently similar light distributions, and this will significantly reduce the efficiency of any background rejection techniques.

Once the detector has been triggered, the individual signals from each photomultiplier tube are recorded by the detector electronics. These data then need to be calibrated to reduce variability in PMT performance between observations. There are a number of additional reasons for calibration, some due to the tracking ability and structural rigidity of the telescope while others are more concerned with the behaviour of PMTs in the detector package.

3.4.1 Source tracking and telescope rigidity

The changing gravitational stresses on telescope structures as they track astronomical sources around the sky will produce some deformation, and thus relative movement between where the telescope's drive motors register the telescope to be pointing and where in the sky the telescope is in actuality pointing. If this occurs in a reproducible way then a standard correction algorithm can be produced that may then be applied as an offset to the telescope pointing in real time, or later as a correction during data-pre-processing. If the telescope's structural integrity is such that the tracking changes in an unpredictable fashion, then regular measurements have to be made during each

observation of the actual pointing direction of the telescope. The monitoring of telescope pointing accuracy is usually accomplished by mounting a coaxial CCD camera such that it always points where the mirrors are pointing, whilst taking frequent measurements of the apparent position of some bright star of known coordinates.

In addition to accurately determining the telescope's pointing direction, there is the problem of relative movement of the mirrors and the detector package. A typical detector package will have a considerable mass and be placed at the prime focus of the telescope system, several metres in front of the mirrors on a set of booms. The bending moment induced will thus be considerable, though the effects on image position and apparent source position due to this this kind of deformation are much simpler to determine and occur in a predictable and reproducible way, making it very easy to compensate for.

3.4.2 Photomultiplier calibration

The low flux levels and short durations of Cherenkov flashes require the use of photomultipliers for their detection: the performance of PMTs under observational conditions is therefore of considerable importance. PMTs are designed and optimized for use in near total darkness, so exposing them to a bright night sky and running them at very high gains, as is common in VHE gamma-ray astronomy, is not an application for which PMTs were intended. It is therefore important to closely monitor PMT behaviour, to calibrate the signal received from each tube relative to the

flux of photons incident upon it. This reveals a major problem inherent in PMT usage: there is no reliable way to measure accurately their absolute gain, as a calibration source of known intensity would be required, and the absolute gain would need to be measured under strict conditions, i.e. collimated light in a restricted frequency range. Under the conditions which prevail during an observation, were the light incident on the PMTs is not collimated and not within a restricted frequency range, notwithstanding the complications introduced by the signal processing electronics. It is not possible under observational conditions to acquire accurate measurements of absolute PMT gain. In contrast to the absolute gains of the photomultiplier tubes the relative gains of the tubes are much easier to ascertain (see section 4.4.3). Estimates of PMT relative gains can be made by mimicking Cherenkov flashes using either a calibrated LED fixed to the the PMT window or laser induced scintillation flashes. In order to achieve this an attempt must be made to measure the relative gains of all the tubes directly before or during each night of observation.

3.4.3 Preliminary pre-processing

The most commonly used operational method for an IACT telescope involves conducting observations of a candidate gamma-ray source for a fixed period on-source and a nearby off-source location for a similar period, with the off-source data being used as a reference data set for the on-source observations. After calibration and image parameter selection, comparison is made between the gross numbers of events remaining in the on- and off-source data sets. For effective use to be made of the reference off-source data, care must be taken to ensure that any systematic bias

between the on- and off-source fields is reduced to a minimum. The main cause of systematic bias between the candidate source field and the nearby reference field is the small differences in the inherent brightness of each field. These induce differences in photomultiplier noise levels between fields, giving rise to systematic bias in the triggering efficiency and hence the energy threshold in the on- and off-source fields. These systematic differences in photomultiplier tube noise levels will also alter the apparent distribution of light in the images and so reduce the efficiency of any image parameter selection regime. If left untreated these systematic biases could reduce or completely mask a real gamma-ray signal, or worse still they have the potential to indicate the presence of a signal where none exists. The precise details of how systematic biases should be treated is telescope dependent, though the methods and techniques employed by the Durham VHE gamma-ray group will be discussed in section 4.6.3.

3.5 Summary of VHE observations

The first tentative detections of VHE gamma-ray emission from astronomical objects were made in the 1970s. Early detection methods relied on the identification of pulsed emission to identify a source, limiting the type of objects which could be observed. Observation concentrated principally on galactic objects which were considered to be possible accelerators of particles to cosmic-ray energies, such as pulsars and X-ray binaries (XRBs). The observations made during the 1970s gave only low significance and results were compounded by the expected transient nature of XRB emission, as a result it became very difficult to obtain independent source

confirmation. Through the 1980s and 1990s advances in ground-based gamma-ray astronomy, driven principally by the development and refinement of IACT telescopes, made it possible to detect constant fluxes of VHE gamma-rays. By the end of the 1980s the Crab Nebula had been identified as a constant source of VHE gamma-rays, quickly becoming the standard candle source for VHE astronomy. Since then the Crab Nebula has been extensively studied at VHE energies and found to be a remarkably steady source. The integral flux above 1TeV has been measured to be ~ $2.1 \pm 0.2_{stat} \pm 0.3_{sys}$ x 10^{-11} cm^{-2} s^{-1} and has remained constant to within the ±20% error margin of current detectors (Ong (1998)), it has been estimated that any pulsed component at the pulsar period of 33ms must be less than 4.8 x 10^{-12} cm^{-2} s^{-1} above 250GeV (Lessard et al (2000)).

3.5.1 Recent observations

A catalogue of VHE gamma-ray sources is shown in table 3.2: only sources which have been detected via the IACT with a significance of >5σ, and published in a refereed journal, have been included. Many of the sources detected by the first generation of Cherenkov telescopes have not been confirmed by IACT telescopes. XRBs are particularly notable by their absence as compared to earlier catalogues. Only Cen X-3 has been confirmed, though as yet not confirmed by another IACT telescope. This selection effect may have a number of causes, it is expected that XRBs are by nature highly transient VHE gamma-ray emitters and it may well be the case that their initial detection was merely fortuitous. Another factor which is certain to cause a significant selection effect is that since the first detection of an extra galactic VHE gamma-ray source Mrk 421 (Punch et al. (1992)) later observing

strategies focused almost exclusively on other extragalactic candidate sources (principally X-ray selected BL lacertae galaxies), due to the perceived better chance of successful observation.

Object Name	Object Type	First Detection	Confirmed (No. times)
Crab Nebula	Plerion	Weekes et al. (1989)	YES (8)
Vela Pulsar	Plerion	Yoshikoshi et al. (1997)	NO
Markarian 421	AGN	Punch et al. (1992)	YES (5)
Cas A	SNR	Puelhofer et al. (2000)	NO
SN1006	SNR	Tanimori et al. (1998)	NO
Markarian 501	AGN	Quinn et al. (1996)	YES (6)
PSR B1706-44	Plerion	Kifune et al. (1995)	YES (1)
PKS 2155-304	AGN	Chadwick et al. (1999b&c)	NO
1ES 2344+514	AGN	Cantanese et al. (1998)	NO
BL-Lac	AGN	Neshpor et al. (2001)	NO
1ES 1959+650	AGN	Nishiyama et al. (1999)	NO
3C 66A	AGN	Neshpor et al. (1998)	NO
RXJ 1713.7-3946	AGN	Muraishi et al. (2000)	NO
1H1426+428	AGN	Horan et al. (2002)	NO

Table 3.2: A catalogue of claimed and confirmed VHE gamma-ray emitting objects, detected at the >5σ level.

Most of the next generation of IACT telescopes will be of the stereo variety, proposals exist for observatories in the northern (VERITAS) and southern hemisphere (HESS) and CANGAROO III. These are planned to be large arrays of several telescopes (7, 16 and 4 respectively), The HESS project is currently (late 2001) in phase-one of operation which involves the construction of 4 telescopes. These projects will enable both surveying of the galactic plane for transient VHE gamma-ray sources and highly sensitive long-duration dedicated observations of particularly interesting objects.

3.6 Summary of IACT telescopes

The longest established group using IACT telescopes is the Whipple collaboration of American, British and Irish universities who were the pioneers of IACT in the 1980s, and have led the field in the northern hemisphere since the late 1960s. The optical reflector of their telescope has been used for Cherenkov astronomy since 1968, and has a reflective area of ~ $75m^2$. Though its camera has changed considerably over the decades, their initial camera configuration was a hexagonal array of 37 one inch 0.5° PMTs, with a 3.5° FOV. The most recent configuration was implemented in the summer of 1999 and consists of 379 x ½inch, 0.13° resolution PMTs, with a guard ring around the outside of 111 x 2inch 0.46° resolution PMTs, arranged in an hexagonal array so that the total FOV of this new camera is about 4.8°. Another northern hemisphere group is the French CAT collaboration. Their telescope, based at Themis, in the French Pyrenees, has a total reflective area of $18m^2$ and the highest resolution camera currently in operation.

Experiment	Mirrors		Detectors			Threshold
	Area (m^2)	PSF (°)	#PMTs	Resolution (°)	FOV (°)	(GeV)
CANGAROO II	75	0.2	512	0.17	3.0	200
CAT	18	0.1	546	0.125	4.8	250
Durham Mk6	3x42	0.18	91	0.25	3.5	300
Whipple	75	0.15	379	0.23	4.0	250
HEGRA	5x8.5	--	271	0.25	~1*	700

Table 3.3 The principal specifications of the four major IACT telescopes. Only the number and resolution of the smallest PMTs has been shown. The FOV is that of the entire camera including the guard ring PMTs. Additional details of the Mk6 PSF and threshold are provided in chapter 4.
* value in stradians.

There are also two groups which have been operating IACT telescopes in the southern hemisphere, both located in Australia: the recently completed CANGAROO II telescope and the recently decommissioned Durham Mk6 telescope. The CANGAROO II telescope's camera package consists of a square array of 552 x ½inch PMTs, combined with a large mirror surface area.

The pionears of the stereo technique the HEGRA IACT system, another northern hemisphere instrument, is part of the HEGRA experiment which consists of a number of different types of particle detectors, located on the Canary island of La Palma. The IACT system consists of 5 identical telescopes arranged on the corners of a square with 100 m sides, with a telescope in the center of the square. This system produces Stereoscopic observations based on a telescope coincidence trigger, allowing unambiguous reconstruction of the air showers in space and leading to the angular reconstruction of primary particles on an event-by-event basis.

The Durham Mk6 telescope has one of the lowest resolution cameras of all five telescopes, but this is not as serious a handicap as at first may be suspected. The unique three mirror design allows for a three-fold spatial coincidence trigger, allowing the PMTs in the central camera to be run with a very high gain while simultaneously keeping the rate of accidental triggers to a minimum. The Durham Mk6 telescope is considered in greater detail in the next chapter.

	Telescope	Camera
CANGAROO II		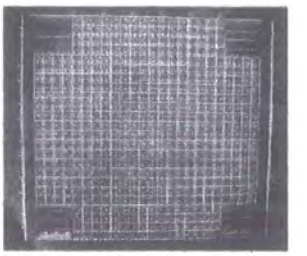
CAT	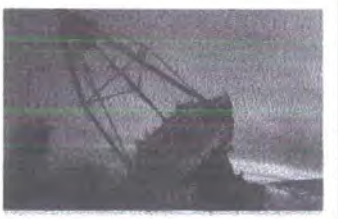	
Durham Mk6		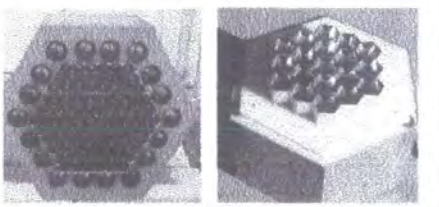
Whipple		
Hegra	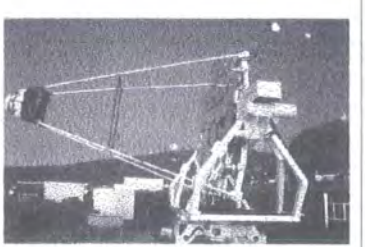	

Table 3.4: The four main IACT telescopes and their respective cameras. Shown here for comparison.

CHAPTER FOUR - The Durham Telescopes

4.1 Introduction

The Durham VHE gamma-ray astronomy group has until recently (late 1999), been operating imaging atmospheric Cherenkov telescopes (IACTs) at Bohena (near Narrabri) in New South Wales, Australia. In this chapter the operation of, and observations made with, the recently de-commissioned Mark 6 (Mk6) telescope will be introduced.

VHE gamma-ray observations by the Durham group began in Dugway, Utah, USA in 1981. The group relocated to Narrabri in 1986 so that observations of the southern sky could be made. The results of the VHE gamma-ray observations made in Dugway suggested that X-ray binary systems were potentially interesting VHE gamma-ray sources, a large number of which are observable from the southern hemisphere. In addition a number of other sources of interest, including the Galactic centre, the Large and Small Magellanic Clouds and Centaurus A, which was identified as a TeV source in the early days of VHE gamma-ray astronomy (Grindlay et al. (1975)), although not confirmed, would be observable.

As the field of VHE gamma-ray astronomy developed after 1986, further extragalactic sources, i.e. X-ray selected BL Lac Galaxies, were observed by the EGRET satellite experiment to be hard X-ray sources, and one in particular was seen to undergo strong flaring activity at VHE energies (Punch et al. (1992)). Coupled

with an early failure to detect and confirm X-ray binaries as VHE sources, later work focused more intensively upon extragalactic objects.

4.1.1 The Bohena observatory

The Bohena Observatory is located approximately 20 km southwest of Narrabri, New South Wales, Australia. It is at a latitude suitable for observing most southern hemisphere galactic objects (30.5S, 149.8E) and, at the time of selection, had experienced many years of clear and stable weather conditions. The Bohena site was, until 1978, the location of SUGAR, the Sydney University Giant Air-shower Recorder. Figure 4.1 shows a plan of the Bohena Observatory site. In addition table 4.1 shows the periods over which each of the Durham telescopes were in operation, and the years in which significant upgrades where made.

The low altitude of the Bohena site (260m ASL) results in an increase in the energy threshold of the Durham telescopes, as compared to that of an identical instrument operating at higher altitudes. The development of the Durham telescopes has been driven by the need to operate at maximal sensitivity, so as to reduce the telescope's energy threshold. As a result of this, all of the Durham telescopes have been constructed around a triple-dish design. Each telescope consists of three light-collecting dishes and detector packages on a single mount, aligned so that they are simultaneously exposed to the same patch of sky.

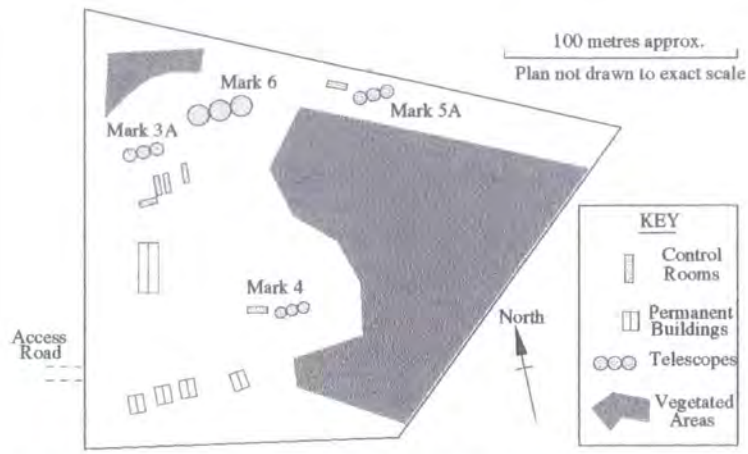

Figure 4.1: A plan of the Durham group's observatory at Bohena Creek near Narrabri N.S.W. Australia (*circa* 1997)

Telescope	Operational	Upgraded
Mk3/3A	1986 - 1996	1994 Mirrors and Detector
Mk4	1990 - 1993	N/A
Mk5/5A	1992 - 1998	1994 Detector
Mk6	1995 - 1999	N/A

Table 4.1: Operational periods of the Durham instruments located at Bohena creek.

The three detectors form part of the triggering mechanism, with the central high-resolution detector recording the Cherenkov images. The immediate precursor to the Mk6 telescope, the Mk5A, was a medium-resolution imaging telescope and offered a significant improvement in sensitivity and threshold over previous Durham instruments. The operation of the Mk5 telescope provided the Durham group with valuable experience in imaging techniques, event parameterisation and, consequently, rejection criteria for the nucleon induced background event images. A detailed discussion of the performance of the Mk5A telescope may be found in Dickinson (1995).

4.2 The Mark 6 telescope

The Mk6 was the largest and most advanced of the Durham group's telescopes, constructed between April 1993 and May 1994 in England, then shipped and reassembled on site in late 1994. The design of the Mk6 telescope focused on providing for a low energy threshold instrument, with the construction relying heavily on the lessons learned during the construction of the Mk5 telescope, particularly with regards to mirror manufacture. The aim of reducing the energy threshold was pursued along five independent lines:

- The use of very large mirrors, compared to previous Durham instruments.
- The intelligent choice of PMTs, to match their spectral and temporal response to that of the Cherenkov light flash.
- The use of a stable, high bandwidth data handling system.
- The use of a high resolution detector package to provide sufficient imaging information for effective event selection to be made.
- The continued use of the three-fold spatial coincidence technique so that the PMTs may be run at maximal gain and sensitivity, without excessive false triggering.

The means by which these targets were attained will be discussed in the following sub-sections of this chapter.

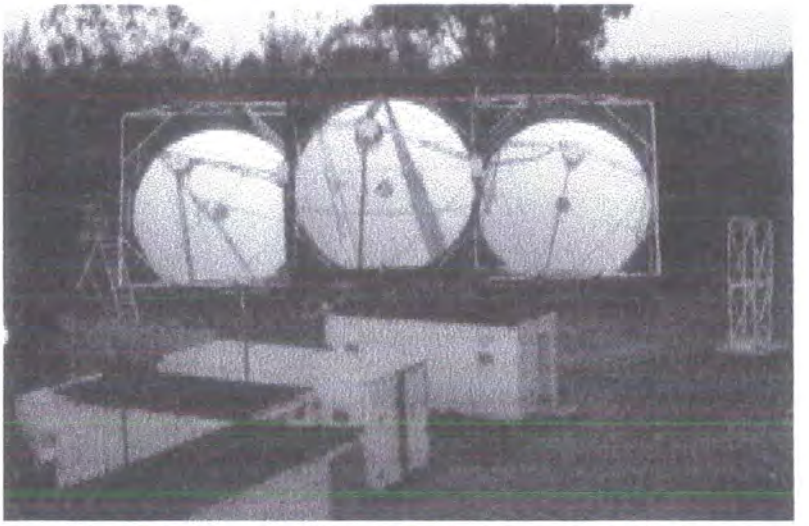

Figure 4.1: Picture of the Mk6 telescope at Bohena Creek observatory. In the foreground are a number of shipping containers, housing the telescope electronics, control room, workshop and monitoring annex.

4.2.1 Mirrors

The three mirrors of the Mk6 telescope were all 7.2m in diameter; each one consisted of 24 sectors, of width 96cm at the mirror edge. The optical properties of the mirror surface were chosen to match as closely as possible the spectrum of Cherenkov light received at ground level. Atmospheric absorption and PMT spectral response induce the requirement that the mirror surface should reflect efficiently within the 300 - 600nm optical window and practical concerns required that the surface should also be optically stable over a time scale of years. The Mk6 mirror surface was chosen to be made from anodised aluminium (Alanod™ 410G3, Veredlung GmbH & Co). The specular reflectivity of this material is >75% over the wavelength range 350 - 720 nm, with 10 ± 2% diffuse reflection (Weekes (private communication)) and had also been shown to be optically stable over a nine year period in the prevailing conditions at the Bohena observatory site.

Each surface segment was mounted on a light-weight aluminium honeycomb material (Ciba-Geigy, Airoweb 3003). this structure was then backed and sided with an aluminium *'Dural'* sheet; a diagram of the mirror construction is shown in figure 4.2. The parabolic cross-section adopted for the mirror gave an isochronous photon distribution at the expense of some off-axis image aberrations, though these were calculated to be smaller than the point spread function of the MK6's mirrors out to 1.5° off axis.

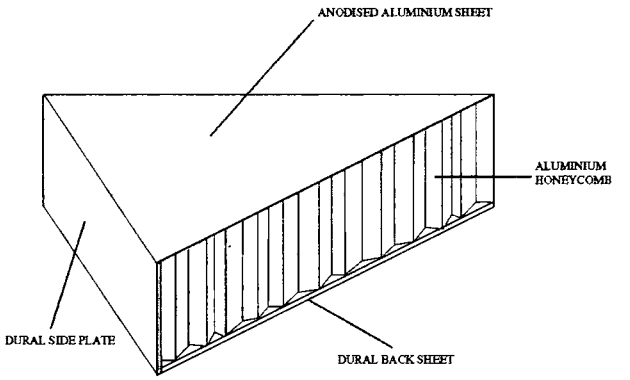

Figure 4.2: Schematic cross-section of a Durham telescope mirror segment.

Construction constraints required a compact telescope design. With the compromise between steering and the effects of off-axis aberrations becoming optimal for a focal ratio of f1.0. This focal ratio gave an image scale on the focal plane of ~0.008° mm^{-1}. Considering the angular extent of a typical EAS image as seen from the ground (of the order of degrees), and the central camera pixel size (21mm ≅ 0.17°) and separation (center-to-center distance of ~30mm ≅ 0.24°), this configuration produced an image size which allowed for adequate sampling of the angular Cherenkov light distribution.

4.2.2 Detector packages

The principal feature of the Mk6 telescope, and previous Durham instruments was the three mirror design format. This optical arrangement required three separate detector packages, one at each of the three prime foci. The central detector consisted of 91 hexagonal-spaced, Hamamatsu R1924 PMTs. The photocathode diameter of each PMT (21mm), results in ¾ coverage of the total detector imaging area. The remaining ¼ *'dead area'* between the photocathodes was minimised by the use of light collecting cones, these directed additional light onto the photo sensitive area of the PMTs (Roberts (1998)).

The Hamamatsu R1924 PMTs were chosen for use in the central imaging camera principally for their low pulse rise time (~2ns), transit time (~8ns) and a transit time spread of ~1 ns (at 1000 Volts). The cathode material (Bialkali, Cs & Na) of this PMT type is sensitive to light between 300 and 650 nm, with peak cathode radiant sensitivity at 420 ± 50 nm, corresponding well to the spectral distribution of Cherenkov light at ground level.

The central detector package also included a guard ring of 18 x 55mm diameter Burle 8575 PMTs, equally spaced around the hexagonal perimeter of the 91 imaging tubes. The guard ring PMTs enabled a rough estimation of the Cherenkov light distribution outside the imaging area of the detector package, to improve the sampling capability of the detector. The detector packages located at the prime foci of the left and right mirrors had a much lower resolution than the central imaging detector, at about 0.5°.

They were principally used as part of the trigger but also supply some useful image information (Shaw (1999)).

4.2.3 Triggering

The fields of view of the central, left & right detector packages were arranged such that a group of seven central detector PMTs overlap, with one hexagonal PMT in each of the left and right detectors (see fig 4.3). The four-fold coincidence (a single temporal and a three-fold spatial) trigger logic required that both corresponding left and right PMTs, and any adjacent two out of seven of the corresponding central camera PMTs, received a signal which passed a discrimination level (usually set to be ~50mV) within a short ~10ns time window. The typical trigger rate for the Mk6 telescope was around 750 counts per minute near the zenith and under clear sky conditions; though the rate had been steadily decreasing over several years of operation, which was thourght to be due to a reduction in sensitivity of the PMT photocathodes.

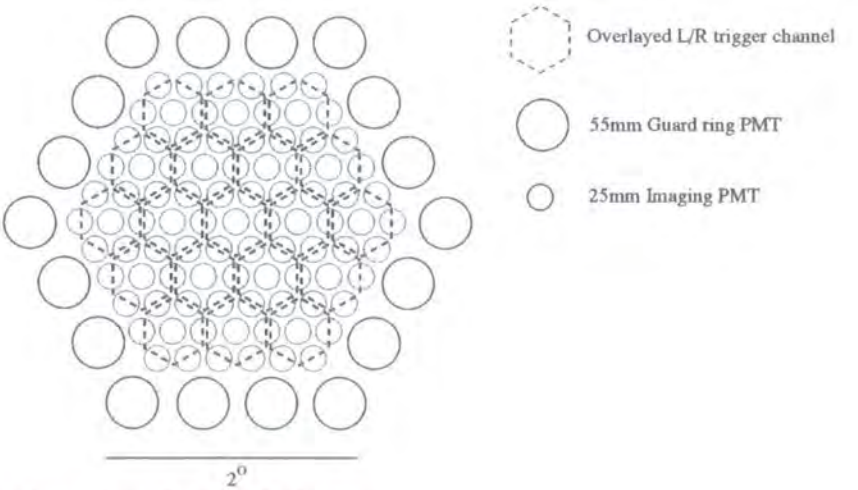

Figure 4.3: The trigger channels of Mk6 telescope.

4.2.4 Electronics

The data logging electronics for the Mk6 telescope are depicted schematically in figure 4.4. This system was developed using the experience gained from the previous Durham telescopes (Brazier et.al., 1998).

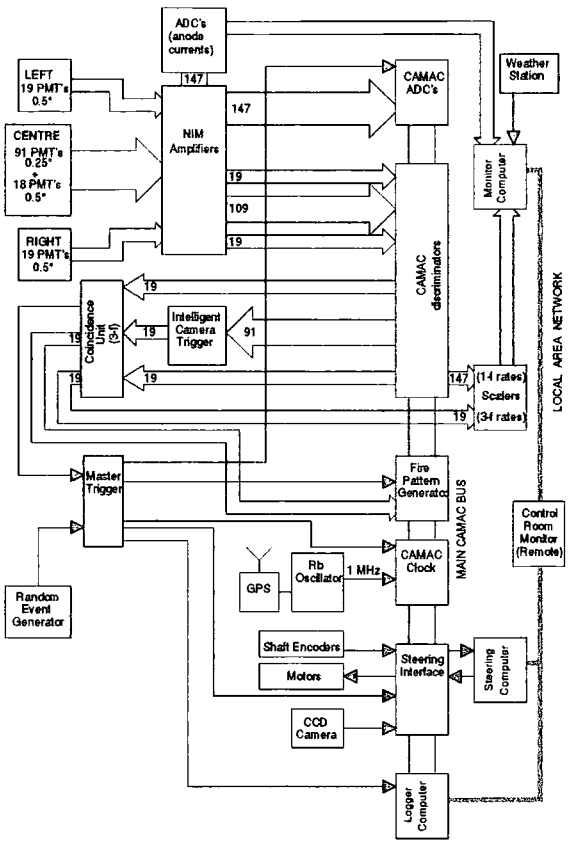

Figure 4.4: The schematic layout of the Mk6 telescope electronics system. When an event is observed by the telescope detectors (upper left) the signal from each PMT is first amplified and sent to the discriminator. The signals from those tubes which successfully meet the discrimination level (set in units of millivolts) then pass to the coincidence unit (via the camera trigger unit, in the case for the central camera PMTs). If the coincidence criteria are met, then the master trigger unit informs the logging computer to read all of the information available across the main CAMAC bus link, i.e. the CAMAC analogue to digital converter (ADC) output, which supplies a digital value for the signal in each PMT; the CAMAC discriminator, which supplies information about which tubes rose above threshold; the fire pattern generator, which gives information about which trigger channels fired; the CAMAC clock, which supplies a sub-microsecond accurate date stamp; and finally the steering interface; which supplies information concerning the direction in which the telescope is pointing at the time of the event.

4.2.5 Data collection and integrity

It is necessary to obtain both on- and off-source observations due to the variable nature of the atmosphere, which can cause significant variation in the images of EAS event images over short time-scales. Observations with the Mk6 telescope were taken in 15min segments towards and away from the source position; several modes of observation were used: on/off/on/off, off/on/on/off and their inverse. In the case of the Mk6 telescope it has not in the past been possible to calculate or predict the number and the image parameter distributions of background events that are in the on-source data set. Thus a comparison off-source observation is made either immediately before or after an on-source observation to empirically measure the background. Interspersed in the observational data are two types of embedded false coincidence data; referred to as *random* and *laser* events.

Random events are the result of triggering the telescope detectors electronically at random intervals to gain a measure of the background signal received by the detector. These data are used to derive pedestal values for each PMT, to be removed from the absolute PMT values in any given real event to take account for the ubiquitous night sky background. Laser events were obtained by illuminating each of the three detector packages with a simultaneous diffuse pulse of laser induced scintillation light. This enables a relative gain calibration to be made, as each PMT will receive similar illumination, the relative responses of the photomultiplier tubes to the scintillation pulse may then be directly related to their relative gains.

During observations, which were routinely made on clear moonless nights, a variety of '*house keeping*' data would be recorded for future reference in case questions arose post-observation as to the integrity of the data (i.e. ambient air and mirror temperatures, humidity and wind speed).

4.2.6 Data reduction

Several stages of calibration are necessary to format the data for final analysis. Firstly the data are split into 15 minute long on- and off-source segments, and the embedded false coincidences are extracted to obtained a measure of the pedestal and relative PMT gains.

The responses of the imaging PMTs to random and laser events (measured in digital counts) are used to correct for gross differences in the relative responses of the PMTs to to both background and Cherenkov light. Additional Gaussian noise is introduced into the data to equalize the responses of differing PMTs in a process known as '*software padding*' (Cawley et al. (1993)). This provides a true representation of the Cherenkov light distribution on the detectors focal plane, free from the effects of differing on/off field brightness and differences in the sensitivity of the PMTs. Modifications are also made to the data to accurately locate the source position in the central detector's field of view for each event, using pointing information obtained from a co-axial CCD camera mounted near the middle of the central mirror. The resultant calibrated EAS images still require some form of parameterisation to allow rejection criteria to be applied.

4.3 Cherenkov image analysis

To identify a gamma-ray signal, those images which are viewed as unlikely to be produced by gamma-ray initiated EAS are rejected from both the on-source and off-source data sets. Following this a comparison is made of the number and orientation of the remaining images, with a significant excess of events in the on-source data set being indicative of a detection. As was discussed in section 2.3.6, the different ways in which gamma-ray and nucleon induced EAS develop within the atmosphere result in significant differences in their light distributions, as seen from the ground by an imaging system. In order to utilise these differences in some kind of background suppression analysis it is first necessary to parameterise the images in a way which will emphasize these differences and produce a small number of highly selective parameters. The method chosen for analysing the data obtained by the Mk6 telescope is the '*image moments technique*'.

The detector PMTs are viewed as potential image elements depending upon the relative Cherenkov signal observed by each one. After a selection of PMTs (image elements) has been made, the moments may be derived. The image moment based analysis technique requires certain approximations to be made in the calculation of the image parameters. It is necessary to define, in some way, which PMT signals are to be included in the calculations, requiring some arbitrary decision to be made about the extent of the image, although these decisions may be guided by optimising the selection using observations (Punch et al. (1991) & Reynolds et al. (1993)).

4.3.1 Image element selection

To apply moment analysis to the distribution of Cherenkov light within the Mk6 telescope detector, one first identifies which PMTs contain signals dominated by Cherenkov light rather than background noise. Each tube has a pedestal value and an *rms*-noise value which are both derived from the random triggers made during each observing period. The pedestal value of each tube is subtracted from the image data so that the remaining signal will consist of the Cherenkov signal combined with a residual *rms* noise value due to Poissonian variability in the background signal. A threshold level for the inclusion of a PMT's signals as an image element may be set in units of the background *rms* noise. PMTs which pass this primary criteria are known a 'image' pixels. Additional Cherenkov signal can be identified by defining 'border' pixels, which pass a less stringent selection threshold, though they must be adjacent to an image pixel.

Image and border pixel thresholds of 4.25 and 2.25 times the *rms*-noise level were optimised using the Whipple Crab Nebula 1988-89 database (Reynolds et al. (1993)) and were adopted by the Durham group with some additional conditions. In the selection technique chosen for use with the Mk6 data the image and border pixels must not only pass a sigma-based selection threshold, they must also pass a percentage-based selection threshold. Image pixels must be $>4.25\sigma$ of their *rms*-noise and >37.5% of the brightest pixel; border pixels must be $>2.25\sigma$ of their *rms*-noise, >17.5% of the brightest pixel and adjacent to a image pixel (Armstrong et al. (1999)). The additional criteria used by the Durham group allow for a certain degree of auto-

scaling in the image parameters derived for the brightest and largest images. The reason for this is to allow the larger and increasingly less common events to be binned together enabling a single set of parameter cuts to be applied. Once selected, the image and border pixels are given a weighting of one and used to derive the image moments (see section 4.3.2). The PMTs whose signal did not satisfy the threshold criteria for image and border pixels are given a weighting of zero and take no part in the analysis of image moments.

4.3.2 The moments technique

Moment analysis is a method for the estimation of a shape which involves the calculation of moments from a collection of elements. In two dimensional moment analysis it is assumed that a body *I*, consists of *i* elements of density $\rho_i = \varepsilon_i \mu_i$, where ε_i is the measured signal in element *i*, and $1 \leq \mu_i \geq 0$ is a weighting factor relating a degree of confidence to the measured signal located at coordinates (x_i, y_i). Some fundamental parameters may be derived to describe the distribution of density across the body *I*.

$$\Omega = \sum_i \rho_i$$

$$< x > = \frac{\sum_i \rho_i x_i}{\Omega} \qquad < x^2 > = \frac{\sum_i \rho_i x_i^2}{\Omega}$$

$$< y > = \frac{\sum_i \rho_i y_i}{\Omega} \qquad < y^2 > = \frac{\sum_i \rho_i y_i^2}{\Omega}$$

$$< xy > = < yx > = \frac{\sum_i \rho_i x_i y_i}{\Omega}$$

the variances in x, y and a cross term may then be derived,

$$\sigma_{x^2} = < x^2 > - < x >^2$$

$$\sigma_{y^2} = < y^2 > - < y >^2$$

$$\sigma_{xy} = < xy > - < x >< y > .$$

The point (< x >, < y >) is known as the 'centroid' of the density distribution. If we were discussing a solid body, then this point would describe the center of mass; the appropriate variances would indicate the extent over which this mass was distributed. These zeroth, 1st and 2nd order moments (M_r, r = 0, 1, 2) are all that is required to define an ellipse which best represents the distribution of density. It is possible for higher order moments to give further, more abstract information which could be used to provide better gamma-ray/nucleon induced shower image discrimination, though as the moment order increases the uncertainties due to measurement errors quickly escalate. If the elements j_i, ρ_i has measurement errors δj_i, $\delta\rho_i$ then the uncertainty in the moments derived ($\Delta M_r(j, \rho)$) is given by,

$$\Delta M_r = r!\ \Delta M_1$$

where ΔM_1 is the error on a 1st order moment derived from elements j_i, ρ_i,

$$\Delta M_1 \approx \frac{\sqrt{\sum_i \delta\rho_i \delta j_i^2}}{\Omega} .$$

The 0.25° pixel resolution over the 3.5° FOV of the Mk6 telescope's central imaging camera allows for accurate derivation of 2nd order moments. The light distributions due to Cherenkov events do contain higher order components, and some work has been conducted by the Whipple and CAT groups which takes advantage of the 3rd order moment *Asymmetry* (Weekes et al. (1997), Le Bohec et al. (1998)). This is a

measure of how the Cherenkov light in an image is distributed about the image centroid along the major axis. *Asymmetry* is extremely prone to both noise and the method of choosing which tubes are included as image elements, so it has never been utilised as a selection parameter for the Mk6 telescope data. Despite these significant problems the Whipple group were able to make some limited use of this parameter.

4.3.3 Image parameterisation

The development of the techniques used for the parameterisation of Cherenkov images have largely been due to the work of Hillas (1985), although the idea of differentiating between gamma-ray and nucleon induced showers via their images was initially proposed by Jelley & Porter (1963). The Hillas parameters used to best represent the shape of a Cherenkov event, as viewed by an IACT, are based on combinations of 1st and 2nd order moments derived from the light distribution within the image. Some commonly occurring terms are abbreviated below,

$$\Delta = \sigma_{y^2} - \sigma_{x^2}$$

$$z = \sqrt{\Delta^2 + 4(\sigma_{xy})^2}$$

$$u = [\, 1 + \frac{\Delta}{z} \,]$$

$$v = 2 - u$$

The main Hillas (image) parameters used in the analysis of Mk6 data are defined as,

$$< \text{Distance} >^2 = < x >^2 + < y >^2$$

$$< \text{Length} >^2 = \frac{\sigma_{x^2} + \sigma_{y^2} + z}{2}$$

$$< \text{Width} >^2 = \frac{\sigma_{x^2} + \sigma_{y^2} - z}{2}$$

$$< \text{Azwidth} >^2 = \frac{< x >^2 < y^2 > - 2(< x >< y >< xy >) + < x^2 >< y >^2}{< \text{Distance} >^2}$$

$$< \text{Miss} >^2 = \frac{1}{2}\left(u\langle x\rangle^2 + v\langle y\rangle^2 \right) - \left(\frac{2\sigma_{xy}\langle x\rangle\langle y\rangle}{z} \right)$$

$$\text{Alpha} = \arcsin\left(\frac{\text{Miss}}{\text{Distance}}\right).$$

The schematic in figure 4.5 shows what these parameters represent in terms of image shape and orientation of the image. Figure 4.6 shows a real event observed by the Mk6 telescope and in the lower left hand corner of this figure are a list of the derived image parameters in units of degrees. It should be clear from figure 4.6 that the ellipse derived from the moments of the image elements is not a fit to the data but is instead an alternative representation of the data which encapsulates the main features.

In addition to the Hillas parameters there are a number of other parameters used by the Durham group which help to distinguish between gamma-ray and cosmic ray EAS images. These additional parameters are *Iratio* which is a measure of the concentration of the Cherenkov light within the central camera, *Eccentricity* which is a measure of image elongation and *left right distance* or *Ddist* which is a measure of the displacement of the image centroid in the left hand detector as compared to the image centroid in the right hand detector.

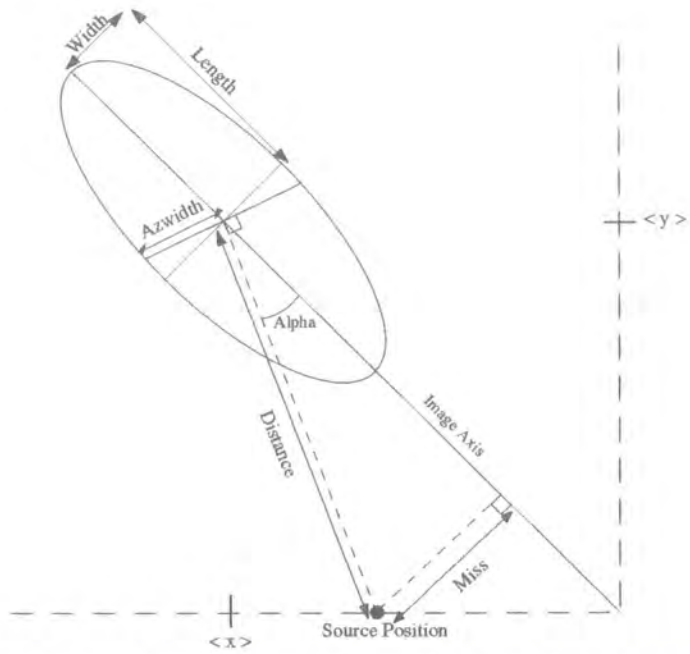

Figure 4.5: A schematic showing the relevance of each of the main image parameters used in the analysis of Cherenkov shower images.

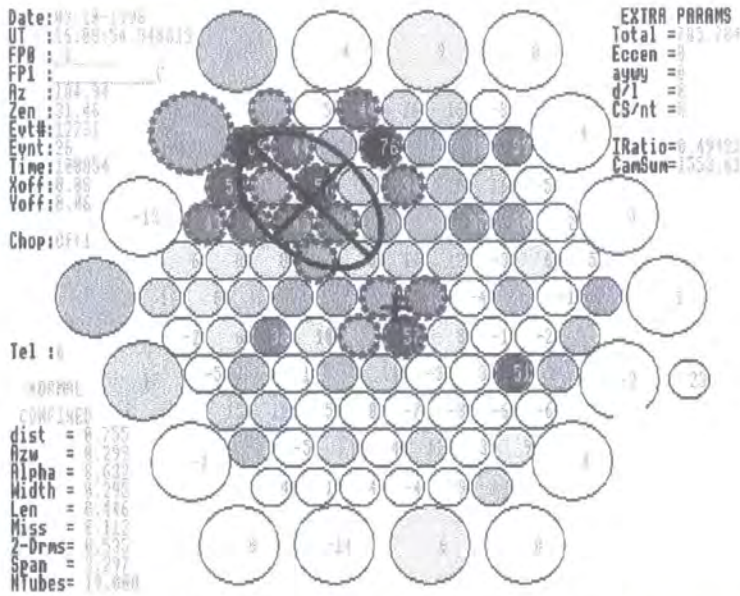

Figure 4.6: The image of an EAS as observed by the Mk6 telescope. The detector pixels (PMTs) which have been selected as elements to contribute to the image parameters are highlighted with dotted edges. The ellipse shown overlaying these tubes is constructed from the zeroth, 1st & 2nd order moments and variances of the selected tubes, combined using the Hillas parameter equations.

$$\text{Iratio} = 1 - \frac{\sum \text{signals within PMTs selected to derive Hillas parameters}}{\sum \text{signals within all central camera PMTs}}$$

$$\text{Eccentricity} = 1 - \frac{\text{Width}}{\text{Length}}$$

$$< \text{Ddist} >^2 = [< x >_L - < x >_R]^2 + [< y >_L - < y >_R]^2 \quad .$$

For a total given Cherenkov signal within the central camera, nucleon induced EAS produce more diffuse images than gamma-ray induced EAS. This is due to the inherently wider lateral development of nucleon induced EAS and leads to the selection of fewer image tubes and thus a lower selected signal for the purposes of image parameterisation. The result being that for nucleonic induced EAS the concentration ratio *Iratio* will be higher than for gamma-ray induced EAS. The left and right detector based parameters used by the Durham group have been described in detail elsewhere (Shaw (1999)).

4.3.4 Physical interpretation of image parameters

As the schematic in figure 4.7 shows, the type of image formed by a vertically developing EAS depends critically upon the lateral distance between the shower core and the telescope. Rieke (1969) studied the angular characteristics of Cherenkov light for various distances of the detector from the shower core. In the case where the core distance or impact parameter is zero, the shower images had a circular symmetry. As the value of the impact parameter increased the images became elongated into ellipses whose major axes were aligned towards, and whose centroids were displaced progressively further from, the center of the field of view. Eventually the core

distance becomes large enough for most of the Cherenkov photons from the EAS to fall outside the detector's FOV and the image is no longer sufficiently well sampled. The *width* parameter can be viewed as a measure of lateral development in the EAS. The *length* can be similarly viewed as a measure of the longitudinal development, though in this case the perspective effect of the shower axis/telescope axis lateral distance is also a significant factor. The differing physical processes governing the development of gamma-ray and nucleon induced EAS introduce differences in the Cherenkov light distribution (see section 2.3.6). This will in turn produce significant differences in the images formed, and the parameters derived to represent them.

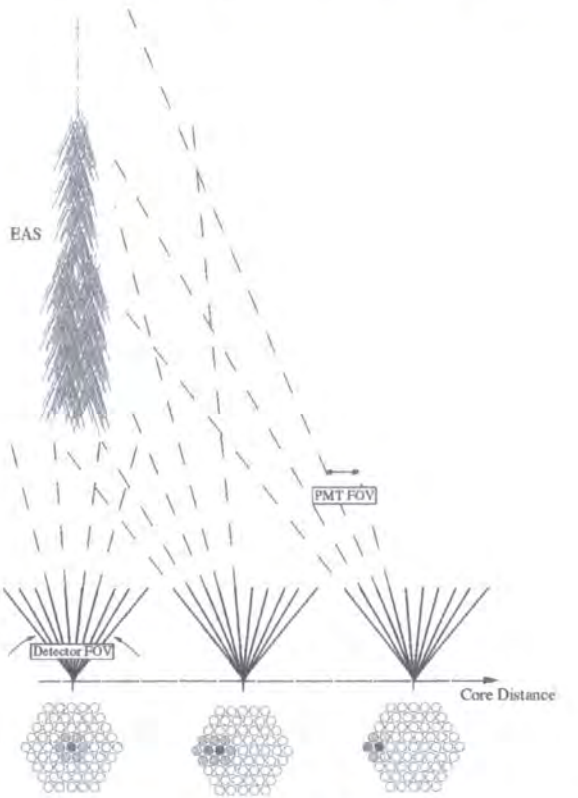

Figure 4.7: Schematic representation of the formation of Cherenkov images in a pixellated detector. As the core distance increases the image centroid moves out away from the camera center and the image first becomes elongated and then truncated. The density of shading indicates a relative increase in Cherenkov light signal.

4.3.5 Physical differences reflected in the Hillas parameters

The most striking and important difference between gamma-ray and nucleon induced showers is related to their apparent orientation, reflected in the Hillas parameter *alpha*. To all intents and purposes astronomical sources which are known to emit VHE gamma-rays may be considered to be point sources (this is strongly related to the current methods of observation, as the atmospheric Cherenkov technique is itself strongly biased to the detection of point sources of gamma-rays). VHE gamma-rays, originating from some given point, enter the atmosphere on parallel courses, thus the gamma-ray induced shower images appear to radiate away from the source position as they are viewed entering the atmosphere with different impact parameters.

In contrast to this, nucleons enter the atmosphere at random angles, due to their isotropic nature; thus nucleon induced showers appear to have no preferred orientation. A selection in Hillas parameter space which retains those events which have an orientation which is consistent with a Hillas parameter value of *alpha* less than about ~20° for the Mk6 telescope (this value varies depending on a specific detector's ability to resolve shower orientation) will preferentially select gamma-ray induced showers over those induced by nucleons.

The Hillas parameter *width* is also known to effectively distinguish between gamma-ray and nucleon induced showers. The *width* parameter retains some information concerning the lateral extent of the Cherenkov light producing region within the shower which produced the original image. The region in which most Cherenkov

light production is generated within gamma-ray induced showers (as mentioned in section 2.3.3) tends not only to retain the original track of the initiating particle, but also tends not to widen by more than a few tens of metres, thus resulting in relatively smaller values for *width* than parametric images of nucleon induced showers.

The Hillas parameters (or combinations of these) such as *distance*, *eccentricity*, and *length* are used by the Durham group to remove regions of parameter space where the data is either poorly sampled or of no use in distinguishing between gamma-ray and nucleon induced showers, e.g. the centre and edge of the camera and events which appear circular. We have not explicitly used *azwidth* or *length* cuts in our usual analysis, though a *length* cut as a function of *width* is implied by a combination of *width* and *eccentricity* cuts.

4.3.5 Gamma/nucleon EAS image separation

The essential difficulty in identifying a gamma-ray source using a set of image parameters which quantify the images as points in an n-dimensional parameter space is choosing which volume in this parameter space gives the best *Quality factor* (QF), where a *Quality factor* is defined as,

$$QF = \frac{\text{Fraction of selected events retained in ON source data set}}{\sqrt{\text{Fraction of selected events retained in OFF source data set (background)}}}$$

In essence therefore, a selection routine which enables the rejection of significantly more off-source events than on-source events will be preferentially selecting those events in the on-source data which differ from the standard off-source population which also exists in the on-source data. In this way the small on-source population of

gamma-ray images will make a larger contribution to the resultant on minus off source significance by a factor QF. Thus, the effectiveness of any particular selection strategy may be quantified by the respective QFs obtained. Unless a strong source of VHE gamma-rays is observed with a particular telescope, it is difficult to select with certainty which volume of parameter space will best select gamma-ray events over background events and result in a sufficiently large value for the QF to produce a signal which will appear above the expected Poissonian noise. Even if a strong source can be identified, there is still the difficulty of ascertaining the efficiency of gamma-ray preferential selection for a particular telescope and selection strategy combination. It is thus necessary to rely on Monte-Carlo simulations to hone the gamma-ray selection routines and predict the telescope sensitivity. A shower simulation program and a telescope model which can accurately reproduce the images of real background events is thus vital. It is a reasonable assumption that if a particular shower simulation, telescope model and selection strategy combination can accurately reproduce the images of background events, a high degree of confidence can be assigned to the simulation of gamma-ray events. Selection strategies derived in this way from the simulation of gamma-ray/background data may then be applied to real data with a high expectation of similar results.

The selection method used by the Durham VHE gamma-ray group is relatively simplistic. The data are binned by total signal detected, then parameterisation of the images is performed and cuts are applied to the data in each Digital Count (DC) bin to determine which regions of parameter space will give the best QFs and help determine the presence of a gamma-ray signal.

Using observations of PKS 2155-304 (an x-ray selected BL lac object) a volume of parameter space has been optimised to contain a significant on-source over off-source excess; the excess is very likely to be the result of gamma-ray emission from this object (Chadwick et al. (1999b and 1999c)). The parameter cuts optimised using the PKS 2155-304 data sets from 1996 to 1998 are shown in table 4.2, arranged by parameter and digital count (DC) bin.

	Size Ranges (digital counts)				
	500 - 800	800 - 1200	1200 - 1500	1500 - 2000	2000 - 10000
Distance (deg)	0.35 - 0.85	0.35 - 0.85	0.35 - 0.85	0.35 - 0.85	0.35 - 0.85
Eccentricity	0.35 - 0.85	0.35 - 0.85	0.35 - 0.85	0.35 - 0.85	0.35 - 0.85
Width (deg)	< 0.10	< 0.14	< 0.19	< 0.32	< 0.32
Concentration	< 0.80	< 0.70	< 0.70	< 0.35	< 0.25
D_{dist} (deg)	< 0.18	< 0.18	< 0.12	< 0.12	< 0.10

Table 4.2: Parameter selection used for the 6.8σ detection of PKS 2155-304 (Chadwick et al. 1999b).

To help clarify our analysis in publication we have chosen to use the term concentration when referring to Iratio, see section 4.3.3 for our definition of Iratio.

4.3.6 Other strategies for analysis

Selection of image elements for moment calculation and eventual parameter derivation as described in sections 4.3.1 to 4.3.5 and shown in Table 4.2 (for the case of the Mk6 telescope's central detector), is not the only method which could be used for gamma-ray/nucleon induced EAS image discrimination. Other parametric methods exist which differ in the way that image elements are either chosen and/or weighted and in the way the images are parameterized and/or selected. For instance, the Whipple image element selection and image parameterisation (Reynolds et al.

1993), the extended super cuts method (Mohanty et al. 1998) and Kernel analysis based methods (Moriarty and Samuelson (2000)). Non-parametric methods have also been shown to efficiently select gamma-ray images using fractal and wavelet parameters and trained neural networks (Haungs et al. (1997)).

4.4 Detections and flux limits for extragalactic VHE sources

Over the four year operational period of the Mk6 telescope, the VHE gamma-ray fluxes for PSR 1706-44, PKS 2155-304 & Centaurus X-3 have been reported. In addition to this a detection of Mrk 501 has been reported, though at the time of publishing no flux level had been estimated as observations where taken at large zenith angles for which only limited simulation data was available. Flux limits for a further nine AGNs have also been reported (Chadwick et al. (1999d).

Object	Type	Significance of signal (sigma)	Estimated Threshold (GeV)	Flux (DC) ($x10^{-11}cm^{-2}s^{-1}$)	3σ Flux Limit (pulsed) ($x10^{-11}cm^{-2}s^{-1}$)	Reference
PSR 1706-44	Pulsar	5.9	300	$3.9\pm1.9_{syst}\pm0.7_{stat}$	0.2	[1]
PKS 2155-304	AGN	6.8	300	$4.2\pm2.0_{syst}\pm0.75_{stat}$	n/a	[2]
Centarus X-3	X-ray binary	4.7	400	$2.8\pm1.4_{syst}\pm0.6_{stat}$	1.4	[3]
Markarian 501	AGN	5.6	~15,000	unpublished	n/a	[4]

Table 4.3: Positively identified sources of VHE gamma-ray emission observed by the Mk6 telescope. DC fluxes are based on number of excess events in the 'on' source data after event selection. Duration of observations and the gamma-ray retention factor have been considered. Three sigma pulsed flux limits are limits for pulsations at the pulsar period. [1] Chadwick et al (1998b) [2] Chadwick et al (1999b&c) [3] Chadwick et al (1998a) and (1999e) [4] Chadwick et al (1999f).

The flux limits from nine AGN's as described in Chadwick et al. (1999d) and (1999g) are summarised in table 4.5. They are all 3σ flux limits, based on the maximum likelihood ratio test (Gibson et al. (1982)). The threshold energy for the observations was estimated on the basis of preliminary simulations, and is in the range 300 to 400 GeV for these objects, depending on the object's average elevation. The collecting areas assumed, again from preliminary simulations, are 5.5 x 10^8 cm^2 at an energy threshold of 300 GeV, and 1.0 x 10^9 cm^2 at an energy threshold of 400 GeV. Under the current image selection procedure, combined with preliminary Monte Carlo simulations, ~20% of the original gamma-ray events were retained for sources observed at less than 45° zenith angle, these results were subject to systematic errors estimated to be ~50%. A major aim of the current study is to refine these values to obtain a better estimate of the flux from PKS 2155.

Object	Estimated Threshold (GeV)	3σ Flux Limit ($x10^{-11} cm^{-2} s^{-1}$)
Centaurus A	300	5.2
PKS 0829+046	400	4.7
PKS 1514-24	300	3.7
1ES 23 16-423	300	4.5
1ES 1101-232	300	3.7
RXJ 10578-275	300	8.2
1ES 0323+022	400	3.7
PKS 2005-489	400	0.79
PKS 0548-322	300	2.4

Table 4.4: Three sigma DC flux limits for nine AGNs observed by the Mk6 telescope between 1996 and 1999. All observations were made below 45° zenith angle (Chadwick et al. (1999d) (1999g) (2000a) and (2000b)).

CHAPTER FIVE - EAS & Telescope Simulations

5.1 Introduction

Ground-based observations of VHE gamma-ray emitting astrophysical objects involve the extraction of a weak signal from a much more intense background signal. Even in the particular case of the Crab nebula, the strongest known source of continuous VHE gamma-ray emission, the signal flux is a minute proportion of the nucleon induced background signal, at much less than 1%. Due to the extremely low count-rate for gamma-ray events as compared to background events, it is not often possible to experimentally determine the precise characteristics of the images of gamma-ray induced events, as observed by any particular Imaging Atmospheric Cherenkov Telescope (IACT) at any given location. The effects of atmospheric considerations, the elevation of the observing site, telescope-dependent details and the details concerning how the image data are treated post-observation. All of these have a significant effect upon the precise size and shape of each event image.

It is certainly possible to discover a 'signal' by trial and error guided by some analytical knowledge of the general trends in the inherent differences between gamma-ray and nucleon induced shower images, although the large number of degrees of freedom which this method necessarily implies means that any signal found can only be considered to be real (rather than simply a random peak in the background noise level) if the volume of parameter space determined to contain a signal is then applied to an independent data set with similar results. Considering the

long periods of observation necessary to obtain a signal even from the brightest sources of VHE gamma-rays, this ad-hoc trial-and-error practice is very inefficient and prone to false identification. The only truly justified method of signal identification is through accurate simulation, excepting cases of extremely high emission rates or extremely long observation periods.

The principal shower characteristics which need to be accurately described by simulations are the lateral distribution of Cherenkov light on the ground, the angular distribution of the shower on the celestial sphere and the temporal and spectral profile of the Cherenkov emission. The extent to which a given set of simulations can predict the properties of proton showers, which are observed experimentally, is an important indicator of the degree of confidence one may place upon the predictions of the photon initiated shower simulations.

Early shower simulation methods were analytical in nature; the computing capability required to undertake detailed Monte Carlo calculations only became available after the advent of modern computers. Monte Carlo based simulations can, in principal, trace the evolution of every particle within an Extensive Air Shower (EAS), though this is often an inefficient use of computer time, and a number of methods are utilised to reduce the computing time required to produce a large number of shower simulations. However great care needs to be taken that these time-saving devices do not introduce significant systematic bias into the shower simulations. Simulations may also be required to predict the response of a particular telescope to simulated Cherenkov showers, and here again great care needs to be taken that all pertinent

information regarding the telescope's performance be contained within these simulations.

5.1.1 Historical development of simulations.

The first notable calculations based on an analytical approach were carried out by Zatsepin and Chudakov (1962a&b) and concerned the lateral distribution of Cherenkov photons from gamma-ray and nucleon (protons only) initiated EAS. The Lateral Distribution Functions (LDFs) of the Cherenkov photons produced by primary VHE gamma-rays with energies of 0.1 and 1 TeV were found to be relatively flat out to a radius, r ~ 100 m, from the hypothetical impact point of the initiating VHE gamma-ray photon. A small increase in the photon density was apparent at a distance of about 120m (this is a consequence of the focusing effect produced as the average emission angle of Cherenkov light increases as the shower develops. See section 2.2.3), followed by a steep fall off in photon density beyond 120m, at a rate of roughly r^{-2}. The LDFs of proton initiated showers were found to be similar but not as flat. The most notable feature was the lack of a 'focusing hump' seen in the LDFs of gamma-ray initiated EAS. Calculations were produced at both sea level and 3860m. The predicted distributions for protons at both altitudes were compared with experimental data and were found to be in reasonable agreement. With the advent of the computing capability to conduct large-scale Monte Carlo simulations, it became possible to take into consideration the effects of pair production, Bremsstrahlung, Compton scattering, direct pair production by electrons, ionisation losses and multiple scattering upon the development of EAS, and to produce a statistically large

data set of EAS simulations. Simulations of purely electromagnetic showers were conducted by Rieke (1969). Some reasonable shower approximations were made to reduce the computing time necessary to produce these simulations; e.g. particles were no longer followed after they went beyond a depth of twenty radiation lengths or their energies dropped below 21.5 MeV or if their directions of motion made an angle greater than 90° with the shower axis. Rieke (1969) produced a total of 250 individual VHE gamma-ray initiated EAS simulations, incident vertically to the Earth's surface. An averaged shower model was constructed by combining the outputs from the 250 individual simulations. This supplied detailed information concerning the longitudinal, lateral and angular distributions of the shower particles and Cherenkov photons, and the first detailed information concerning the temporal and spatial characteristics the shower front. The analytical simulations of Zatsepin and Chudakov (1962a) and (1962b)) were in good agreement with the Monte Carlo simulation results of Rieke (1969) at least in relation to the lateral distribution of Cherenkov light, as illustrated in Figure 5.1, overleaf.

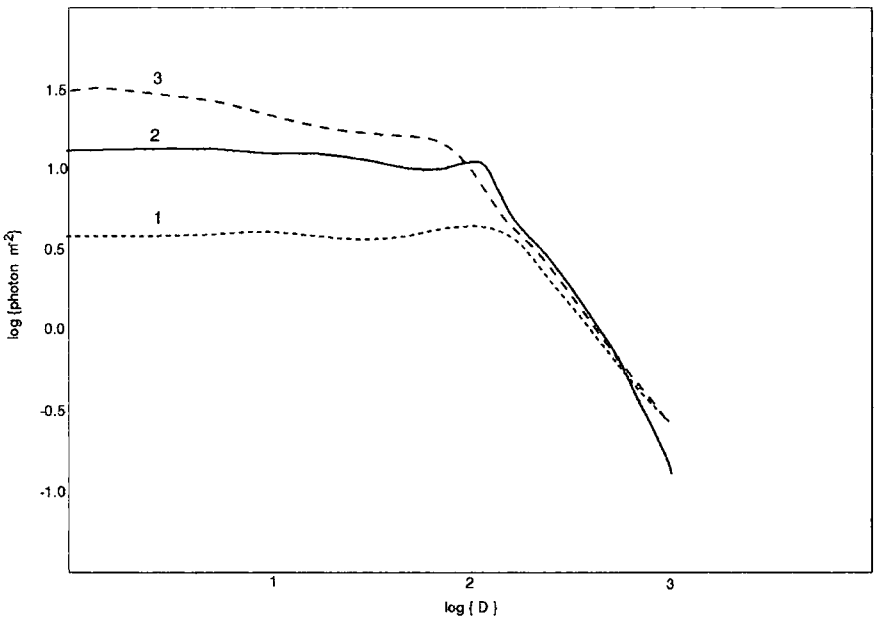

Figure 5.1: Lateral distribution of Cherenkov light for 0.1 TeV gamma-ray photon initiated EAS. (1) Zatsepin and Chudakov (1962a), sea level. (2) Rieke (1969), 2320m. (3) Zatsepin and Chudakov (1962b) 3860m, (from: Rieke (1969))

5.1.2 Further Monte Carlo studies

The presence of large fluctuations in individual gamma-ray induced EAS showers was ascertained by Browning and Turver (1977); this had not been seen in the earlier simulations of Rieke (1969) and Castagnoli et al (1972). The immediate impact of this discovery was to necessitate the recalculation of energy thresholds for contemporary detectors. The Whipple Observatory 10 m detector for example was determined to have an energy threshold a factor of three lower than had been evaluated using previous simulations. The major ramification of these simulations was the assertion that the angular distribution of Cherenkov light from electromagnetic cascades would be so distorted by fluctuations that its use in the

separation of gamma-ray induced Cherenkov events from the background nucleonic initiated events would be questionable.

Turver and Weekes (1978) compared a series of Monte Carlo simulations concerned with the LDFs of EAS nucleon (protons only) induced showers, with gamma-ray simulations conducted by Browning and Turver (1977). The comparison of nucleon induced EAS showers of energies 0.1 TeV, 1 TeV and 10 TeV with these gamma-ray simulations identified a potentially discriminating difference between the two types of shower. Turver and Weekes (1978) determined that the intensity of Cherenkov light from a gamma-ray initiated EAS showers of primary energy 10 TeV was greater by a factor of two than that from a proton initiated shower of the same energy. For primary energies of below 10 TeV this ratio increased dramatically, reaching a value of 14 at 0.1 TeV. Thus, traditional Cherenkov detectors operating at these energies should, be more sensitive to gamma-ray showers than proton showers. Turver and Weekes (1978) proposed the use of a detector system, comprising two telescopes located about 100m apart, each with a detector array of 37 photomultiplier tubes as a possible system to achieve a low (~0.1TeV) energy threshold. The use of imaging arrays of photomultiplier tubes subsequently proved to be of great use in the the detection of gamma-ray induced Cherenkov events.

5.1.3 Monte Carlo simulations and Cherenkov imaging

The application of the Cherenkov imaging technique to the detection of VHE gamma-rays has been strongly influenced by the encouraging results of Monte Carlo

simulations conducted by many authors. For example Plyasheshnikov and Bignami (1985) carried out Monte Carlo simulations of both gamma-ray and nucleonic (proton only) showers in the energy range 0.1 to 2 TeV. These were then used as source material for further simulations of the Whipple Observatory 10 m detector, simulations of how the Cherenkov radiation from these showers would appear within the FOV of the prime focal plane of the telescope. The conclusion drawn was that there would be sufficient information recorded in these images to distinguish between the Cherenkov light signals observed from gamma-ray and proton initiated EAS.

The primary distinguishing features discussed within the context of the results were firstly, shower image orientation, with gamma-ray event images aligning with the location of the source position, and secondly the presence of larger fluctuations in the nucleon induced shower images, in direct contradiction with the results of Browning and Turver (1977). One result of particular interest is that Plyasheshnikov and Bignami (1985) found the angular dimensions of the two shower image types to be quite similar and, as a result of this, ruled out the use of image size as a potential gamma-ray/proton initiated shower discriminatory factor. However this was later found to be incorrect (Hillas (1985)).

Hillas (1985) used the Monte Carlo simulation method to determine the behaviour of shower particles in a non-isothermal atmosphere. Thin sampling was used (a method in which a weighting factor is assigned to some low energy particles to take account of those particles not followed in their entirety). This helps to significantly reduce the computation time required for Monte Carlo simulations of VHE showers, where

previously limitations upon computer time would have limited simulations to purely analytical methods (Hillas, 1981). Thinning is not used in the present analysis as it is not necessary below about 30 TeV. Hillas (1985) found a number of image parameters which could be used to distinguish between gamma-ray and nucleon initiated showers based on his simulations. These were summarised in the previous chapter (see section 4.3.3).

5.1.4 Monte Carlo simulation programs

The problem to be solved with cascade simulation programs is the development of a inverted cascade tree in Monte Carlo fashion, see figure 2.3. The loci of each branching vertex and the number and properties of the lines emanating from them are to be chosen randomly from appropriate probability distributions. Vertices represent either particle decay of the incoming particle or interactions with other particles. The lines represent the path length between interactions or decay, whichever occurs first. A problem which needs to be treated by all simulation programs is the division of energy between particles arriving at a vertex and those leaving. In addition to this, the lateral momentum of outgoing particles is of paramount importance to the transverse structure of the cascade. There are currently many different Monte Carlo based simulation programs which exist for analysing experimental data on EAS or for planning new experiments, e.g. CORSIKA (COsmic Ray SImulations for KAscade) Heck (1999), MOCCA (MOnte Carlo CAscade) Hillas (1981, 1985, 1995), ALTAI (Atmospheric Light Telescope Array Image) Konopelko & Plyasheshnikov (2000), CHESS (CHerenkov and Electromagnetic Shower Simulator) Vassiliev et al (1997).

The simulation program MOCCA was developed by Prof A. M. Hillas to study EAS in the energy range 10^{10} to 10^{21} eV and has been used extensively for modelling the behaviour of the Durham Mk6 telescope (Shaw (1999), Chadwick et al. (1999a)).

5.2 MOCCA

The most notable feature regarding MOCCA, as compared to other simulation programs is the relative simplicity of the algorithms used to describe nucleonic interactions. This simplicity should not be considered to be a disadvantage as it enables rapid simulation and, as will be shown in the next chapter, MOCCA is at least comparable to other more complex simulation programs that treat the nucleonic interactions in a more theoretically 'correct' manner.

5.2.1 The treatment of particles within MOCCA

MOCCA recognises a number of different types of particle and intermediate particles.

Particle Types:

*Glueball: intermediate state of nucleon collision, progresses into pion.

*Fireball: intermediate state of photopion production, progresses into nucleon + pion or two pions.

*Pion: Type of meson, may be +ve -ve or neutral.

*Nucleon: Type of baryon, may be +ve or neutral.

*Neutrino: type of lepton, no charge & no mass.

*Muon: Type of lepton, may be +ve or -ve

*Electron: Type of lepton, may be +ve or -ve

*Nuclei: A group of nucleons (equal numbers of +ve and neutral), may be fragmented into smaller nuclei, nucleons and gluons.

*Photon: May convert into two electrons.

These particles are assigned properties e.g. type, energy, propagation vector, charge, etc. Subroutines are activated to decide whether or not a particle has decayed since its last interaction, or its creation, or after progressing some distance along its path. The particles' properties are assessed and appropriate action taken (e.g. decayed/not-decayed) and it is noted whether any new particles have been produced (for instance, decay products). New particles (along with their assigned properties) are then followed along their courses and appropriate action taken regarding their subsequent interactions/energy loss/decays etc. In this way a complex cascade tree of branches (particle path lengths) and vertices (points at which particles either interact or decay) is built to represent the reality of an EAS. A significant quantity of information is needed to decide the fate of individual particles, the half lives of unstable particles, differential production cross sections for interactions, the rates of energy loss due to Bremsstrahlung/ionisation, decay products and typical properties of decay products, and scattering must all be considered. Finally all of this information needs to be placed within the framework work of Monte Carlo calculation to decide the fate of individual particles.

5.2.2 Heavy nucleus fragmentation

The break up of heavy nuclei upon striking an air nucleus is treated sparingly and without unnecessary complexity within the MOCCA simulation code. The binding energy of nuclei is ignored as it is insignificant when considering high energy interactions. The average number and type of fragments depends on the mass number of the initiating particle. Except for protons, it is always assumed that the mass number of a nucleus is an even number as it is defined as twice the charge of the particle. The number of freed protons/neutrons is always even and thus the number remaining bound is always even; the precise number of freed protons/neutrons depends on the mass number of the initial nuclei and obeys different functions for mass numbers in the ranges <15, >15 and >23. The emission of alpha particles (mass number = 4) is also considered.

For the nuclei remaining after collision (i.e. after considering the loss of protons and neutrons) of mass number >15 one alpha particle will be produced; for mass numbers >23 two alpha particles are produced. In addition, all nuclei of mass number = 8 are broken up into two alpha particles (to represent the behaviour of the highly unstable beryllium 8 isotope). The kinetic energy of the initiating particle is divided equally between all of the nucleons in the resultant nuclei, whether they are individual protons/neutrons, within alpha particles, or remain bound within what remains of the initiating nucleus. All of the alpha particles, and those individual nucleons which have been designated as undergoing elastic collisions, will simply be followed along within the body of the simulation program (using the routine PROPAGATE), though

a proportion of the individual nucleons liberated in the fragmentation process will be designated to have undergone inelastic collisions which will produce other particles (e.g. pions) and be treated by the subroutine COLLISION (see section 5.2.3).

5.2.3 The MOCCA energy splitting algorithm

Like most programs which have been in use for a number of years, many additions and revisions have been made to MOCCA since its initial formulation. To describe the algorithms used within MOCCA, the initial formulation of the energy splitting algorithm will be presented and then some mention of the important additions and revisions which occurred in later years will be made. The basic nucleonic energy splitting algorithm, paraphrased from the presentation in Hillas (1981) states:

i) Split the Total energy available into two random parts, A and B.

ii) Assign energy A to the leading nucleon.

iii) Further subdivide energy B randomly into J = 4 parts.

iv) Subdivide each J = 4 energy fragment randomly into two parts, A′ and B′.

v) Assign A′ as the energy of a pion.

vi) Subdivide B′ and assign one energy fragment as the energy of another pion.

vii) Continue in this fashion until the energy remaining is less than some predefined threshold value (the energy threshold will depend on the problem at hand, but must be at least as large as the rest mass energy of a pion, m_π).

The principal feature of this algorithm is that energy is automatically conserved, and all of the energy splitting occurs in the laboratory frame, hence there is no need for

Lorentz transformations. In addition, no time is wasted in calculating the parameters of particles with energies below which they have no observable effects. In this original formulation the average elasticity for nucleon-nucleon collisions is obviously 50%, as the energy is split randomly and without bias. The fractional energy distribution for leading nucleons is thus flat, i.e.,

$$F_{N\text{-}N}(x) = x \frac{dn}{dx} = x.$$

This distribution has since been modified by simply choosing the energy available to the leading nucleon according to the best available fit to proton-nucleus interaction data. As described in Hillas (1997), this modification has been made in post-1992 MOCCA versions (MOCCA92 & Mocveri) and results in the average elasticity of nucleon-nucleon collisions being reduced to ~41% from the original 50%. The energy assignment for fragments (glueballs) is derived by randomly splitting the total available energy into J fragments, and selecting the number of energy fragments that will become glueballs using the following Monte Carlo expression:

$$J \rightarrow \text{Integer part of } [\ (4.35\ .\ \text{Rand}\ ) + 3\ ]$$

where J is the number of fragments to be assigned the intermediate particle type 'glueball' and Rand is a random number between 0 and 1. The sum of the energy assigned to these fragments is then removed from the total available energy that the initiating particle originally provided. The above function ensures that at least three glueballs and at most seven will be produced, though the probability of producing seven glueballs (i.e. J = 7) is only ~8% as opposed to a ~23% probability of producing J = n glueballs, where $3 < n < 7$. On average, 58.75% of the initiating particles' available energy will be converted into glueballs, i.e. nuclei-nuclei collision

elasticity ~ 41.25%. An analytic form for the energy distribution of the pions resulting from the original splitting algorithm (Hillas 1981) may be found, i.e.,

$$F_{N\text{-}\pi} = x_\pi \frac{dn_\pi}{dx_\pi} = x_\pi 2^N \left\{ \frac{1}{x_\pi} - \sum_{n=0}^{N} \frac{\left(\ln \frac{1}{x}\right)^n}{n!} \right\}.$$

The logic behind the derivation of this function may be found in Gaisser (1990). As for the case of the leading nucleon, this fractional energy function represented above is for the case of the original splitting algorithm and will be slightly different for versions MOCCA92 and later, to take account of the revised elasticity of the nuclei-nuclei collisions.

5.2.4 Transverse particle momenta within MOCCA.

The particles produced at each vertex in the shower cascade tree will be assigned values of transverse momenta. Accuracy is important if the simulations are to reproduce the lateral distributions observed in real EAS. Within high energy nuclei-nuclei collisions the transverse momentum distributions for the produced particles are known to reflect the momentum distributions of their constituent partons, and these distributions are believed to scale with the incident energy. The hypothesis which governs this process is known as the Hypothesis of Limiting Fragmentation (HLF) and is the main Hypothesis behind Yen scaling (Yen 1974). For particle types produced at cascade tree vertices through reactions of the form, $a + b \rightarrow c + X$, the inclusive cross section σ_1 of finding a single particle 'c' in a small region of invariant phase space, regardless of what else is produced will be of the form,

$$\sigma_1 = E_c \frac{d^3\sigma_{ab}}{dp_c^3}\left(\sqrt{s_{ab}}\ ,\ p_{\|}^*,\ p_t\right) \equiv f_{ac}^{(b)}\ \left(\sqrt{s_{ab}}\ ,\ p_{\|}^*,\ p_t\right)$$

where $\sqrt{s_{ab}}$ is the total centre of mass energy of the initial system a + b; p is momentum and * indicates the centre of mass frame. Assuming HLF to be true the above expression reduces to,

$$f_{ac}^{(b)}\ \left(\sqrt{s_{ab}}\ ,\ p_{\|}^*,\ p_t\right) \rightarrow f_{ac}^{(b)}\ \left(x^*,\ p_t\right),\ \text{for}\ \sqrt{s_{ab}} \rightarrow \infty$$

where x^* may be defined in a number of ways dependent on the precise assumptions made in the HLF hypothesis. The nature of x^* can to some extent be decided upon depending on the problem at hand, but it is essentially a factor relating the resultant particle's energy and the total energy available. If x^* is defined as $x^* = E^*/E_0{}^*$, and the maximum energy available is taken to be $\frac{1}{2}\sqrt{s_{ab}}$, then it becomes convenient to define that $E_0{}^* = \frac{1}{2}\sqrt{s_{ab}}$ and thus that $x^* = 2E^*/\sqrt{s_{ab}}$. In essence therefore, the above function suggests that in the high-s limit, $E_c d^3\sigma/dp^3$ becomes independent of 's' for given (x^*, p_t). The variable x^* has become known as the '*radial*' scaling variable x_R.

To relate $E_c d^3\sigma/dp^3$ to $f_{ab}{}^{(b)}(x_R\ ,\ p_t)$ one needs to multiply by the inelastic cross section for the reaction a + b → c + X, i.e. σ_{ab}; thus,

$$\lim_{s\rightarrow\infty}\ E\frac{d^3\sigma_{ab}}{dp_c^3} = \sigma_{ab} \cdot f_{ac}^{(b)}\ (x_R,\ p_t)$$

where p_t is the transverse component of momenta for particle c. Fits to the function $f_{ab}{}^{(b)}(x_R\ ,\ p_t)$ can be found experimentally. If the HLF is true then fits to graphs of $E_c d^3\sigma/dp^3$ vs x_R at fixed p_t for relatively low energy a + b → c + X interactions may be made and applied to higher energies. Experimental data for the interaction a + b →

c + X need to be obtained for p-p primaries and for each possible permutation of c (e.g. neutral and charged pions, matter and antimatter, nucleons etc, and appropriate fits derived). Fits of this kind have been made to experimental data and are incorporated within standard MOCCA versions (Hillas 1979). It is clear that experimental data will be needed to reform $f_{ab}^{(b)}(x_R , p_t)$, such that it can be utilized within a Monte Carlo structure. This will be of the form,

$$f_{ac}^{(b)}(x_R , p_t) = A(x_R) . e^{-\left(B(x_R) . p_t^{C(x_R)} \right)}$$

where A, B and C all, in general, vary with x_R. Hillas (1979) presents a number of functions representing $A(x_R)$, $B(x_R)$ and $C(x_R)$ for differing product particle species.

When considering relatively low energy nucleonic primaries, <10s of TeV, it becomes possible to make some bold simplifications to the above equation, starting from the approximation that the probability of finding a value of p_t is,

$$P(p_t) \propto e^{-\frac{p_t^2}{x_R}} .$$

After rearranging this equation and re-representing it in a form suitable for Monte Carlo calculations, with random numbers included, this equation becomes,

$$p_t^2 = \left[- x_R . \ln(Rand_1 . Rand_2) \right]^2 .$$

This is the form used for the calculation of p_t in post-1992 versions of MOCCA. Having knowledge of the total momentum of the particle in question it becomes simple to calculate the relative vector (relative to the direction vector of the incoming nucleon) taken by a particle created at a vertex in the branching tree. The azimuthal

angle ϕ for these new branches takes a random value between 0 and 2π. In Monte Carlo form this is simply,

$$\phi = 2\pi \cdot \text{Rand} .$$

5.2.5 Particle type and charge assignment for Glueballs

Within the MOCCA procedure COLLISION, after the number and energy of collision products (i.e. glueballs) has been decided, the glueballs progress into Pions and thus the charge of these resultant pions must be chosen. Firstly one must decide whether the initiating particle changes its charge. The average probability of this is ~70% (protons turn to neutrons and vice versa). The pion which has the highest proportion of the available energy will be assigned the appropriate charge, charge being conserved. After this the remaining pions are assigned positive, negative or neutral charges randomly and with equal probability and thus at this stage charge may not be conserved for an individual collision. The condition that the highest energy pion will retain any charge lost by the initiator reflects what occurs in reality.

5.2.6 Electrons and gamma-ray photons

Within MOCCA, as with nuclei and nucleons, there are a number of procedures which simulate the behaviour of electrons and HE photons. There is an electromagnetic component within EAS induced by nucleons as well as gamma-rays, and both are treated by the same group of procedures. For electrons, the initial factor is to decide the fate of an electron; either energy loss due to Bremsstrahlung or

annihilation. In the case of Bremsstrahlung emission, a check is made to see if the energy of the electron is above a given level. If this is true then the electron will probably emit a Bremsstrahlung photon, following the acceptance test given by Rossi and Greisen (1941), which is intended to reproduce the differential cross-sections for Bremsstrahlung.

Annihilation is only an option for positrons which have lost practically all of their kinetic energy and are essentially at rest; in-flight annihilation is not considered to be a significant possibility. Energy loss via ionisation is treated as a continuous energy loss mechanism. For high energy gamma-ray photons within an EAS the important interactions are electron pair production and photo-nuclei interactions. Although the cross section for interactions of gamma-rays and nuclei is small, this process does allow for the production of muons in otherwise purely electromagnetic showers. At lower gamma-ray energies Compton scattering becomes important and at the lowest energies photo-electric absorption becomes highly significant.

5.2.7 Cherenkov photon emission.

Cherenkov light emission is calculated for all charged particles above their Cherenkov emission thresholds. The probability of a Cherenkov photon being emitted is resolved in terms of frequency with equal probability per frequency interval, between 270nm and 685nm, as below 270nm Cherenkov photons will be strongly absorbed by the atmosphere, hence there is little point in calculating their progress through the atmosphere. This process naturally gives a λ^{-2} wavelength spectrum

which well represents the Cherenkov spectrum. A determination is made then as to whether an individual photon of given wavelength would produce a photoelectron, given the effects of atmospheric absorption and and detector quantum efficiency. These factors are stored in the form of lookup tables. If a particular Cherenkov photon would produce a photoelectron, then it is then determined whether or not this photon has impinged upon a telescope mirror; in this way the time-consuming process of determining which mirror a particular photon would hit only becomes necessary if the photon in question will produce a photoelectron. The angle to the charged particle's vector at which Cherenkov photons are emitted depends on β and the refractive index of the medium (see section 2.3.1); the Cherenkov angle defines a cone around the charged particle. If this cone intersects a mirror, then a proportion of the emitted Cherenkov photons will be recorded. This proportion depends on the fraction of the Cherenkov emission cone bisecting the detector's mirror. A number of mirrors or mirror groups can be defined at different positions within the light pool of a simulated EAS so that a number of samples of the same shower may be collected.

5.2.8 MOCCA output and IACT simulations

MOCCA output files for use in IACT simulation programs contain information on only those Cherenkov photons which have survived the attenuation due to atmospheric absorption, mirror reflectivity, PMT quantum efficiency and have impinged upon a telescope mirror. In addition, information concerning the direction vector of the Cherenkov photon (or rather the photoelectron produced), relative to the telescope mirror and the time of arrival, are also recorded in the output file. The

arrival time is taken relative to the time of arrival at the ground of some imaginary highly relativistic particle, travelling from the point of first interaction of the shower initiator directly along the shower axis without interacting.

A program (Presol) is needed to read through the MOCCA output file to record the minimum photon arrival time for each shower and for each telescope position. This time is subtracted from the recorded times, so that the time used by the telescope simulation program 'SOLMK' is set relative the the arrival time of the first photon. In order to increase the amount of available information, MOCCA samples each shower at five randomly selected telescope positions within a certain area, the radius of which is determined by the energy and zenith angle of the EAS events in question. This is done within a plane normal to the shower axis and around the shower axis. As the Mk6 telescope consists of three mirrors, the output for each photon detected will consist of a direction vector, the position upon the mirror, relative time of arrival and the telescope and mirror number upon which the photon impinged.

5.3 The SOLMK IACT Monte Carlo simulation program

The first objective of the SOLMK program is to take the output information from MOCCA concerning the vectors, positions, relative arrival times, telescope and mirror numbers, for the photons detected from each shower and to decide if the Mk6 telescope would have been triggered by any particular shower sample. For this to be achieved, SOLMK requires information regarding the salient properties of the Mk6 telescope in addition to the easily derived characteristics, such as the size and geometry. There are also other factors which may need to be derived either experimentally or iteratively by comparing the simulated results with observations, such as the point spread function (PSF) of the telescope mirrors, the size and position of each of the photomultiplier tubes in each of the detector packages, a pulse profile for the response of a photomultiplier tube to a single photoelectron liberated from the photocathode and a gate time within which a preset discrimination level is to be attained for a photomultiplier tube to trigger. If enough photoelectrons arrive over a short enough time period, the sum of the single pulse profiles (SPPs) will reach above this discriminator level. In addition to the SPPs resulting from Cherenkov photons, there is a probability that night sky background photons will induce noise in the form of additional SPPs arriving at random intervals. If the discriminator level is reached in a number of tubes and fits the triggering pattern set for the Mk6 telescope (see section 4.2.3) then the responses of all the PMTs to all the Cherenkov photons

arriving at them will be summed. The PMT response values obtained will be in units of photoelectrons (pe). To convert these values into the digital counts (dc) response which is obtained from PMTs under real observing conditions, a pe/dc conversion ratio has to be obtained. A digital counts to photoelectron ratio may be chosen so as to match the average simulated brightness values in photoelectrons with the average of the observed brightness values in digital counts. At this stage the shower images may be parameterised in exactly the same manner as real images (see section 4.3.3) and a comparison drawn.

5.3.1 Point spread function

A number of estimates have been made of the point spread function (PSF) of the Mk6 telescope. The PSF of the Mk6 telescope is best represented as the superposition of two 2-dimensional Gaussian. This provides the best fit to the central-cross section of a star image upon the focal plane of the Mk6's central mirror. this two component curve will be of the form,

$$f(x) = A\exp^{\frac{-x^2}{a}} + B\exp^{\frac{-x^2}{b}}$$

where the angular size of each component of the PSF can be found from the standard deviation, i.e. $\sigma_a = | \sqrt{(a/2)} |$ for the first component and similarly for the second component. The original measurement at the time of construction was ~0.18° for the first component, another measurement two years later (September 1996), using the same CCD based method, gave an identical result.

A more recent estimate (May 1997) using a solid state photodiode produced a value of ~0.15°. This suggests that the surface quality of the mirror remained reasonably consistent over the three year period after construction. These estimates of the PSF are really only a first approximation; more detailed information is needed if accurate simulation of the mirror behaviour is to be achieved. Upon closer inspection of the CCD based results (Shaw (1999)) the PSF appeared to be composed of at least two distinct components, a *peak* component and a *skirt* component; the estimates given above are for the *peak* component. The *skirt* component is much wider, at about 0.45°, and contains about two thirds of the light within the PSF of the Mk6 telescope's central mirror. There is also likely to be some diffuse scatter of light reflecting off of the mirrors, though as the *skirt* component is already large this is considered to be negligible for the purposes of the simulations. For future reference the PSF will be expressed in the form: Standard deviation of *peak* component (degrees)/Standard deviation of *skirt* component (degrees)/ % of light in *skirt* component, e.g. 0.18/0.45/66 would summarise the PSF of the Mk6 telescope's central mirror.

5.3.2 Single electron pulse profile

To simulate the response of a photomultiplier tube to a single photoelectron, a single electron pulse profile (SPP) must be defined. The typical rise time of a central imaging PMT in the Mk6 central camera is about 2 to 3 ns below 1000V; typical transit times are about 7ns. A pulse profile which rises to maximum in 3ns and falls off to zero after 7ns, therefore, would be a simple yet descriptive representation of the

behaviour of a PMT to an photoelectron liberated from the photocathode. The single electron pulse profile currently used with the SOLMK simulation program is shown in figure 5.2.

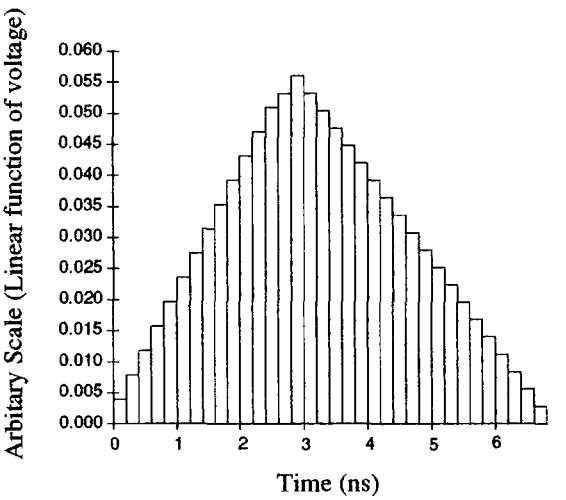

Figure 5.2: The single electron pulse profile adopted for use in the SOLMK simulation program.

5.3.3 dc/pe ratio

In the recorded image data from the Mk6 telescope, the signals received from each PMT and its associated electronics channel are measured in terms of digital counts (dc); this is a measure of the Cherenkov signal incident upon the PMT with additional contributions from the night sky and thermal noise inherent within the PMT. In the simulations, a dc/pe ratio is defined in order to relate the number of photoelectrons actually liberated from the PMTs photocathode to a dc value suitable for comparison with observed events. Estimates of this ratio may be obtained by exposing a PMT to a photon pulse of known intensity and measuring the response in terms of digital counts after the signal has passed through an appropriate length of cable and the PMTs associated electronics. Measurements of this kind have been performed using a

pill of radioactive material (0.02μCu of Am^{241}) embedded within a 10mm diameter pill of scintillating material, placed upon the front surface of a PMT. Results from this kind of experiment suggest values for the dc/pe ratio of about four digital counts per photoelectron (dc/pe ~ 4). The value derived via simulation through matching the means of simulated and observed brightness distributions is dc/pe = 4.5, this value is within the uncertainty of the experimentally derived value.

5.3.4 Simulated triggering

In order for a tube to be triggered, the signal from a PMT must reach beyond a preset discrimination threshold set in arbitrary units, within a gate time of 40ns from the arrival of the first photon. This gate time is divided into 200 segments, each 0.2ns long. The arrival of each Cherenkov photon will contribute one SPP, starting at the arrival time of the photon at the photocathode. The convolution of all the SPPs contributed by the Cherenkov photon-induced photoelectrons arriving within the 40ns gate time represents the voltage vs time profile of the Cherenkov signal from each PMT. In addition to the Cherenkov photon signal, there is a probability that noise-induced photoelectrons will be produced, adding additional SPPs to the convolved Cherenkov pulse profile (CPP).

5.3.5 Background noise level

The level of background noise induced within the simulated PMT responses has a significant effect on the resultant EAS images derived from the simulation of the Mk6 telescope. The effect of noise is to add SPPs to the convolved Cherenkov pulse

profile (CPP) at random intervals and at a level which must be derived iteratively by comparing the simulated image parameter distributions with observed distributions for nucleonic EAS. Noise is added in a Poissonian manner to the CPP and at a level which is dependent upon the basic PMT, mirror and NSB properties, the equation for the mean level of noise in units of photoelectrons is,

$$<\text{Noise}> = SNB_{Noise} \cdot SNB_{Ratio} \cdot A_{Mirror} \cdot R_{Mirror} \cdot Ang_{Tube} \cdot C_{Factor} \cdot S_{Tube} \cdot T_{Int}$$

where SNB_{Noise} is the average night sky brightness level ($SNB_{Noise} \sim 7.7 \times 10^{11}$ pe s^{-1} m^{-2} sr^{-1}), SNB_{Ratio} is a variable parameter within the simulations, A_{Mirror} is the mirror area, R_{Mirror} is the mirror reflectivity, Ang_{Tube} is the solid angle subtended by each tube, C_{Factor} is a factor representing the additional light captured by the PMTs due to the addition of reflective cones Dickinson (1995), S_{Tube} is the tube sensitivity relative to the central imaging PMTs and T_{Int} is the time over which the noise is to be integrated. The Poissonian probabilities of obtaining N photoelectrons within any particular time bin are,

$$N = 0;\ Prob_{N=0} = Exp[- <\text{Noise}>]$$

$$N = 1;\ Prob_{N=1} = Prob_{N=0} - \left[Prob_{N=0} \cdot \frac{Prob_{N=0}}{N + 1} \right]$$

$$N = 2;\ Prob_{N=2} = Prob_{N=1} - \left[Prob_{N=1} \cdot \frac{Prob_{N=1}}{N + 1} \right] \quad .....etc.$$

CHAPTER SIX - Simulation method and results

6.1 Introduction

Outlined in this chapter is a description of the method for determining the sensitivity of the Durham Mk6 telescope to VHE gamma-rays. Simulations have been made of the response of the Durham Mk6 IACT telescope to air showers generated by the MOCCA simulation code, then comparisons made between the simulated and real background data. As a result of this comparison the effective collection area of gamma-ray showers, including the retention factor, has been derived as a function of energy. This information has been combined with our observations of the X-ray selected BL Lac PKS 2155-304 to provide a revised TeV gamma-ray flux value for this object. The previous estimate for the integral gamma-ray flux from PKS 2155-304, derived using preliminary simulations (Chadwick et al (1999b) and (1999c)), was determined to be $4.2 \pm 0.7_{stat} \pm 2.0_{sys}$ x 10^{-7} m^{-2} s^{-1} (above 300 GeV).

To determine the sensitivity of the Mk6 telescope it is first necessary to accurately simulate the response of the Mk6 to the background flux of cosmic rays. The MOCCA simulations of cosmic ray shower images used in this thesis have been made using the MODTRAN standard US atmospheric model, to provide an atmospheric profile of pressure and atmospheric absorption as a function of altitude .

The cosmic ray spectrum assumed for these simulations is similar to the cosmic ray spectrum used by Mohanty et al (1998) to derive a spectra for the Crab Nebula. For

convenience the spectrum used by Mohanty et al (1998) was binned into cosmic ray species groups; protons, alphas, oxygen-like (11 to 28 in atomic number) and iron-like (32, 42 and 56 in atomic number), these particular atomic numbers are chosen to reduce systematic errors. Approximations were made to produce average spectral indices and fluxes for these groups, the results were then mixed in the correct proportions to approximate the complete cosmic ray spectrum. Then an improved version of our in-house Monte Carlo simulation software (SOLMK) was used to produce simulated data on the response of the Durham MK6 IACT to MOCCA shower simulations of TeV gamma-ray showers.

Reliable gamma-ray simulations were obtained by searching for a set of SOLMK input parameters which best reproduced the observed cosmic ray rate and image parameter distributions. Then, the parameter selection applied to the 1996-97 data set for PKS 2155-304, which identified this object as a VHE gamma-ray emitter (Chadwick et al (1999a) and (1999c)), was applied to this simulated gamma-ray data set to determine the energy dependent effective area for the Mk6 telescope.

From the energy spectrum of the retained simulated gamma-rays and our observations an integral flux was derived for PKS 2155-304 above 1.5TeV, and some estimation of the spectral index for this source were made (see section 6.5.3). In addition, we have estimated the 3σ flux limits for a number of similar southern hemisphere objects observed with the Mk6 telescope, see chapter 7.

6.2 The simulation of cosmic ray induced EAS images

Utilizing a cosmic ray spectrum similar to that used by Mohanty et al (1998), a large number of cosmic ray induced EAS were simulated using MOCCA and from these pixilated images were produced using our in-house telescope simulation program (SOLMK). The SOLMK simulation program was used to reproduce the observed triggering rate and image parameter distributions observed in the off source data set, between 25° and 35° zenith, from our observations on PKS 2155-304. The approximations made to the cosmic ray spectra used by Mohanty et al (1998) are detailed in section 6.2.1. The US standard atmospheric model MODTRAN was used to approximate the atmospheric profiles prevalent at the Bohena creek observatory site, see section 6.2.2.

6.2.1 The observed cosmic ray spectrum

The spectra of individual components of the total cosmic ray spectrum can for the purposes of this work be expressed in terms of the total kinetic energy of the nucleus E, a constant E_0, which fits the function of the spectrum at low energy, the spectral index of the particular cosmic ray species γ, and D the flux of a species at 1GeV. The differential spectral flux of cosmic ray species can then be expressed in the form,

$$Flux = D \,.\, (E + E_0)^{-\gamma} \text{ GeV}^{-1}\text{m}^{-2}\text{sr}^{-1}\text{s}^{-1}$$

The spectra of the various cosmic ray components were then expressed in terms of the variables, D, E_0 and γ, and the appropriate values shown in table 6.1 have been chosen as a starting point for the present simulations.

Atomic mass	1	4	11	12	14	16	20	24	28	32	42	56
D	24,500	7,390	1637	1,091	1,028	1,744	384	690	774	192	1870	1560
E_0	4.4	5.6	16.5	15.6	21	21	24	29	34	42	71	95
γ	2.77	2.66	3.05	2.63	2.84	2.63	2.62	2.62	2.62	2.62	2.77	2.62

Table 6.1 The parameters for cosmic ray fluxes quoted in terms of the total kinetic energy of the incident nucleus, taken from Mohanty et al (1998).

These values are not known to a high degree of accuracy, in general the likely systematic error in the total flux rate is probably of the order of ~15% (Mohanty et al (1998)). For convenience in the present simulations the E_0 term has been neglected as this will only have a significant effect in the lower energy ranges and becomes insignificant in the energy range of concern here. The high mass cosmic ray species were binned into two groups, Oxygen-like and Iron-like. The actual values used in the present simulations are given in table 6.2.

Atomic Mass	1	4	11 to 28	32 to 56
D	24,500	7,390	5,083	2,197
γ	2.77	2.66	2.63	2.62

Table 6.2 The parameters for the differential species dependent cosmic ray fluxes quoted in terms of the total kinetic energy of the incident nucleus, used in the present simulations.

Strictly speaking a value of E_0 should have been included for the mass group 32 to 56, as E_0 has at this stage become large enough to cause significant deviation from a power law form; however this approximation is of little concern as this group only contributes about 2% to the total number of simulated triggers (see table 6.5).

6.2.2 Atmospheric profile

In these simulations, fits to a US standard atmosphere were used in order to approximate the atmospheric profile prevalent at the Bohena observatory site, (see

figure 6.1). As we have no knowledge of the actual atmospheric profile at the time of observation, the assumption has been made that a US standard atmosphere is applicable given that it has been produced for a similar latitude, albeit in the northern hemisphere.

There is likely to be some seasonal variation in the atmospheric profile at the Bohena observatory, although the observations for which the present simulations have been made to reproduce were all taken at a similar time of year, so any seasonal variation will be minimised. We show in figure 6.2 some transmission profiles obtained from MODTRAN for electromagnetic radiation passing through the atmosphere from a given altitude to sea level. MODTRAN is a program for deriving atmospheric profiles, patented by the US air Force Philips Laboratory.

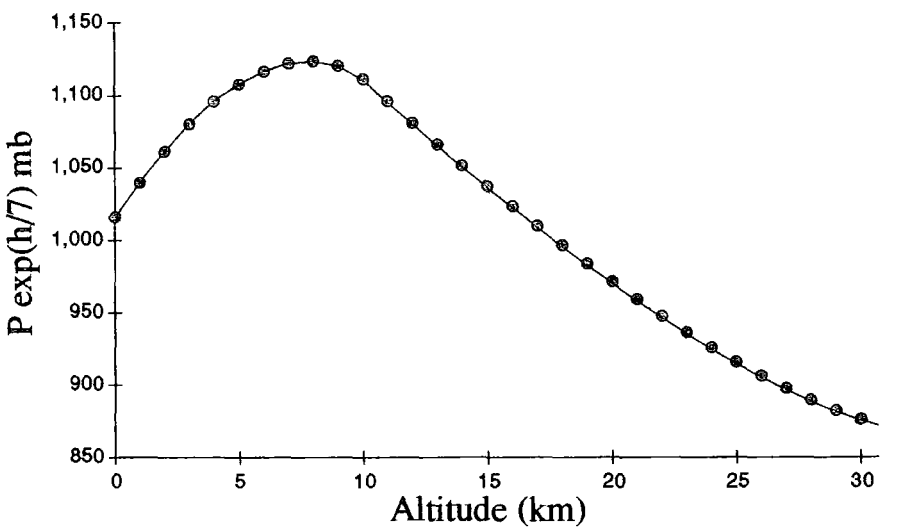

Figure 6.1 Profile of atmospheric pressure against altitude, the dots are points at which the value for the pressure have been tabulated against altitude, the curve is similar to the curve used to fit these data.

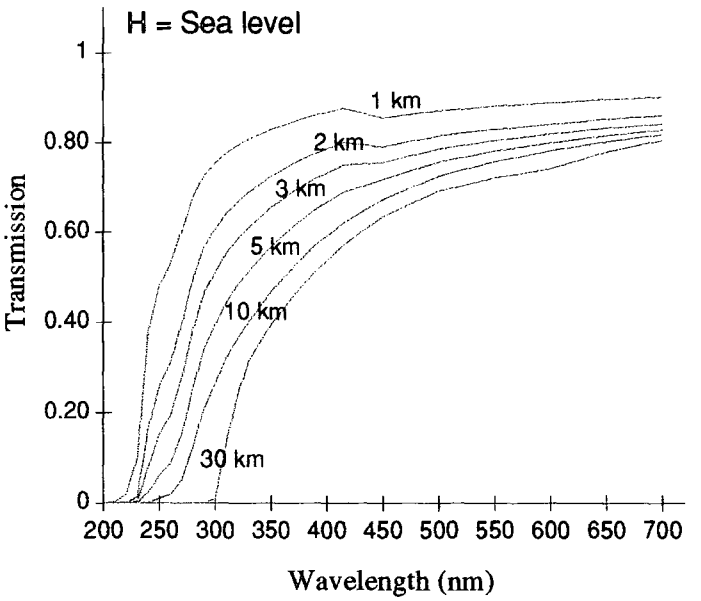

Figure 6.2 An example of transmission profiles as obtained from MODTRAN and utilised within MOCCA. The observation level H is at sea level, although in the simulations the observation level is taken to be 260m (i.e. the altitude above sea level at Narrabri, NSW).

6.2.3 Model dependent parameters in SOLMK

There are a number of model dependent parameters used in the SOLMK telescope simulation program. The values of these parameters have for the most part been derived via comparison of the simulated image parameter distributions with the observed distributions.

Discriminator Level: this is the value (set in arbitrary units) over which the sum of the single photoelectron pulse profiles, induced by a combination of Cherenkov and NSB photons from a simulated EAS, must reach in any one 0.2ns time bin for a particular PMT to be triggered. This must occur within 40ns of the arrival of the first Cherenkov photon at the PMT.

Point Spread Function (PSF): the PSF of the Mk6 telescope mirrors has been experimentally determined to be well described by the superposition of two 2-dimensional gaussian distributions of standard deviation 0.2 ± 0.02^{o} and about 0.45^{o}, with about 2/3 of light falling within the 0.45^{o} gaussian. These values were measured shortly after the construction of the telescope, additional measurments made in September 1998 using a different method provided confirmation of these values to within error. Increasing the PSF within the simulations has a tendency to reduce the rate of triggers and increase the mean width of event images.

Digital Count per Photoelectron Ratio: the distribution of image brightness within the observed events are recorded in terms of digital counts (dc) although the incident Cherenkov signal as output by MOCCA is in units of photoelectrons (pe). It is therefore necessary to determine the ratio for conversion dc/pe. This ratio is set by scaling the size distribution of simulated events to match the mean of the observed image size distributions, when these distributions coincide we find the appropriate conversion ratio. The value of dc/pe derived in this way for the present simulations is 4.5. Some measurements of the dc/pe ratio have been made (see section 5.3.3), and experimentally determined to be at about the 4 digital counts per photoelectron level, which is in good agreement with the value derived through simulation.

Sky Noise Factor (SNF): this is a simple factor, $0<SNF<1$ which is multiplied by a sky noise value of 7.7×10^{11} photons s^{-1} sr^{-1} m^{-2}. Its main effect is to alter the background PMT noise level, which in turn significantly affects the process of image tube selection for image parameter derivation. See section 4.3.1.

Guard Ring Sensitivity: the sensitivity of the guard ring PMTs is expressed as a relative sensitivity as compared to the central camera imaging tubes. Its value has a strong influence on the mean camera centred distance of event images and a complex effect on the image shape and alpha distributions. This value is optimised by comparison of the distance distributions in both observed and simulated background events.

Left-Right Sensitivity: similar to the guard ring sensitivity, the left-right sensitivity is also set relative to the central camera imaging tubes. As would be expected it has a strong effect upon those parameters which utilise information from the images of events in the left and right detector packages. Though in addition to this it has a strong effect on the telescope trigger.

6.3 Matching the cosmic ray event rate and image distributions

A total of 30,863 cosmic ray shower simulations have been performed in a continuous spectrum between 0.1 and 30 TeV using the Mocveri version of MOCCA92. This version of MOCCA was written by Prof A. M. Hillas for use in simulating the behaviour of the Veritas array of IACTs. Mocveri has been modified for our purposes. Changes were made to factors such as the size and location of the telescope mirrors and the format of the output files. Importantly, none of the physical models have been altered.

The species dependent numbers of showers simulated are given in table 6.4. The relative proportions of showers simulated for each species have been chosen such that the resultant numbers may simply be added together to reproduce the correct total cosmic ray spectrum.

Species	Number generated
Protons	13223
Alphas	7965
Oxygen group	6625
Iron group	3050
Total	33563

Table 6.4 The numbers of cosmic ray showers generated using MOCCA. The ratios were chosen to provide a realistic cosmic ray composition.

MOCCA samples each shower generated at five random telescope positions within an area perpendicular to the shower axis and bounded by a circle of radius 300m. Then SOLMK applies an additional four random angular offsets to the photon arrival directions at the mirrors given in the MOCCA output. These offsets are randomly chosen within a cone, of half angle 2°, which is judged to be sufficiently larger than the FOV of the camera as to include all of the cosmic ray shower images that have a significant probability of triggering the telescope. Thus a total of twenty samples were taken of the Cherenkov light distribution for each simulated cosmic ray EAS.

6.3.1 Variations in background cosmic ray distributions

Analysis has been conducted of the event rate and image parameter stability of background cosmic ray events, as observed by the Durham Mk6 IACT, to assess the degree of variability in the image parameter distributions between observations. It has

been noted that some variation in event rate (~10%) does occur between background cosmic ray observations taken at similar zenith angles, with a smaller population of data segments occurring with significantly large deviation from the norm, see figure 6.3. This kind of variation has been shown by Buckley et al (1999) to be strongly correlated with atmospheric clarity. Variations in event count rate are shown in figure 6.4 to have a significant effect upon the image parameter distributions of cosmic ray events. This variability in cosmic ray image parameters presents a difficulty for accurate simulation of background event images. Matching simulations to an averaged set of image parameter distributions, observed under various atmospheric conditions that may not be accurately represented by a single atmospheric model, will likely induce some degree of systematic bias, see section 6.6.2.

In relation to the present simulations, all of the off source data in the PKS 2155 data set used by Chadwick (1999a) and (1999b), lying between 25 and 35 degrees zenith angle, have been chosen as a benchmark to be simulated. The present simulations have been conducted for a zenith angle of 30 degrees and an azimuth of 180 degrees. It can be seen from figure 6.6 a&b that there is no significant bias over and above that caused by variations in atmospheric clarity, induced by zenith angle dependent trends in count rate or image shape, over the 10 degree zenith range around 30 degrees zenith.

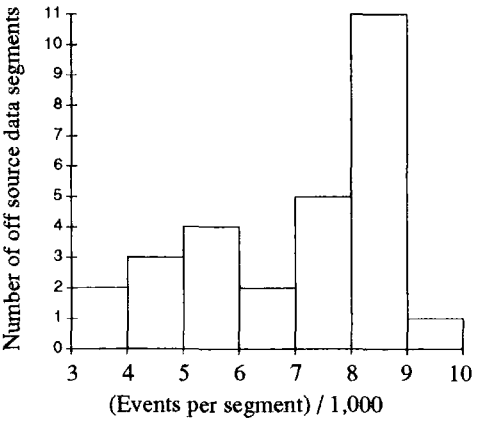

Figure 6.3 The distribution of off source data taken between 25 and 35 degrees zenith (and at various azimuth angles), significant variation in event count rate can be seen between data segments.

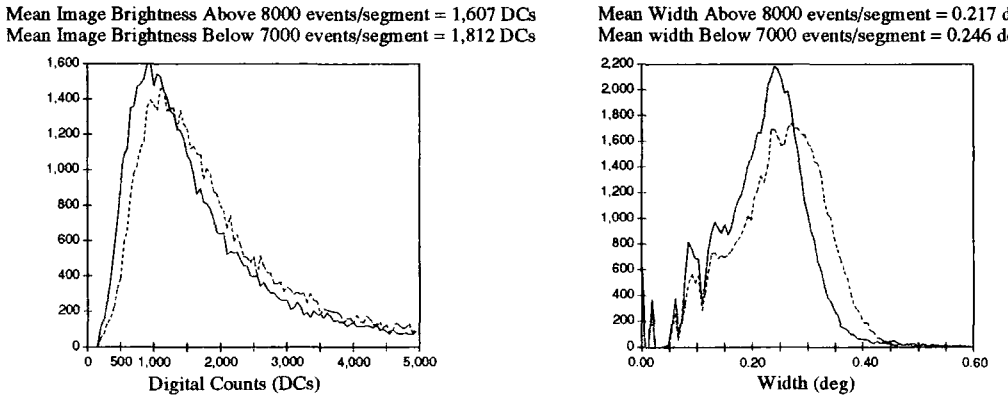

Figure 6.4 Differing image parameter distributions observed between off source data segments containing significantly differing numbers of events.These graphs have been normalised such that both curves have the same area.

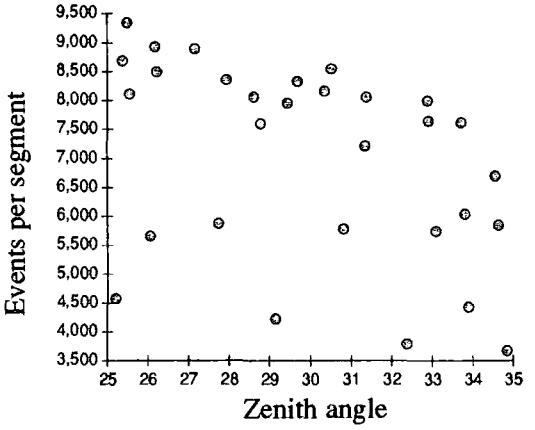

Figure 6.5 Counts per segment versus zenith angle for off source data taken between 25 and 35 degrees zenith.

6.3.2 Event rate

When simulating the response of an IACT to the background flux of cosmic ray events, the primary parameter to be matched is the raw rate at which real events trigger the telescope. For each cosmic ray species of the simulated trigger rate R_{trig} is related to the number of simulated triggers n_{trig} by

$$R_{trig} = \frac{n_{trig}}{n_{shower}} \cdot A \cdot \Omega \cdot \frac{D}{\gamma - 1} \cdot \left(E_L^{1-\gamma} - E_H^{1-\gamma} \right) = C \cdot n_{trig}$$

where A is the area around the telescope position over which showers are simulated, Ω is the solid angle of a cone of half angle 2°, D and γ are species dependent parameters, see table 6.2. The number of simulated shower samples generated for each cosmic ray species n_{shower} has been chosen such that the constant C in the above expression is the same for each cosmic ray species. This allows direct summing of the triggered events to simulate the results from a spectrum of the correct mixed composition.

Given the number of simulated shower samples generated (i.e. 20 times the number of showers simulated; 264,460 protons, 159,300 alphas, 132,500 Oxygen group and 61,040 Iron group), and the average rate of triggers observed by the Mk6 telescope between 25° and 35° zenith in the off source segments of the PKS 2155 data set (8 events s^{-1}, averaged over 30 off source data segments each 14 minutes long), the constant C has the value 2.34×10^{-3} s^{-1}. This means that to match the observed cosmic ray rate of 8 events s^{-1} around 3,400 simulated events should be seen to trigger within the SOLMK simulations.

Attempts have been made to match both the event rate and the image distributions, though it has not been possible to accurately match the image distributions with the required number of simulated triggers. The lowest number of triggers which can be attained and still match the image distributions is ~4,150 events (i.e. 9.2 events s^{-1}), see table 6.5 for the species dependent triggering ratios. Any further increase in the trigger threshold, required to lower the number of event triggers, introduced discrepancies in the image parameter distributions which we were unable to correct for by altering the other telescope simulation parameters.

The essential problem arises from the increase in the trigger threshold needed to reduce the trigger rate, this had a tendency to increase the mean size of events which triggered the telescope. To compensate for this the PSF needed to be reduced to decrease the mean image size, this in turn had a tendency to increase the trigger rate. There was in effect a minimum number of events triggering, whilst still preserving the match between simulated image parameter distributions and the observed distributions. This minimum in the simulated number of triggers lay about 20% above the number of triggers required to match the observed cosmic ray trigger rate. Having said this, it is interesting to note that the cosmic ray flux derived by Wiebel B (1994) from a large selection of cosmic ray observations is some 16% lower than the Mohanty et al (1998) spectra at 1TeV, after allowing for differences in binning of cosmic ray species and the triggering proportions of these species, see table 6.7. To a first approximation, if the Wiebel (1994) spectra had been used for these simulations utilising the same telescope model and parameters, the simulated number of cosmic ray events would be expected to be in good agreement with the observed rate.

Cosmic ray Species	Number Triggered	Fraction of Total Triggers
Proton	2881	0.695
Alpha	855	0.206
Oxygen Group	332	0.079
Iron Group	87	~0.02

Table 6.5 The species dependent numbers and fractions of triggers in the simulated data set.

Species	Cosmic ray Flux at 1 TeV $m^2s^{-1}sr^{-1}TeV^{-1}$ Mohanty (1998)	Wiebel (1994)	Mohanty (1998)/Wiebel (1994)	Trigger Fraction	Weighted Diference over all Species at 1 TeV
Proton	0.1244	0.1091	1.14	0.695	1.156
Alpha	0.0773	0.0660	1.17	0.206	
Oxygen group	0.0655	0.0286, 0.0236] 0.0522	1.25	0.079	
Iron Group	0.0303	0.0252	1.20	~0.02	

Table 6.7 A comparison of two equally valid cosmic ray spectra at 1 TeV.

6.3.3 Background image parameter distributions

Simulations of cosmic rays were conducted at a zenith angle of 30 degrees to match both the rate and the image shape distributions (see section 4.3.3) seen in the real off source cosmic ray observations in the PKS 2155 data set between 25 and 35 degrees zenith angle. Doing this provided the model dependent parameters, given in table 6.8, which were used to adequately simulate the parameter distributions expected from gamma-ray induced EAS, see figure 6.8 a&b. There are a total of 30 off source segments of data in the PKS 2155 data set used by Chadwick (1999a) and (1999b), having an average zenith angle between 25 and 35 degrees. They contain a total of 203,602 cosmic ray events, representing around one fifth of the total background data set below 45°. This sub set of the data is shown in figures 6.5 a&b to be representative of the total background data set between 0° and 45° zenith.

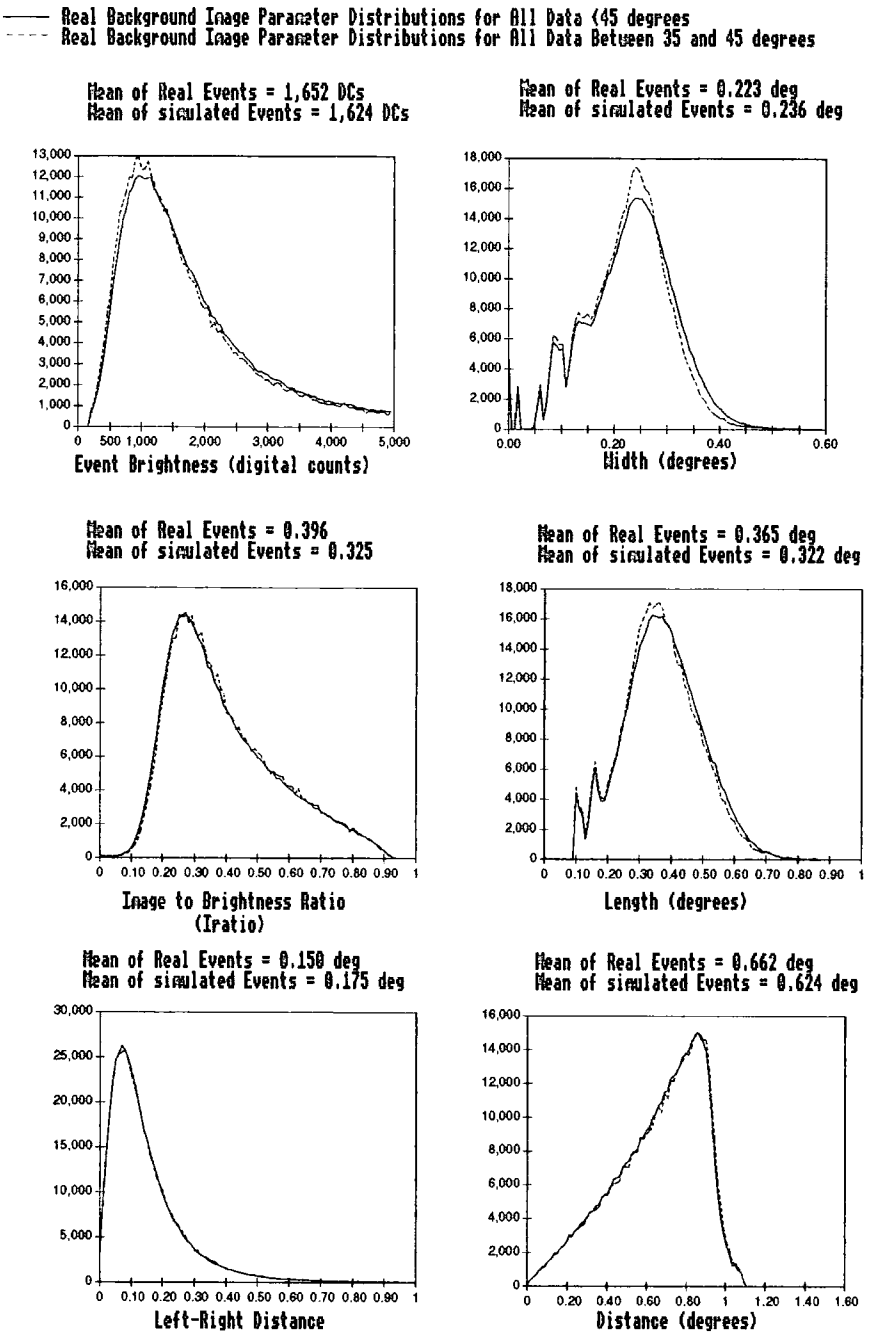

Figure 6.6a The observed difference in image parameter distributions between off source cosmic ray observations taken between 25 and 35 degrees zenith and at all zenith angles below 45 degrees. These graphs have been normalised such that both curves have the same area.

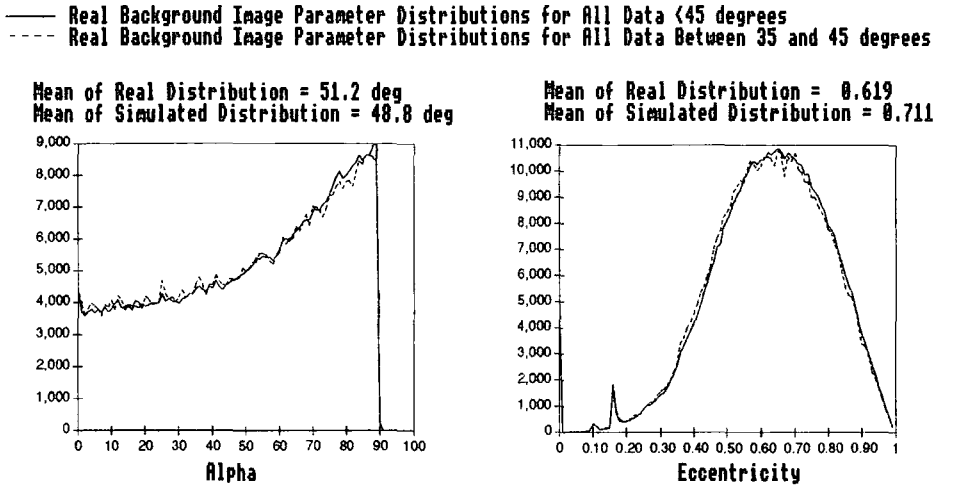

Figure 6.6b The observed difference in image parameter distributions between off source cosmic ray observations taken between 25 and 35 degrees zenith and at all zenith angles below 45 degrees. These graphs have been normalised such that both curves have the same area.

IACT model dependent parameter values have been derived such that both the rate of simulated cosmic ray events triggering the Mk6 IACT and their image parameter distributions are a reasonable match to those observed in the off source PKS 2155 data. A comparison of the parameter distributions for both real and simulated cosmic ray events using the values given in table 6.8 are shown in figures 6.7 a&b.

Simulation Parameter	Value Chosen
Discriminator Level	0.43
Point Spread Function	$0.20^{\circ}0.47^{\circ}66\%$
Digital Counts per Photoelectron	4.5
Sky Noise Factor	0.30
Guard Ring Sensitivity	0.58
Left-Right Sensitivity	0.31

Table 6.8 The model dependent simulation parameters used to obtain the best simulated fits to the real image parameter distributions, for off source background cosmic ray events observed between 25 and 35 degrees zenith.

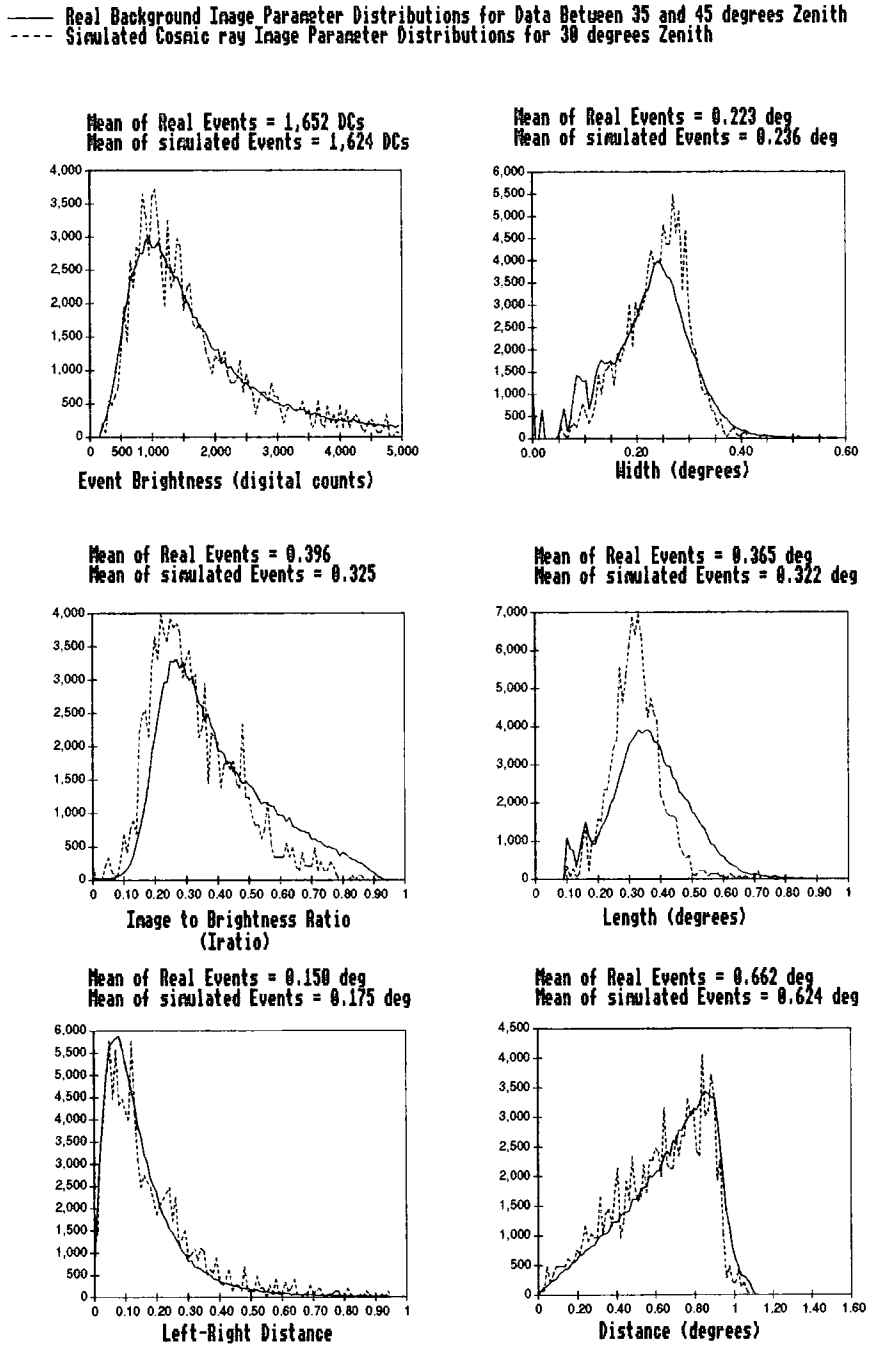

Figure 6.7a The difference in image parameter distributions between off source cosmic ray observations taken between 25 and 35 degrees zenith and cosmic ray events simulated at 30 degrees zenith an 180 degrees azimuth. These graphs have been normalised such that both curves have the same area.

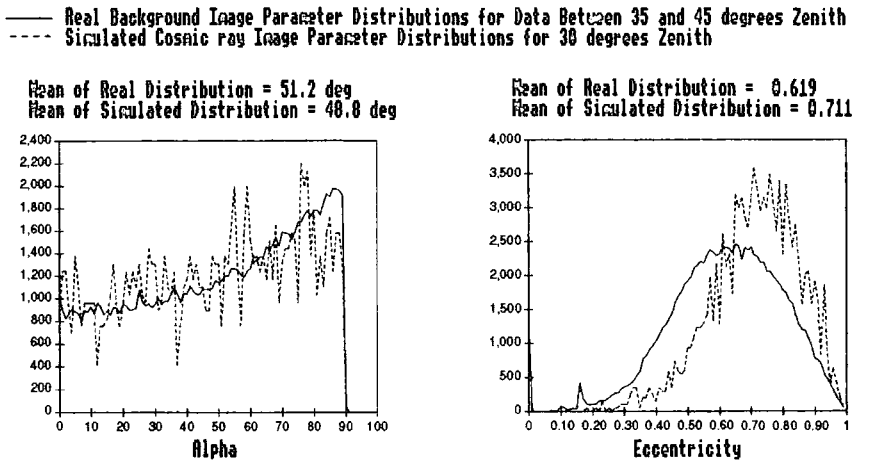

Figure 6.7b The difference in image parameter distributions between off source cosmic ray observations taken between 25 and 35 degrees zenith and cosmic ray events simulated at 30 degrees zenith an 180 degrees azimuth. These graphs have been normalised such that both curves have the same area.

6.3.4 The disparity in the length and iratio distributions

As can be seen from the parameter distributions of the real and simulated cosmic ray images given in figures 6.7 a&b, there is a significant disparity in the simulated *length* and, to a lesser extent, the simulated Iratio distributions compared to the observed distributions. When one looks at real event images which have large values of *length* it is apparent that a significant minority of these events are composed of two distinct regions of Cherenkov light within the camera. The event parameterisation procedure used with Mk6 data (see section 4.3.3) will simply represent this image information as one long event conjoining two separate regions of Cherenkov signal within the camera, these types of event do not appear to be well simulated by the MOCCA and SOLMK Monte Carlo simulation program combination. This may be due to poor simulation within MOCCA of the sub structure of cosmic ray showers developing at low altitudes. The long events seen in the real observations of cosmic

ray showers could be due to Cherenkov light from local muons, though local muons by themselves do not trigger the Mk6 telescope, local muon light is likely to be present in cosmic ray shower images. Alternatively, the disparity could be the result of poor simulation of the flat fielding procedure used for observed data, which is not followed in detail within SOLMK. It is simply assumed that the flat fielding procedure used for observed data will eliminate any significant sources of systematic bias. Though the selection of PMTs which contribute to the image parameterisation procedure is dependent upon the individual noise level in each tube, it is therefore possible that assuming all the central camera PMTs can be represented by one common noise level is too simplistic an assumption, the result of which may be the poor simulation of long and relatively diffuse images.

If the disparity in the observed *length* distributions of cosmic ray induced event images were the result of poor simulation of their subshower structure it would be reasonable to assume that this would not be reflected in the gamma-ray simulations. However, if this disparity is due to poor simulation of noise in the central camera there may be a systematic bias which would follow through into the gamma-ray simulations. The result would be an underestimate of the number of gamma-rays retained due to the range of eccentricity values used to select gamma-rays during analysis.

The slight disparity between real and simulated cosmic ray events in their Iratio distributions is likely to be related to the disparity in their length distributions. The majority of observed cosmic ray images with long lengths are due to the conjoining

of two distinct regions of Cherenkov signal. This results in higher values of Iratio (high concentration relates to low values of Iratio, see section 4.3.3), as for a given event size the Cherenkov signal selected for image parameterisation will be concentrated in two small regions of the camera rather than selected across the whole length of the event.

6.4 Simulated gamma-ray image parameter distributions

Given the results of the previous few sections it was concluded that the simulations of the background cosmic ray distributions were sufficient to allow confidence in the accuracy of gamma-ray image parameter distributions simulated using MOCCA and SOLMK. These distributions are shown compared against real background cosmic rays in figures 6.8 a&b.

For the purposes of determining the flux and spectral index of PKS2155, derived using the Chadwick et al. (1999a) and (1999c) parameter selection, the data in figures 6.8 a&b were divided into five image size bins, the number of events in each bin was used to derive the integral flux some estimation of the spectral index of gamma-rays from PKS 2155-304, and the threshold level for detection of the Durham Mk6 IACT.

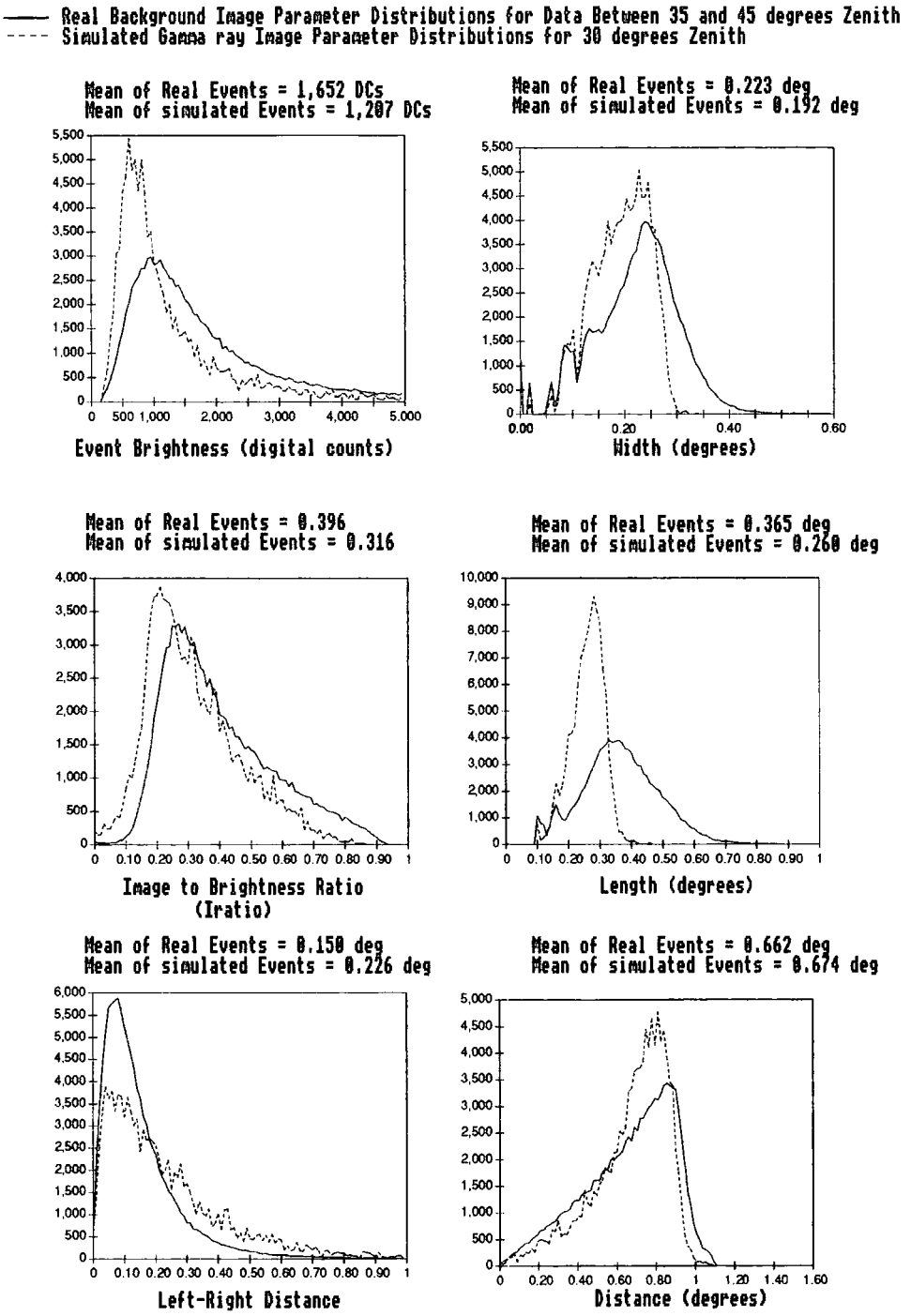

Figure 6.8a The difference in image parameter distributions between off source cosmic ray observations taken between 25 and 35 degrees zenith and simulated gamma-ray events simulated at 30 degrees zenith and 180 degrees azimuth.

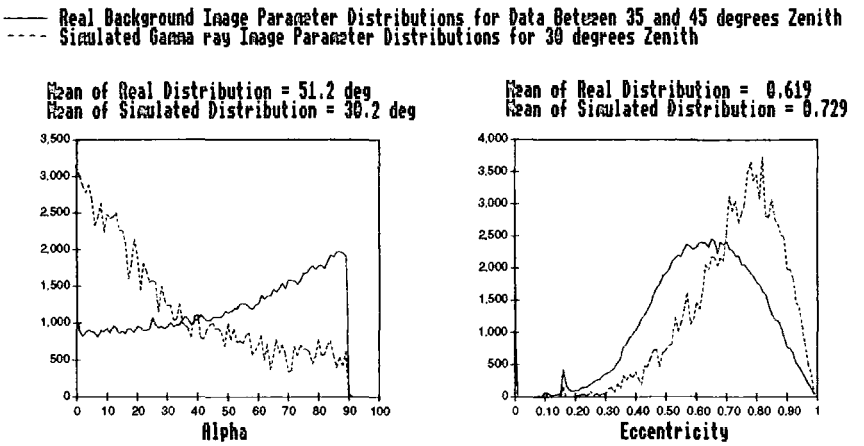

Figure 6.8b The difference in image parameter distributions between off source cosmic ray observations taken between 25 and 35 degrees zenith and simulated gamma-ray events simulated at 30 degrees zenith an 180 degrees azimuth.

6.5 Determining the flux of PKS 2155-304

A VHE gamma-ray signal from the close X-ray selected BL Lac PKS 2155-304 was detected during the observing seasons of 1996 and 1997 (see section 6.5.1). For zenith angles less than 45° a total of 544±99 excess gamma-ray events were observed on source in 32.5 hours of observation. In order to determine the flux of PKS 2155-304, the image parameter selection criteria used in Chadwick et al. (1999b) and (1999c) were applied to this simulated data set of 750,000 simulated gamma-ray images produced at a zenith angle of 30 degrees. This was done using the same shower and telescope simulation models as for the images of nucleonic induced showers, as was discussed in sections 6.2 and 6.3. The number of residual gamma-ray images retained after application of the Chadwick et al. (1999b) and (1999c) parameter selection criteria is shown grouped by image size bin and VHE gamma-ray energy in table 6.9. The on source excess observed in each image size bin is given in

table 6.10. It is apparent from the number of simulated gamma-rays selected by these selection criteria that only the top two image size bins, 1,500 to 2,000 DCs and 2,000 to 10,000 DCs, (from now on referred to as bins 4 and 5 respectively), contained enough events to provide reasonable statistics. Hence from this time onwards comment will be reserved to a discussion regarding bins 4 & 5.

Image Brightness Bins (digital counts)

Energy Bins (GeV)	500-800	800-1,200	1,200-1,500	1,500-2,000	2,000-10,000	500 - 10,000
300 to400	0	0				0
400 to 500	2	1	0	0		0
500 to 700	3	0	1	1		5
700 to 1,000	5	15	2	4	1	27
1,000 to 1,500	3	3	12	44	9	71
1,500 to 2,000	0	0	8	126	56	190
2,000 to 3,000			0	54	212	266
3,000 to 4,000				0	159	159
4,000 to 5,000					96	96
5,000 to 7,000					106	106
7,000 to 10,000					36	36
10,000 to 15,000					0	0
15,000 to 20,000						
All Energies	13	19	23	229	675	959

Table 6.9 Tabulated results of the number of simulated gamma-ray images per size and energy bin that survive the selection procedure used by Chadwick et al. (1999a) and (1999c) in the detection of PKS 2155-304.

6.5.1 The observed data

The data used in this thesis is a sub set (i.e. observations made at zenith angles less than 45°) of that published in Chadwick et al. (1999b) and (1999c). Observations of PKS 2155-304 were made during 1996 September/October/November and 1997 October/November using the Mk6 telescope (see chapter 4) under conditions of moonless, clear skies. A total of 156 on source segments was observed (along with their corresponding off source comparison segments), 130 of which where observed below 45° zenith, giving a total of 109,200 seconds of on-source observation. The image parameter selection applied to the PKS 2155-304 data recorded at zenith angles less than 45° is summarized in table 4.2. They constitute a standard set of criteria developed to include an allowance for the variation of parameters with event size and are routinely applied to data from all dark-field objects recorded at zenith angles less than 45°. The number of excess on source events remaining after application of the selections described above are shown in table 6.10.

Size Bin	Number of Excess events
Bin 1	29+/-22
Bin 2	74+/-28
Bin 3	83+/-31
Bin 4	138+/-57
Bin 5	220+/-65
Total	544+/-99

Table 6.10: Number of excess events in various image size bins for 130 on source segments observed below 45° zenith. The errors have been calculated from the number of background events in both the on and off source fields.

In this data set there is an excess of events at small alpha, the expected gamma-ray domain, and imposing a selection of alpha 22.5° yields a gamma-ray detection significance at the 6.8 σ level for the total data set, and a significance at the 5.5 σ level for data observed below 45° zenith.

As can be seen from table 6.9, significant numbers of simulated gamma-rays are retained, after the application of the image selection criteria shown in table 4.2, only in image size bins 4 and 5. The numbers of events in bins 1, 2 and 3 were found to be very sensitive to small variations in the model dependent simulation parameters and were thus viewed to be unreliable. Analysis was continued using only image size bins 4 and 5. The number of excess events observed within these bins, below alpha of 22.5°, are 138±57 and 220±65 respectively (see table 6.10); this combined excess yields a gamma-ray detection significance at the 4.1 σ level.

6.5.2 Method for calculation of flux values

Firstly, the number of simulated gamma-ray images retained in size bins 4 and 5 after application of the parameter selections given in table 4.2 was determined. These were then converted, as a function of energy, into fractions of the number of gamma-ray samples simulated. Table 4.2 gives the tabulated fractional retention factor f(E) for these bins as a function of energy.

Secondly, each $f(E)_i$ (were i represents the bin number i.e. either 4 or 5) is folded with a trial spectrum of the form $E^{-\gamma}$ and integrated over the energy range for which gamma-ray simulations have been made, to derive $F(\gamma)_i$.

$$F(\gamma)_i = \int_{0.1TeV}^{30TeV} f(E)_i \, E^{-\gamma} \, dE$$

The spectral index that best fits with the observed data is found when $F(\gamma)_i$ divided by the number of excess events observed in size bin N_i is the same within error for each bin, i.e.

$$\frac{F(\gamma)_i}{E_i} = \frac{F(\gamma)_{i+1}}{E_{i+1}} \ldots = \frac{F(\gamma)_{i+n}}{E_{i+n}}$$

Alternatively, this analysis will only be dealing with two image size bins (i.e. bins 4 and 5) and this can be represented in a simplified form,

$$\frac{N_4}{N_5} = \frac{F(\gamma)_4}{F(\gamma)_5}$$

All that is now required is to find the range of γ values which satisfies this equation, given the errors on the observed on source excess and in the simulations, see section 6.5.3.

To reduce the systematic errors incurred in deriving $F(\gamma)_i$, due to binning over relatively large energy intervals, a curve is drawn over the histogrammed data for f(E) to provide a tabulated function into which is folded spectra of the form $E^{-\gamma}$. A numerical integration has then been performed over this curve to derive a value for $F(\gamma)$, see section 6.5.4.

Finally, the integral flux $S_\gamma(E_{th})$ above a threshold energy E_{th}(TeV) for a differential index γ is found using the following expression,

$$S_\gamma(E_{th}) = \frac{N}{T} \frac{E_{th}^{-(\gamma-1)}}{\gamma - 1} \left[A \sum_{i=1}^{n} F(\gamma)_i \right]^{-1}$$

Where N is the number of excess on source events; T is the time of observation; A is the target area for the simulated showers, π x $(300)^2 = 2.827$ x 10^5 m^2; and F(E) is the integral over all gamma-ray energies of the fraction of gamma-ray showers of energy E falling on the target area, which trigger the telescope, and whose Cherenkov images survive the image size bin dependent selection criteria. See figure 6.8 for more details.

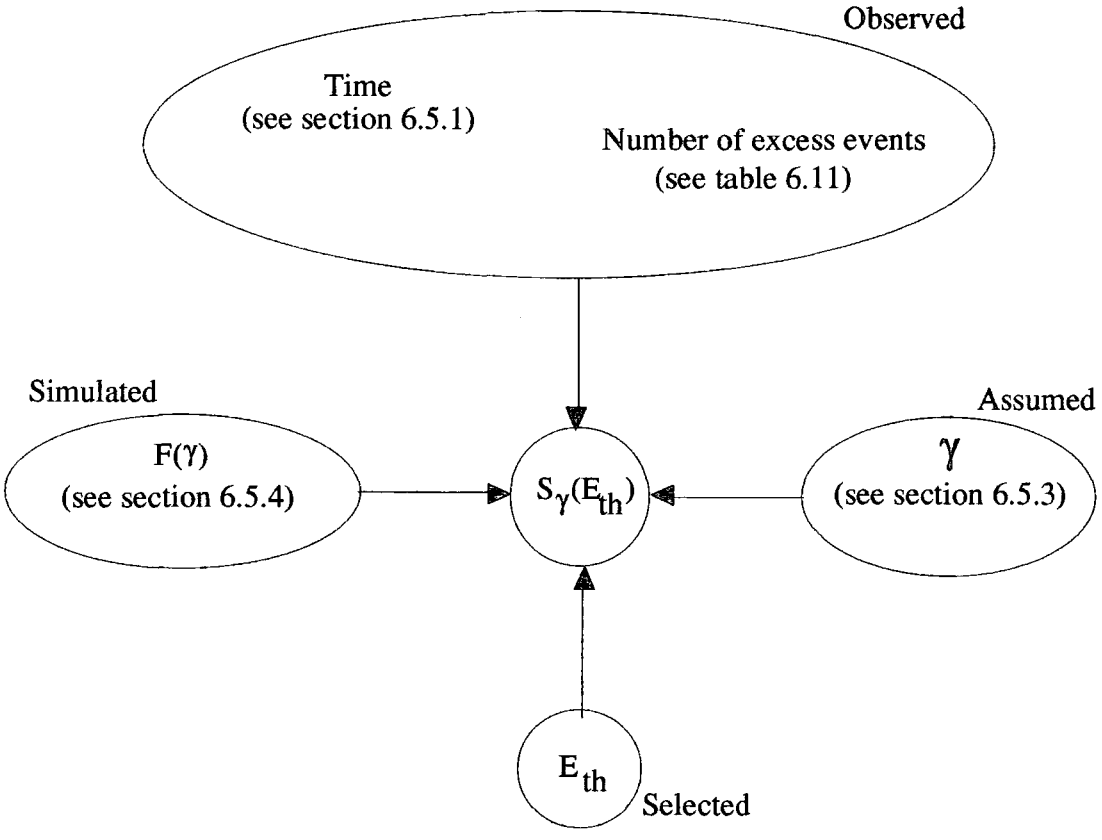

Figure 6.9: A guide to the factors which contribute to the flux $S_\gamma(E_{th})$ above a threshold value of E_{th}.

6.5.3 Spectral index

A plot of the differential spectral index γ verses the percentage difference between the ratios of observed excess in bins 4 and 5 (N_4=138±57 and N_5=220±65) and the ratio of $F(\gamma)_4$ and $F(\gamma)_5$ is given in figure 6.8. It can be seen that the errors on the observed excess in bins 4 and 5 are too large to significantly constrain the range of possible spectral indices for our observation of PKS 2155-304. All that can be said with reasonable confidence is that our observations suggest that the observed spectral index of PKS 2155-304 is likely to be steeper than about 2 and no steeper than about 7. This is not very constraining. To calculate the flux from PKS 2155-304, the assumption has been made that the differential spectral index will be similar to that used to fit the spectrum of Mkn501, the actual value for γ that we have used is 2.6, which is simmilar to that of Mkn501 (Aharonian et al (1999), Samuelson (1998), Krennrich (1999)).

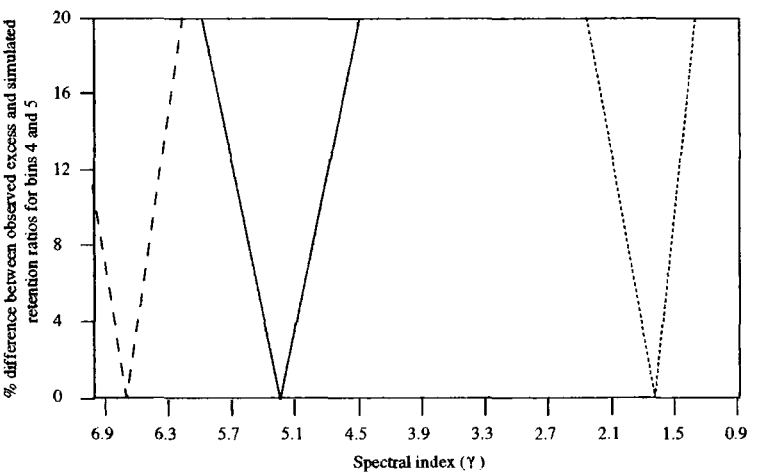

Figure 6.10: The spectral index of PKS 2155-304 as determined from the observations of Chadwick et al. (1999b) and (1999c) and the gamma-ray simulations conducted for this thesis. The point at which the solid line reaches zero on the Y-axis marks the spectral index value that equalises the ratio between simulated gamma-rays in bins 4 and 5 and the observed excess in bins 4 and 5, this gives the most likely value for the spectral index as measured on the X-axis. The dotted and dashed lines are the 1σ limits on this result.

6.5.4 The flux for PKS 2155-304

The number of simulated gamma-rays which were retained by the Chadwick et al. (1999b) and (1999c) image parameter selections were summed over brightness bins 4 and 5 (i.e. from 1,500 to 10,000 DCs). The resultant numbers of gamma-rays binned and then expressed as a fraction of the number simulated over the area used in the simulations, see table 6.9.

Energy Bin (TeV)	Number Simulated	Number Selected		Ratio f(E) Selected / Simulated	
		Bin 4	Bin 5	Bin 4	Bin 5
0.1 to 0.3	580,510	0	0	0.00000	0.00000
0.3 to 0.4	53,830	0	0	0.00000	0.00000
0.4 to 0.5	28,775	0	0	0.00000	0.00000
0.5 to 0.7	29,690	1	0	0.00003	0.00000
0.7 to 1.0	19,700	4	1	0.00020	0.00005
1.0 to 1.5	12,885	44	9	0.00341	0.00070
1.5 to 2.0	5,465	126	56	0.02306	0.01025
2.0 to 3.0	4,760	54	212	0.01134	0.04454
3.0 to 4.0	2,130	0	159	0.00000	0.07465
4.0 to 5.0	1,155	0	96	0.00000	0.08312
5.0 to 7.0	1,255	0	106	0.00000	0.08446
7.0 to 10.0	695	0	36	0.00000	0.05180
10.0 to 15.0	465	0	0	0.00000	0.00000
15.0 to 20.0	195	0	0	0.00000	0.00000
20.0 to 30.0	210	0	0	0.00000	0.00000

Table 6.9: The ratios of the number of simulated gamma-ray images retained by the selection criteria shown in table 4.2 to the number of gamma-rays falling within the area over which simulations where made (in this case this is a circle 300m in radius), as a function of energy for image size bins 4 and 5.

Combining the fractional values for bins 4 and 5 in table 4.2 gave the histogram shown in figure 6.9. A curve was drawn through the peaks of each bin and an interpolated set of f(E) values as a function of E was computed, see table 6.10. The

tabulated function f(E) was then folded with the assumed source spectrum of $E^{-2.6}$, and $F(\gamma)$ was determined by numerical integration using the tabulated values for f(E) . $E^{-2.6}$. The curve of f(E) . $E^{-2.6}$ verses energy is shown in figure 6.10.

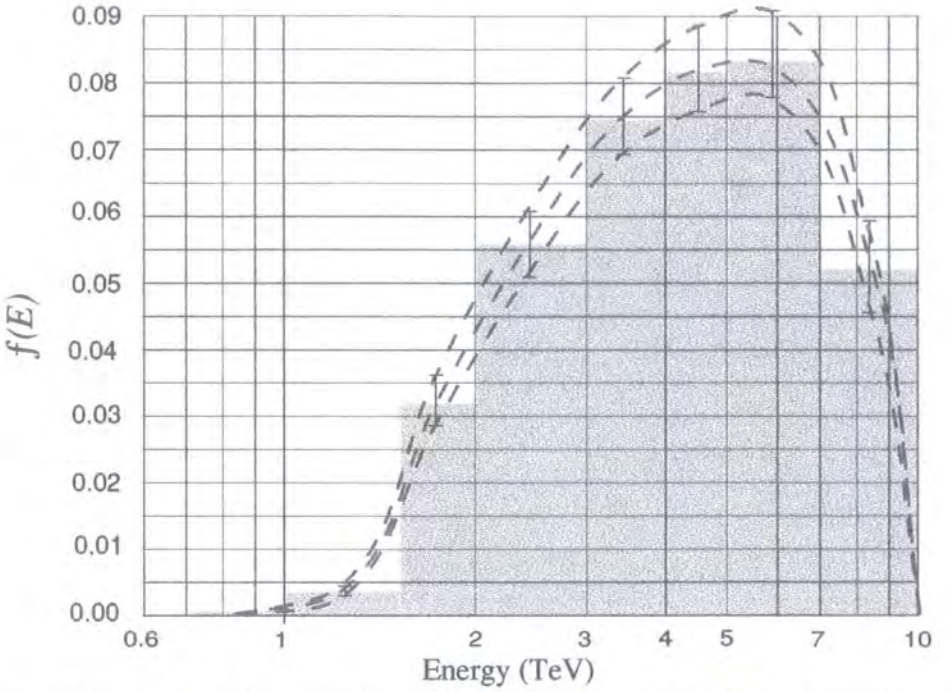

Figure 6.11: The form of the fractional trigger spectrum. Interpolated values for f(E) where taken from this figure and folded with a spectrum of the form $E^{-2.6}$ to derive the trigger spectrum $F(\gamma)$ for our simulations.

Energy Bin (TeV)	Tabulated f(E)	$f(E) \cdot E^{-2.6}$
0.8	0	0
0.9	0.0005	0.0007
1.0	0.0011	0.0011
1.5	0.0044	0.0015
2.0	0.0436	0.0072
2.5	0.0562	0.0052
3.0	0.0698	0.0040
3.5	0.0753	0.0029
4.0	0.0796	0.0022
5.0	0.0835	0.0013
6.0	0.0840	0.0008
7.0	0.0753	0.0005
8.0	0.0600	0.0003
9.0	0.0398	0.0001
10.0	0	0

Table 6.10: The tabulated form of the trigger spectrum for our simulations and for a differential source energy spectrum of index, $\gamma = 2.6$.

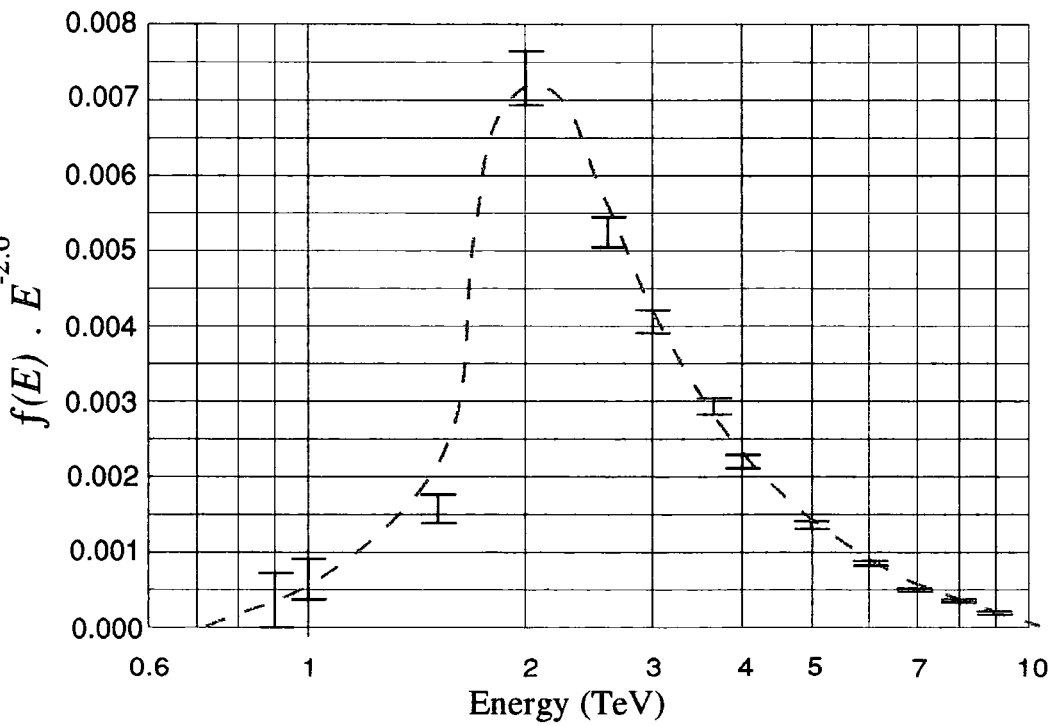

Figure 6.12: The form of the energy dependent triggering responce of the Durham Mk6 IACT to simulated VHE gamma-rays.

The result of this was a value for F(2.6) = 0.015±0.002. Hence, the flux of gamma-rays above 1.5 TeV from the AGN PKS2155 was found to be,

$$2.5 \times 10^{-7} \text{ photons } m^{-2} s^{-1}$$

6.6 Statistical and systematic errors

The value for the flux from PKS 2155-304 found in section 6.5.4 will certainly have a significant contribution from statistical and systematic errors in the observed and simulated data. Statistical errors are relatively trivial to calculate given that all one needs to do is propagate the known 1σ Poissonian errors on the numbers of observed and simulated events through the appropriate equations and procedures, whilst always erring on the side of caution when it comes to making choices on how to plot curves, tabulate functions and in numerical integrations. Systematic errors on the other hand are notoriously difficult to determine as they often contain many contributing factors, the relative effects of which may be unknown.

6.6.1 Statistical error

The major contributor to the statistical error comes from the observed error on the number of excess events in bins 4 and 5, i.e. 358±87 events, though there will be a small statistical error on F(γ) introduced by the error on the number of simulated events surviving the selection criteria in bins 4 and 5 as a function of energy, i.e. ΔF(γ) = 0.002. This value for ΔF(γ) will be a slight overestimate of the 1σ error on F(γ) as they have been calculated using a tabulated Δf(E) as a function of energy derived from the two dotted curves in figure 6.9, these were drawn through the 1σ

error limits of each calculated value of f(E) in each energy bin. Propagating both these sources of error to find $\Delta S_{-2.6}(1.5\text{TeV})$ gives a value for the statistical error on the flux for PKS 2155-304 of,

$$\Delta_{statistical}\left[S_{-2.6}(1.5TeV)\right] = 0.7 \times 10^{-7}\ photons\ m^{-2}\ s^{-1}$$

6.6.2 Systematic error (atmospheric stability and count rate)

Over the wavelengths relevant for observations of Cherenkov photons, atmospheric variability is likely to be a significant source of systematic error. Relevant contributors to extinction are: Rayleigh scattering, Ozone absorption and aerosol scattering. Rayleigh scattering is the dominant mechanism and is governed by the column density of the atmosphere above the telescope, which is in turn related to barometric pressure. Although the majority of ozone in the atmosphere is located above shower maximum (roughly 7km), ozone extinction will still be significant at lower altitudes and will reduce transmission for wavelengths below about 300nm. In addition to this the atmospheric profile of ozone varies on a seasonal basis. Aerosols are mainly located at low altitudes with a scale height of roughly 1km (Jursa, 1985), the local concentrations of which are also highly variable.

These factors may go some way to explaining the variability in background count rate observed by the Mk6 telescope, even though the observations were made under apparently clear and stable atmospheric conditions. Variations of around ±10% are seen in the background count rate at a given zenith angle for observations taken on consecutive nights under apparently similar conditions. Considering that the Mk6

telescope is situated at an altitude of 260m ASL it is likely that the local aerosol concentration will have a strong effect on the observed count rate. This may go some way to explaining the data segments with anomalous low count rates which sometimes appear in the observed data, see figures 6.3 and 6.5.

6.6.3 Systematic error (SOLMK input parameters)

In the course of this study into the sensitivity of the Durham Mk6 IACT, the image parameters of the observed background cosmic ray events were matched using a different set of SOLMK input parameters from those used throughout this thesis. In this alternative case the cosmic ray trigger rate at 30° zenith angle was held at 10.7 events s^{-1}, a rate corresponding to the average of a larger data set than that used to derive the SOLMK input parameter set shown in figure table 6.8. In order to best match the observed width distribution, a broader PSF (near to the limit of that allowed by measurement) was adopted. This alternative parameter set is given in table 6.13. When these input parameters were used to derive the sensitivity of the Mk6 telescope to VHE gamma-rays and in turn the flux for PKS 2155-304 above 1.5TeV, the resultant value was about 15% higher than the value derived in section 6.5.4. This suggests that the systematic error due to the sensitivity of the final flux value to the precise nature of the input parameters is likely to be around 15%.

Simulation Parameter	Value Chosen
Discriminator Level	0.35
Point Spread Function	0.25°,0.45°,66%
Digital Counts per Photoelectron	4.5
Sky Noise Factor	0.25
Guard Ring Sensitivity	0.40
Left-Right Sensitivity	0.30

Table 6.13: An alternative set of model dependent simulation parameters used to obtain the best simulated fits to real image parameter distributions. A different data set of background cosmic ray events than that which has been used so far, observed between 25 and 35 degrees zenith.

6.6.4 Insights from CORSIKA and ALTAI

The effect of using Corsika or ALTAI shower simulation codes on the value of the sensitivity of the Mk6 IACT has been investigated by two other members of the Durham VHE gamma-ray group, S. J. Nolan and J. L. Osborne. Their radial distance versus Cherenkov photon yield plots show that ALTAI predicts slightly more (<10%) light from both hadronic and gamma-ray showers than does MOCCA, see figures 6.10 and 6.11 respectively. Because of the way we normalise to the observed hadronic shower trigger rate these two discrepancies compensate and the derived fluxes are little affected by the use of either one or the other of the codes. For CORSIKA the radial distributions show good agreement with MOCCA for the gamma-ray showers but a significant (~20%) lowering of the light from hadronic showers. Detailed simulations show that in order to simultaneously match the trigger rate for hadronic showers and the mean brightness of the images, the dc/pe ratio would have to be increased from 4.5 to 6.0. Such a value can not be excluded but it would be higher

than direct measurements have suggested. The trigger probability of the gamma-ray showers would be correspondingly increased and this would result in a reduction of the measured flux from a given source by a factor of 0.6.

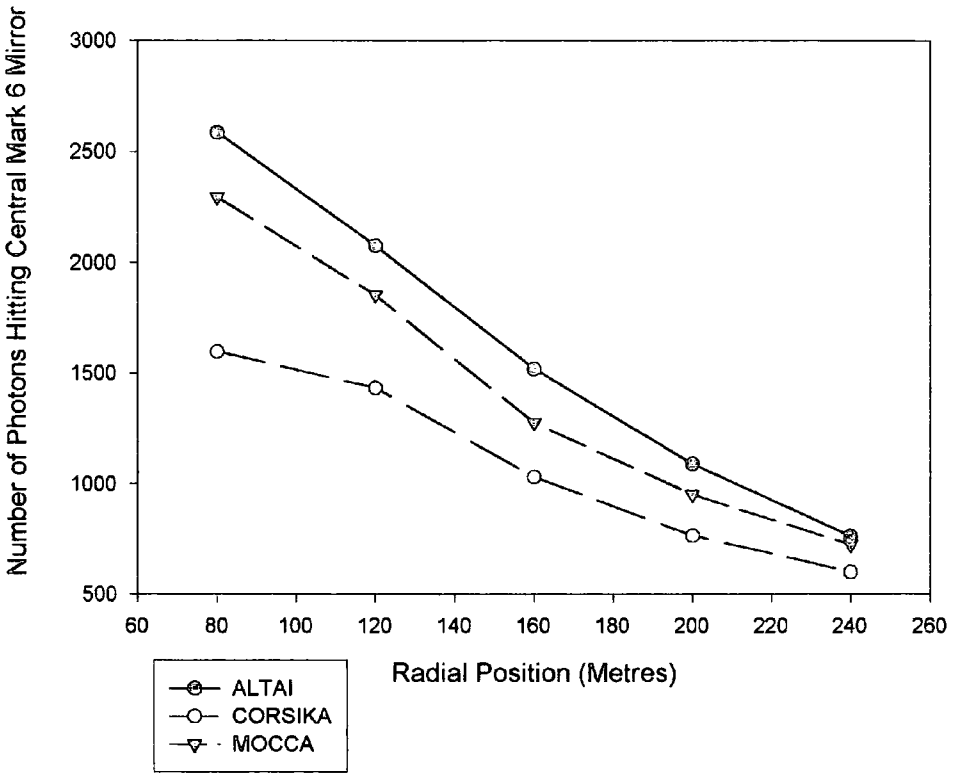

Figure 6.13: Plot of mean number of photons hitting a central Mark 6 mirror, with atmospheric absorption, for a US standard atmospheric profile at an altitude of 1800 meters for a 1TeV proton primary for ALTAI, CORSIKA and MOCCA at fixed radial distances. S. J. Nolan and J. L. Osborne (personal communication).

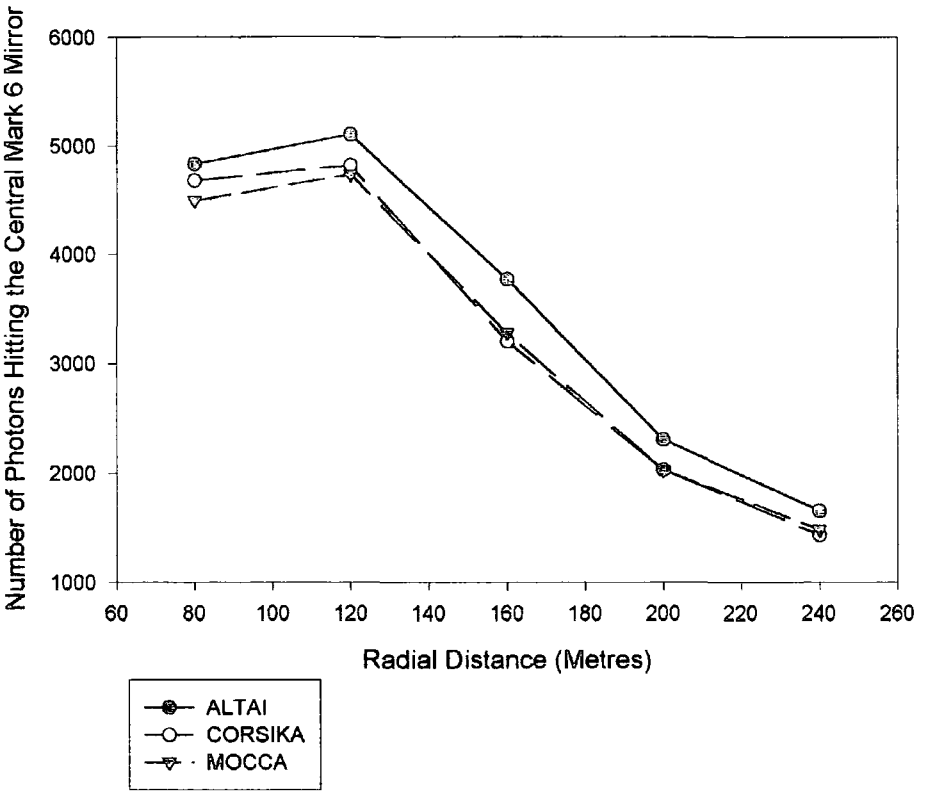

Figure 6.14: Plot of mean number of photons hitting a central Mark 6 mirror, with atmospheric absorption, for a US standard atmospheric profile at an altitude of 1800 meters for a 1TeV gamma-ray primary for ALTAI, CORSIKA and MOCCA at fixed radial distances. S. J. Nolan and J. L. Osborne (personal communication).

6.6.5 Combined systematic error

Combining the effects of the main contributors to the systematic error on the result given in section 6.5.4 results in asymmetric error bars. The 10% contribution from atmospheric variability must be considered as 10% in either direction, as should the systematic error due to differing SOLMK input parameters (i.e. 15%). However, the possible error due to the effects of utilising different shower simulation programs would be best interpreted as a systematic in one direction only. The ALTAI simulation code agrees quite well with MOCCA, although CORSIKA suggests a value 60%

lower than the flux predicted using MOCCA shower simulations. The complte sytematic error on the result for the flux of PKS 2155-304 is then,

$$+\Delta_{systematic}\,[S_{-2.6}(1.5TeV)] = 0.5 \times 10^{-7}\ photons\ m^{-2}\ s^{-1}$$

$$-\Delta_{systematic}\,[S_{-2.6}(1.5TeV)] = 1.6 \times 10^{-7}\ photons\ m^{-2}\ s^{-1}$$

6.7 Conclusion

After considering all the main factors concerning the statistical variables discussed in section 6.6, that effect the reliability of the result reached in section 6.5.4, the resultant flux from PKS 2155-304 including all significant error contributions was found to be,

$$S_{-2.6}(1.5TeV) = 2.5 \pm 0.7_{stat} \frac{+\ 0.5}{-\ 1.6}sys \times 10^{-7}\ photons\ m^{-2}\ s^{-1}$$

For the purposes of comparison this result was converted into erg cm^{-2} s^{-1} and shown on a plot of the spectral energy distribution (SED) for PKS 2155-304, see figure 6.15. The value plotted at 1.5TeV (i.e. 3.63 x 10^{26} Hz) is,

$$9.6 \pm 2.7_{stat} \frac{+\ 1.9}{-\ 6.1}sys \times 10^{-11}\ erg\ cm^{-2}\ s^{-1}$$

The optical depth (ρ) to PKS 2155-304, which is the most distant AGN to be observed in TeV gamma-rays, at redshift of 0.12, is by the model of Stecker & de Jager (1997), $\rho_{(High\ IR)} = 2.27$; $\rho_{(Low\ IR)} = 1.35$, for 1.5 TeV gamma-rays, where 'High IR' and 'Low IR' represent the extremes of the expected flux density of the intervening inter-galactic infra-red radiation field. These optical depths for the AGN PKS 2155-304 relate to an opacity of between 75% and 90%. This would lift somewhat the 1.5 TeV gamma-ray point plotted in figure 6.15, as the SSC model of Tavecchio et al (1998) (*curves*) takes no account of possible sources of opacity.

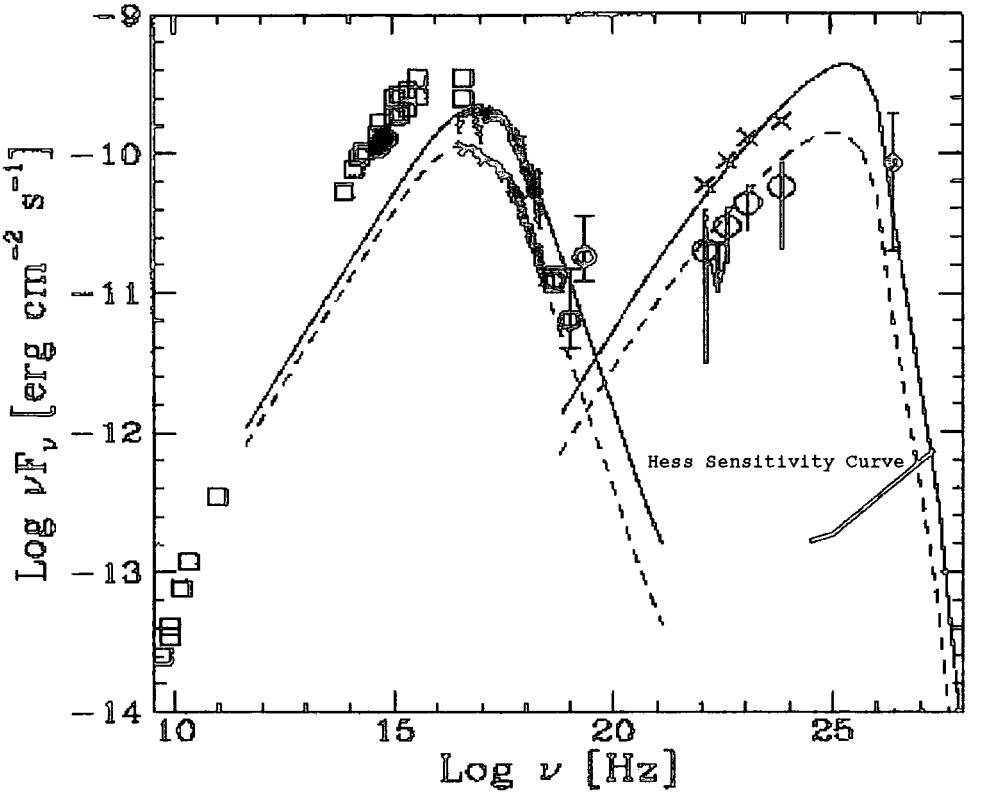

Figure 6.15: Spectral Energy Distribution (SED) of PKS 2155-304 taken from Maraschi et al (1998). The TeV flux given in this thesis (*filled diamond*) has been superimposed, the TeV data set used contains November 1997 observations of PKS 2155-304, which comenced on the 17th, several days after the observation of high flux X-ray data and gamma-ray data (Chiappetti et al (1999) & Vestrand et al. (1999)). Maraschi et al (1998) fitted the SSC model (*curves*) of Tavecchio et al (1998) to a selection of spectral data. The radio and optical points (*squares*) (Courvoisier et al (1995) & Pesce et al (1997)) are an average of several observations made over an extended period. The UV points (*bars*) (Edelson et al. (1992), Urry et al. (1993) & Pian et al. (1997)) shows pre-1997 flare and non-flare data separately, and the BeppoSax X-ray points (*bold circles*) of Chiappetti et al (1999), taken in November 1997, contain mixed data with a significant proportion of flare data. The EGRET gamma-ray points Vestrand et al (1995) (*circles*) are also shown multiplied by a factor of three (*crosses*) to represent the gamma-ray state of PKS 2155-304 in November 1997 [as communicated in IAU circular (Sreekumar & Vestrand (1997)), and analysed in Vestrand et al. (1999)]. The simple seven parameter homogeneous SSC model of Tavecchio et al (1998) fitted by Maraschi et al (1998), is shown in the both the high (*solid curve*) and low (*dashed curve*) states.

CHAPTER SEVEN - Discussion

7.1 Introduction

Close X-ray selected BL Lac objects (XBLs) are sources of VHE gamma-rays at energies above several hundred GeV. The BL Lac first detected as a source of VHE gamma-rays was Mrk 421 (Punch et al. (1992)), following its discovery as a GeV source by the EGRET experiment on the Compton Gamma-Ray Observatory (Lin et al. (1992)). Mrk 421 has been extensively monitored in VHE gamma-rays and exhibits complex behaviour, having a low-level quiescent state with flaring on timescales as short as 30 minutes (Gaidos et al. (1996); Zweerink et al. (1997); Takahashi et al. (1998)). Another source of VHE gamma-rays is Mrk 501 (Quinn et al. (1996)), although not detected at GeV energies with EGRET, and also exhibits low-level emission with flaring (Catanese et al. (1997a)). In 1997, extremely strong outbursts of TeV emission were detected lasting several months (Deckers et al. (1997); Quinn et al. (1997); Hayashida et al. (1998)). The BL Lac 1ES 2344+514 also emits VHE gamma-rays, most of the evidence for emission comes from a single outburst (Catanese et al. (1997b & 1998)). All of these objects are close (z~0.03), X-ray-selected BL Lac objects. There have been no reported detections of VHE gamma-rays from radio-selected BL Lac objects although this category of objects is frequently detected at GeV energies by the EGRET experiment.

Stecker, de Jager and Salamon (1996) have interpreted the gamma-ray results in the GeV-TeV range and propose a model in which RBLs will be GeV gamma-ray sources

and XBLs will be TeV sources. They associate the emission of TeV gamma-rays from XBLs with the presence of relativistic electrons with energies higher than those in RBLs. They then go on to show that a simple synchrotron self-Compton model can explain the differences observed between RBLs and XBLs, provided the attenuation of the VHE gamma-ray flux by pair production with the inter-galactic infrared background is taken into account (Stecker, de Jager and Salamon (1992); Stecker and de Jager (1997)). On the basis of this model despite having a redshift of 0.117, PKS 2155-304 is predicted to be a strong TeV gamma-ray source.

The BL Lac PKS 2155-304, was discovered as an X-ray source during observations made with the HEAO 1 satellite (Schwartz et al. (1979); Griffiths (1979)) at a position where the Ariel V satellite had previously detected confused emission (Cooke et al. (1978)). In many ways, PKS 2155-304 may be regarded as the archetypal X-ray-selected BL Lac object; like most BL Lac objects it is associated with a compact, flat-spectrum radio source and has an almost featureless continuum that extends from radio to X-ray energies. It is the brightest known BL Lac at UV wavelengths and the object's maximum power is emitted between the UV and the soft X-ray range (Wandel and Urry (1991)). PKS 2155-304 has a history of rapid, strong broadband variability and has been the subject of several multiwavelength monitoring campaigns (see, e.g. Brinkmann et al. (1994); Courvoisier et al. (1995); Pesce et al. (1997)). The EGRET experiment on board the Compton Gamma-Ray Observatory was used to detect 30 MeV-10 GeV gamma-ray emission from PKS 2155-304 during 1994 November 15-29 (Vestrand, Stacy and Sreekumar (1995)). These observations indicated a very hard spectrum, with an integral power-law spectral index of 1.71 ±

0.24, and this, combined with its proximity, makes it an excellent candidate TeV source. In 1997 November, contemporaneous with some of the observations reported here, X-ray emission was detected with the BeppoSAX satellite (Chiappetti and Torroni 1997) with a flux equal to the strongest previous outburst. The flux derived in chapter six can be understood if PKS 2155-304 was in a high state of emission, which is consistent with the BeppoSAX observations of high X-ray emission.

There is a broad understanding of the processes in blazars that give rise to the high energy component that is seen. Current models ascribe this high energy emission to production by inverse Compton scattering of low energy photons by the relativistic jet. These soft photons may be either the sychrotron photons themselves (the SSC model) or photons produced in the disc or broad line region.

The peak frequency of this Compton component is then determined by the position of the lower energy sychrotron peak. A simple model has recently been introduced to account for the phenomenology of gamma-ray bright blazars (Fossati et al. (1998); Ghisellini et al. (1998)). This model predicts that: there is a fixed ratio between the frequencies of the Compton and synchrotron energy peaks of 5×10^8, and the high energy peak luminosity and the radio luminosity (at 5 GHz) have a fixed ratio of 3×10^3. Stecker et al. (1996) have made predictions for the flux from AGN, using a simple model for the VHE emission and taking into account absorption on the IR background. They use simple arguments to relate the VHE fluxes to the X-ray flux, assuming that the emission is similar to that observed for Mrk 421.

7.2 Upper limits for other southern AGNs

Using the observations of southern hemisphere AGN made with the Durham Mk6 IACT between 1996 and 1998, and the information contained in chapter 6 of this thesis regarding the Mk6's efficiency of VHE gamma-ray retention, 3σ flux limits for seven AGN have been obtained. This analysis has been reserved to data contained in image size bins 4 and 5, the typical energy threshold for these observations is ~ 2TeV, similar to the typical threshold of the CANGAROO telescope, which has also been used to observe southern hemisphere AGNs (Roberts et al. (1999)). In addition, only those segments which were observed at less than 45° zenith angle have been used, for this reason the number of on-source segments given in Chadwick et al (1999d) (2000a) and (2000b) are different from those given here in table 7.1. This table provides the numbers of on-source segments for the seven southern hemisphere AGN observed with the Mk6 IACT and the year and month in which these observations were made. The flux limits for these AGNs will be discussed individually in the following subsections.

Object	Date	Number of on-source scans
Cen A	1997 Mar	22
PKS 1514-24	1996 Apr	53
1ES 2316-423	1997 Aug/Sep	37
1ES 1101-232	1998 May	43
RX J1058-275	1996 Mar	11
PKS 0548-322	1996 Mar	95
PKS 2005-489	1996 to 1999 inc [Jun to Aug]	358

Table 7.1: a summary of the observing log for observations of AGNs made with the Mk6 telescope.

7.2.1 Cen A

Cen A (NGC 5128) is the closest radio-loud active galaxy to Earth, at a distance of 5 Mpc (z=0.008), and is often described as the prototype Fanaroff-Riley type 1 low-luminosity radio galaxy. It was tentatively identified as a TeV source in the early days of VHE gamma-ray astronomy (Grindlay et al. (1975)), with a flux of $(4.4\pm1.0)\times10^{-7}$ m^{-2} s^{-1} at an energy threshold of 300GeV. Observations of Cen A were also made with the University of Durham Mk3 IACT, which placed a 3σ flux limit of 7.8×10^{-7} m^{-2} s^{-1} at a similar energy threshold (Carraminana et al. (1990)). The X-ray state of Cen A at the time of these observations was unknown. The observations of Cen A made with the Mk6 IACT reported here provide a flux limit of 3.8×10^{-7} m^{-2} s^{-1} above 1.5 TeV. BeppoSAX observations made in 1997 February, approximately 2 weeks before the commencement of our observations, show the source to have been in a low state; lower by a factor of ~5 than the outburst in 1974-1975 (Grandi et al. (2000)). RXTE observations taken contemporaneously with our data confirm that Cen A was in a low state in 1997 March. If, as seems to be the case in other AGNs, the X-ray and VHE gamma-ray emission from Cen A are correlated, then it may not be surprising that no VHE emission was detected in 1997 March.

7.2.2 PKS 1514-24

Misidentified initially as AP Libra, PKS 1514-24 was one of the first radio-detected BL Lac objects (Bolton, Clarke and Ekers (1965)). It has a redshift of 0.049, and although detected by EXOSAT (Schwartz and Ku (1983)), its relatively small X-ray flux classifies it as an RBL object (Ciliegi et al. (1993)). Phase 1 observations with

the EGRET detector on board CGRO resulted in an upper limit for the object of 7 x 10^{-4} m^{-2} s^{-1} at >100 GeV (Fichtel et al. (1994)), and it does not appear in the third EGRET catalog (Hartman et al. (1999)). The VHE limit presented here is 2.8 x 10^{-7} m^{-2} s^{-1} above 1.5 TeV.

7.2.3 1ES 2316-423

The Object 1ES 2316-423 (z = 0.055) was originally classified as an RBL, known as PKS 2316-423, see e.g. Stickel et al. (1991). Recently however Perlman et al. (1998) have identified this object as an intermediate case whose high-energy emission could reach VHE energies. The limit presented here is 3.7 x 10^{-7} m^{-2} s^{-1} above 1.5TeV.

7.2.4 1ES 1101-232

The object 1ES 1101-232 is an XBL object with a redshift of 0.186. It has been detected using both the HEAO 2 and Einstein satellites (Della Ceca et al. (1990); Perlman et al. (1996a)). Phase 1 EGRET observations resulted in an upper limit of 6 x 10^{-4} m^{-2} s^{-1} at E > 100 MeV (Fichtel et al. (1994)). It was detected with the BeppoSAX satellite in 1997 (Wolter et al. (1998)), and our observations of this XBL objects were made at a similar time as a BeppoSAX campaign on the object. Indications are that the X-ray flux from 1ES 1101-232 was ~30% lower during our observations than in 1997 (A. Wolter 1999, private communication). Our flux limit is 3.4 x 10^{-7} m^{-2} s^{-1} above 1.5 TeV.

7.2.5 RX J1058-275

The ROSAT source RX J1058-275 was initially identified as a potential BL Lac object from its optical characteristics (Bade, Fink, and Ekers (1994)). It has a redshift

of 0.092 and is classified as an XBL object. Our flux limit is 8.8 x 10^{-7} m^{-2} s^{-1} above 1.5 TeV.

7.2.5 PKS 0548-322

The object PKS 0548-322 is at a redshift of 0.069 (Fosbury and Disney (1976)). The high X-ray flux and wide band spectral shape indicates that it is an HBL. Observations with OSSE (McNaron-Brown et al. (1995)) and EGRET (Thompson et al. (1995); Hartman et al. (1999)) have failed to detect gamma-ray emission. Our flux limit is 2.0 x 10^{-7} m^{-2} s^{-1} above 1.5 TeV.

7.2.5 PKS 2005-489

PKS 2005-489 was identified as a very bright BL Lac by Wall et al. 1986 and was found to be at a redshift of z = 0.071 (Falomo et al. 1987). Although it was discovered in the radio band (and so would formerly have been classified as a radio-selected BL Lac) it is now classified as an HBL or an intermediate object on the basis of its X-ray-to -radio flux ratio (Sambruna et al. (1995); Perlman et al. (1996)). Unusually, it has been detected in the EUV band (Marshall et al. (1995)). Although not listed as a 100 MeV gamma-ray source in the 2nd or 3rd EGRET catalogues (Thompson et al. (1995), Hartman et al. (1999)) it is seen as a marginal source at energies above 100 MeV (Lin et al. (1996); Lin et al. (1997); Lin et al. (1999)). It also seen at marginal significance in the GeV EGRET catalogue (Lamb and Macomb (1997)). Our flux limit is 1.2 x 10^{-7} m^{-2} s^{-1} above 1.5 TeV.

7.3 Further work

The Durham very high energy gamma-ray group ceased operations at the Bohena creek observatory near Narrabri NSW Australia at the end of 1999. The results of simulations presented in this thesis are likely to be the last statement on the observations made with the Mk6 IACT regarding the AGN observable at zenith angles below 45°.

Using data obtained at zenith angles greater than 45° the Mk6 IACT detected Mrk 501 (Chadwick et al (1999f)) and obtained 3σ flux limits from observations of an additional two AGN; PKS 0829+046 and 1ES 0323+022 (Chadwick et al. (1999d) and (2000b)). The data collected regarding these northern hemisphere AGN can not be analysed using the insight into the sensitivity of the Mk6 IACT given in this thesis, as the majority of the observations were made at zenith angles greater than 45°. Additional simulations would need to be made at the appropriate zenith angle for each of these objects as seen from Narrabri. Nonetheless, the SOLMK input parameters describing the main features of the Mk6 IACT derived in this thesis could be used as a starting point for such simulations. A similar case holds for the galactic objects observed with the Mk6 IACT over its four year operational lifetime, though in this case it is not the zenith angle which is of primary concern but the much brighter background star fields that alter the noise levels prevalent within the detector PMTs. The simulations would need to be recallibrated on the observed background cosmic ray count rate and the resultant image parameters matched to those observed in their off source data sets.

7.4 The future of ground-based gamma-ray astronomy

The imaging atmospheric Cherenkov technique continues to be the favoured method for detecting gamma-rays in the 100 GeV to 10 TeV energy range (see, e.g. Fegan (1997); Lorenz (2001)). A number of large arrays of IACTs have been proposed, including the VERITAS (Bradbury et al. (1999)) planned by the Whipple group, the HESS array (Kohnle et al. (1999)) by the HEGRA and CAT groups (with aid from the Durham group), and the CANGAROO-III array (Mori et al. (2000)). In each case, the arrays are planned to exploit the high sensitivity of the imaging atmospheric Cherenkov technique and the high sensitivity and angular resolution of the array approach.

However, particle air shower arrays such as the Tibet air shower array (Amenomori et al. (1999)) and the MILAGRO water Cherenkov detector in New Mexico (Sinnis et al. (1996)) also have good sensitivity to gamma-rays. Satellite experiments such as GLAST, with a planned launch in 2005 (Kniffen, Bertsch and Gehrels (2000)) will complement the next generation of ground-based IACT arrays, with overlapping energy sensitivity ranges. Combined with the low energy thresholds that can be achieved with Solar array telescopes (see, e.g. Ong (2000); Smith and de Naurois (2000); Zweerink et al. (2000); Arqueros et al. (1999)), the range between ~30 GeV and a few 100 GeV which has in the past been inaccessible to both satellite experiments (due to their necessarily small collection areas) and ground-based experiments (due to the development of the techniques required) will finally be closed.

Dramatic instrumentation developments have in the past always led to new scientific results. From a review of the physics objectives of these up and coming instruments it appears that many are optimistic that within the next decade major and long-standing physics questions can be resolved, such as the origin of the Galactic cosmic rays, the non-thermal characteristics of AGN and quasars, and non-thermal history of galaxy formation in large galaxy clusters; the diffuse extragalactic optical/infrared photon background produced by the galaxies since their formation; as well as the absolute distance scale (the Hubble constant) to many extragalactic VHE gamma-ray sources.

7.4.1 The HESS project

HESS is expected to achieve an energy threshold of about 40 GeV for gamma-ray detection and 100 GeV for spectroscopy; significantly better than any IACT currently in operation. Located in the southern hemisphere at one of the best astronomical sites in the world (originally short listed as an observing site by the European Southern Observatory (ESO)) HESS offers unprecedented opportunities for the observation of the galactic plane - probing SNRs, investigating microquasars, identifying of the EGRET unidentified sources and extending the VHE gamma-ray catalogue of active galactic nuclei.

HESS phase 1 comprises four telescopes, each with a reflective area of $82m^2$ composed of 300 individual elements of focal length 15m. Arranged in a Davis-Cotton configuration, the composite mirror dish is expected to provide a spot size of less than 0.05^o. The detectors will consist of 960 pixels, with each pixel viewing

0.16°. The field of view will be initially 4.3°, expandable to 5° with the addition of further rings of pixels. When completed the HESS array of IACTs is expected to represent an improvement of more than an order of magnitude over any existing VHE gamma-ray telescope. If the HESS phase 1 array were to be used to observe PKS 2155-304 and if it were to be in the flaring mode which has apparently been observed here an exposure of only 2 to 3 minutes would be sufficent for a 5σ detection.

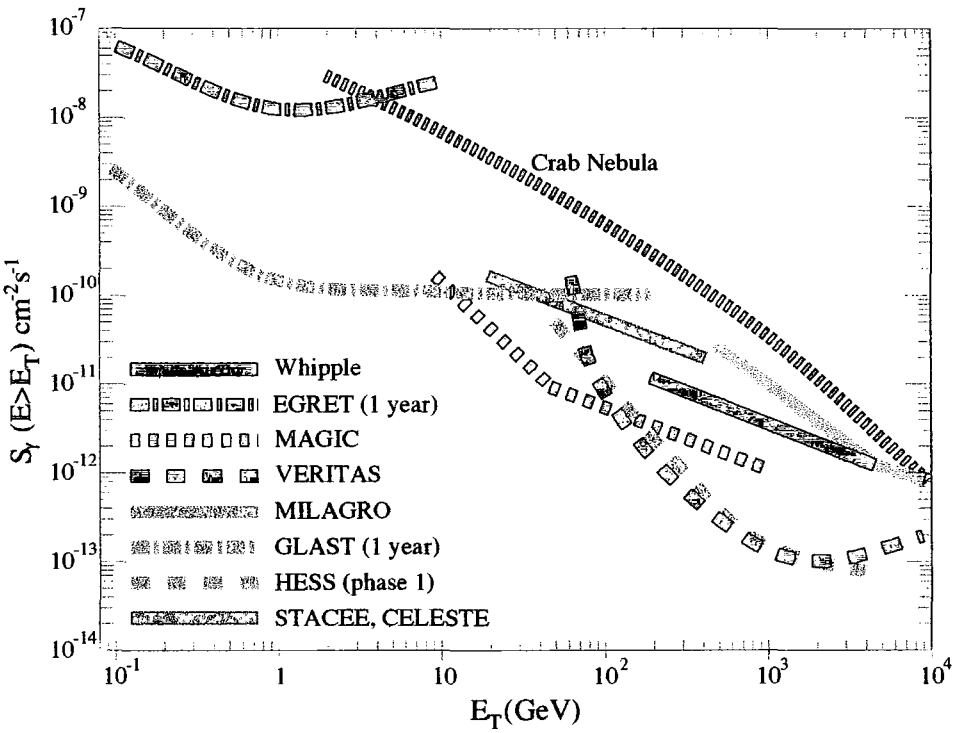

Figure 7.1: Sensitivity curves of the main proposed and existing IACT observatories. sensitivities for EGRET and GLAST satellite detectors are for one year and the atmospheric Cherenkov detectors are for 50 hours. In all cases a 5s point source detection is required with the additional requirement that the signal contain at least 10 photons.

REFERENCES

Aharonian, F, et al., 1999, A&A., 342, 69

Allan, 1971, Prog. Elem. Part. & Cosmic Ray Physics., 10, 170

Amelino-Camelia, G, et al., 1998, Nature, 393, 765

Amenomori, M, et al., 1999, Proc. 26th International cosmic ray conf, Salt Lake, 3, 486

Armstrong, P, et al., 1999, Exp.Astron., 9, 51

Arqueros, F, et al., 1999, Proc. 26th International cosmic ray conf, Salt Lake, 5, 219

Arzoumanian, Z., Nice, D, & Taylor, J. H., 1992, GRO/Radio Timing Database (Prinston: Princeton Univ)

Bade, N, Fink, H. H, & Ekers, R. D., 1965, Australian J. Phys., 18, 627

Bell, A.R., 1978. Mon.Not.R.Astron.Soc., 182, 147

Bergstrom, L, et al., 1998, Astropart.Phys., 9, 137

Bhat, C. L., 1997, Proc. Towards a Major Atmospheric Cherenkov Detector V, Berg-en-Dal, 398

Blackett, P. M. S., 1948, Phys.Soc.London, Gaissot.Comm.Rep., 34

Blumenthal, G.R. & Gould, R. J., 1970. RevMod.Phys., 42. 237

Bolton, J. G, Clarke, M.G, & Ekers, R. D., 1965, Australian J. Phys., 18, 627

Bradbury, S. M, et al., 1999, Proc. 26th International cosmic ray conf, Salt Lake, 5, 263

Brazier, K. T. S, et al., 1998, Exp.Astron., 1, 77

Brinkmann, W, et al., 1994, A&A, 288, 433

Browning, R, & Turver, K. E., 1977, Nuvo Cimento, 38A, 223

Buckly D. J. et al., 1999, Exper Astron, 9, 4, 237-249,

Cantanese, M, et al., 1997a, Ap.J., 487, L143

Cantanese, M, et al., 1997b, Proc. 25th International Cosmic Ray Conf., Durban, 3, 176

Cantanese, M. et al., 1998, Ap.J., 501, 616

Carraminana, A, et al., 1990, A&A, 228, 327

Castagnoli, C, et al., 1972, Nuvo Cimento, 9B, 213

Cawley, M. F, et al., 1993, Proc. Towards a major atmospheric detector II, Calgary, 176

Chadwick, P M, et al., 1998a, Ap. J., 503, 391

Chadwick, P. M, et al., 1998b, Astropart.Phys., 9, 131

Chadwick, P. M, et al., 1999a, Proc. 26th International cosmic ray conf, Salt Lake, 5, 227

Chadwick, P. M, et al., 1999b, Ap.J., 513, 161

Chadwick, P. M, et al., 1999c, Astropart.Phys., 11, 145

Chadwick, P. M, et al., 1999d, 5th Compton Symp. New Hampshire, A058

Chadwick, P. M, et al., 1999e, Proc. 26th International cosmic ray conf, Salt Lake, 4, 72

Chadwick, P. M, et al., 1999f, J.Phys.G: Nuc.Part.Phys., 25, 1749

Chadwick, P. M, et al., 1999g, Ap.J., 521, 547

Chadwick, P. M, et al., 2000a, A&A., 364, 450

Chadwick, P. M, et al., 2000b, Proc. Towards a Major Atmospheric Cherenkov Detector VI, Snowbird, 91

Chiappetti, L., & Torroni, V., 1997, IAU Circ. 6776

Chiappetti, L, et al., 1999, ApJ., 521, 552

Cherenkov, P. A., 1937, Phys.Rev., 52, 378

Chudakov, A. E, et al., 1965, Trans. Consultants Bureau, P.N.Lebedev Phys. Inst. 26, 99

Ciliegi, P, et al., 1993, ApJS., 85, 111

Cocconi, G., 1959, Proc. 7th Int. Cosmic Ray Conf., Moscow, 2, 309

Cooke, B. A, et al., 1978, MNRAS, 182, 489

Courvoisier, T. J. L, et al., 1995, ApJ., 438, 108

Daum, A, et al., 1997, Astropart.Phys., 8, 1

Deckers, T, et al., 1997, Proc. 25th International Cosmic Ray Conf., Durban, 3, 245

Della Ceca, R, et al., 1990, ApJS., 72, 471

Dickinson, J. E., 1999, PhD.Thesis, University of Durham, UK

Edelson, R, et al., 1992, ApJS, 83, 1

Falomo, R, et al., 1987, ApJ., 218, L39

Fegan, D. J., 1997, J.Phys.G: Nucl. Part. Phys., 23, 1013

Fermi, E., 1949. Phys.Rev., 75, 1169

Fichtel, C. E, et al., 1994, ApJS., 94, 551

Fishman, G. J, et al., 1992, in The Compton Observatory Science Workshop, NASA, Washington, 3137, 26

Fossati, G, et al., 1998, MNRAS, 299, 443

Fosbury, R. A. R, & Disney, M. J., 1976, ApJ., 207, 75

Frank, I. M, & Tamm, I. G., 1937, Dokl.Fys.Nauk., SSSR, 14, 109

Gaidos, J. A, et al., 1996, Nature., 383, 319

Gaisser, T. K., 1990, "Cosmic rays & particle physics", Cambridge University Press

Galbraith, W, & Jelley, J. V., 1953a, J.Atmosph.Terr.Phys., 6, 250

Galbraith, W, & Jelley, J. V., 1953b, Nature, 171, 349

Ghisellini, G, et al., 1998, MNRAS., 301, 451

Gibson, A. I, et al., 1982, Proc, Int. Workshop on Very High Energy Gamma Ray Astronomy, Bombay, 97

Ginzberg, V.L, 1940., Zh.Fiz., SSSR, 2, 441

Goeckel, 1910, Phys.Zeits., 11, 280

Goret, P, et al., 1997, Proc. 25th Int. Cosmic Ray Conf., Durban, 3, 185

Gould, R. J, & Schreder, G. P., 1966, Phys.Rev.Lett, 6, 252.

Gould, R. J, & Schreder, G. P., 1965, Phys.Rev.Lett, 15, 511.

Grandi, P, et al., 2000, Adv. Space Res. 25, 485

Griffiths, R. E., 1979, ApJ., 234, 810

Grindlay, J. E, et al., 1975, ApJ., 197, L9

Grindlay, J. E., 1971, Nuvo Cimento 2B, 119

Hartman, R. C, et al., 1992, in The Compton Observatory Science Workshop, Berg-en-Dal, 166

Hartman, R. C, et al., 1999, ApJS., 123, 79

Haungs. A, et al., 1997, Proc. 26th International cosmic ray conf, Salt Lake, 5, 291

Hayashida, N, et al., 1998, ApJ., 504, L71

Heaviside, O., 1890., Electrical. Papers., 2, 494

Heck, D., 1999, Workshop 'Simulation and Analysis Methods for Large Neutrino Detectors' Report: DESY-PROC-1999-01, P288

Hess, V. F., 1912, Phys.Zeits, 13, 1084

Hill, D. A, & Porter, N. A., 1961, Nature, 191, 690

Hillas, A. M., 1972, Cosmic rays. Oxford: Pergamon Press

Hillas, A. M., 1979, Proc. 16th International cosmic ray conf., Kyoto, 8, 7

Hillas, A. M., 1981, Proc. 17th International cosmic ray conf., Paris, 8, 193

Hillas, A. M., 1985, Proc. 19th International cosmic ray conf., La Jolla, 3, 445

Hillas, A. M. & Patterson, J. R., 1990, J.Phys.G: Nucl.Part.Phys., 16, 1271

Hillas, A. M., 1995, Proc. 24th International cosmic ray conf., Rome, 1, 270

Hillas, A. M., 1996, Space Science Reviews., 75, 17

Hillas, A. M., 1997, Nuc.Phys.B (Proc.Suppl.), 52B, 29

Hillas, A. M., 1998, Nature., 395, 15

Horan, D, et al., 2002, Ap.J., 571 753

Jelley, J.V., 1958, "Cherenkov Radiation and its Applications", London, Pergamon Press

Jelley, J. V, & Galbraith, W., 1955, J. Atmos. Phys., 6, 304

Jelley, J. S, & Porter, N. A., 1963, Q. J. R. Astron. Soc., 4, 275

Jursa, A. S., sci. ed., 1985, Handbook of Geophysics and the Space Environment, Air Force Geophysics Laboratory, NTIS Document ADA 167000

Kifune, T, et al., 1995, Ap. J., 438, L91

Kniffen, D. A., Bertsch, D L., & Gehrels, N., 2000, Proc. Towards a Major Atmospheric Cherenkov Detector VI, Snowbird (1999), 492

Kohnle, A, et al., 1999, Proc. 26th International cosmic ray conf., Salt Lake, 5, 239

Kolhorster, W., 1913, Phys.Zeits., 14, 1066

Konopelko, A, & Plyasheshnikov, A., 2000, Nucl.Instrum.Meth., A450, 419

Krennrich, F, et al., 1997, Ap.J., 481, 758

Krennrich, F, et al., 1999, Ap.J., 511, 149

Lamb, R. C, & Macomb, D. J., 1997, ApJ., 488, 872

Le Bohec, S, et al., 1998, NIM., A416, 425

Lessard, R. W, et al., 2000, Ap.J., 531, 942

Lin, Y. C, et al., 1992, ApJ., 401, L61

Lin, Y. C, et al., 1996, ApJS., 105, 331

Lin, Y. C, et al., 1997, ApJ., 476, L11

Lin, Y. C, et al., 1999, ApJ., 525, 191

Longair, M. S. 1997. High Energy Astrophysics Volume 1: "Particles, photons and their detection". Cambridge University Press, Cambridge

Longair, M. S. 1997. High Energy Astrophysics Volume 2: "Stars, the galaxy and the interstellar medium" Cambridge University Press, Cambridge

Lorenz, E., 2001. J.Phys.G: Nucl.Part.Phys., 27, 1675

Mallet, L. 1926., C.R.Acad.Sci. Paris., 183, 274

Mallet, L. 1928., C.R.Acad.Sci. Paris., 187, 222

Mallet, L. 1929., C.R.Acad.Sci. Paris., 188, 445

Maraschi, L, et al., 1998, Proc. of the III National Meeting on AGNs, J.It.Astr.Soc 193

Marshall, H. L, et al., 1995, ApJ., 439, 90

McEnery, J. E., 1997, PhD.Thesis, University College Dublin, Ireland

McNaron-Brown, K, et al., 1995, ApJ., 451, 575

Mohanty, G, et al., 1998, Astropart.Phys., 9. 15

Mori, M, et al., 2000, Proc. Towards a Major Atmospheric Cherenkov Detector VI, Snowbird, 485

Moriarty, P. & Samuelson, F. W., 2000, Proc. Towards a Major Atmospheric Cherenkov Detector VI, Snowbird, 338

Muraishi, H., et al, 2000, A&A., 354, L57-L61

Nesphor, Y. I., et al, 1998, Ap.J. Lett., 24. 139

Nesphor, Y. I., et al, 2001, Astron.Rep., 45, 249

Nikishov, I. D., 1962, Soviet.Physics, JETP, 14. 393

Nishiyama, T, et al., 1999, Proc. 26th International Cosmic Ray Conf, Salt Lake, 3, 370

Ong, R. A. & Covault, C. E., 1997, Proc. Towards a Major Atmospheric Cherenkov Detector V, Berg-en-Dal, 247

Ong, R. A., 1998, Phys.Rep., 305, 93

Ong, R. A., 2000, Towards a Major Atmospheric Cherenkov Detector VI, Snowbird, 401

Perlman, E. S., et al. 1996, ApJS, 104, 251

Perlman, E. S., et al. 1996a, ApJS, 456, 451

Perlman, E. S., et al. 1998, AJ., 115, 1253

Pesce, J. E. et al., 1997, ApJ., 486, 770

Pian, E. et al., 1997, ApJ., 486, 784

Plyasheshnikov, A. V., & Bignami, G.F., 1985, Nuovo Cimento, 32B, 514

Porter, N. A., & Weekes, T. C., 1979, Smithsonian Astrophysical Observatory Special Report 381

Puelhofer, G. et al., 2000 Proc. 26th Int. Cosmic Ray Conf. OG 2.2.17

Punch, M. et al., 1992, Nature, 358, 477

Punch, M., et al, 1991, Proc. 22nd Int. Cosmic Ray Conf., Dublin 1, 464

Quebert, J., 1997 Proc. Towards a Major Atmospheric Cherenkov Detector V, Berg-en-Dal, 234

Quinn, J. et al., 1996, Ap.J., 456, L83

Quinn, J. et al., 1997, Proc. 25th International Cosmic Ray Conf, 3, 249

Ramana-Murthy, P. V. & Wolfendale, A. W., 1986, "Gamma ray astronomy", Cambridge University Press, Cambridge

Rao, M. V. S. & Sinha, S., 1988, J.Phys.G: Nucl.Part.Phys., 14, 811

Reynolds, P. T., et al, 1993, Ap.J., 404, 206

Rieke, G. H., 1969, S.A.O. Special.Report No: 301

Roberts (1998), PhD.Thesis, University of Durham, UK

Roberts, M. D., et al. 1999, A&A, 343, 691

Rossi, B., & Greisen, K., 1941, Rev.Mod.Phys., 13, 240

Rutherford & Cook, 1903, Phys.Rev., 16, 183

Rybicki, G. B. & Lightman, A. P. 1979. "Radiative processes in astrophysics". New York: Interscience Publishers

Sambruna, R, M., et al, 1995, ApJ., 449, 567

Samuelson, F., et al, 1998, ApJ., 501, L17

Schwartz, D. A. et al., 1979, ApJ., 229, L53

Schwartz, D. A., & Ku, W. H. 1983, ApJ., 266, 459

Shaw, S. E., 1999, PhD.Thesis, University of Durham, UK

Sinitsyna, V. G. 1997, Proc. Towards a Major Atmospheric Cherenkov Detector V, Berg-en-Dal, 190

Sinnis, C., et al. 1996, Amer.Astron.Soc.Meeting, Vol. 188, 8509

Smith, D. A. & de Naurois, M. 2000, Towards a Major Atmospheric Cherenkov Detector VI, Snowbird, 416

Sreekumar, P., & Vestrand, T., 1997, IAU Circ. 6774

Stecker, F. W. et al., 1996, ApJ., 473, L75

Stecker, F. W., & de Jager, O. C., 1997, Ap.J., 476, 712

Stecker, F. W., & de Jager, O. C., 1998, A&A., 334, L85

Stecker, F. W., de Jager, O. C., & Salamon, M. H., 1992, ApJ., 390, L49

Stecker, F. W., de Jager, O. C., & Salamon, M. H., 1996, ApJ., 473, L75

Stepanian, A. A. et al., 1983, Izvestia, CAO J. 66, 234

Stickel, M., et al, 1991, ApJ, 374, 431

Tanimori, T. et al., 1998, Ap.J., 497, L25

Takahashi, T. et al., 1998, IAU Circ. 6888

Tavecchio, F, et al., 1998, Ap.J, 509, 608

Thompson, D. J. et al., 1995, ApJS., 101, 259

Turver, K. E., & Weekes, T. C., 1978, Nuovo Cimento, 45B, 99

Urry, C. M., 1993, ApJ., 411, 614

Vassiliev, V. V, et al., 1997, Proc. 25th International cosmic ray conf, Durban, 6, 249

Vestrand, W. T, et al., 1995, ApJ., 454, L93

Vestrand, W. T, et al., 1999, 5th Compton Symp. New Hampshire, A224

Wandel, A., & Urry, C. M. 1991, ApJ., 367, 78

Weekes, T. C. & Turver, K. E, 1977, Proceedings of the 12th Eslab Symp. Frascati, ESA SP-124, 279

Weekes, T. C., 1992, Sp.Sci.Rev., 59, 314

Weekes, T. C, et al., 1989, Ap. J., 342, 379

Weekes, T. C, et al., 1997, Proc. Towards a major Cherenkov detector V, Berg-en-Dal, 202

Weekes, T. C., private communication

Wiebel, B., 1994, WUB 94-08, Chemical composition in high energy cosmic rays, Bergische Universität-Gesamthochschule Wuppertal

Wolter, A, et al., 1998, A&A., 335, 899

Yen, E., 1974, Phys.Rev.D, 10, 836

Yoshikoshi, T. et al., 1997, Ap. J., 487, L65

Zatsepin, V. I., & Chudakov, A. E., 1962a, Sov.Phys, JETP, 15, 1126

Zatsepin, V. I., & Chudakov, A. E., 1962b, Sov.Phys, JETP, 24, 1622

Zweerink, J. A, et al., 1997, Ap.J, 490, L141

Zweerink, J. A, et al., 2000, Towards a Major Atmospheric Cherenkov Detector VI, Snowbird, 426

Zyskin, Y. L, et al., 1987, Proc.20th IntCosmic Ray Conf, Moscow, 2, 342